Spring 5-23-2019

Modeling the Effect of a Compartment Fire on Spaces Adjacent to a Bulkhead With and Without Attachments

Carl E. Hendrickson II
University of New Orleans, cehendri@uno.edu

Modeling the Effect of a Compartment Fire on Spaces Adjacent to a Bulkhead, With and Without Attachments

A Thesis

Submitted to the Graduate Faculty of the
University of New Orleans
in partial fulfillment of the
requirements for the degree of

Master of Science
in
Engineering
Mechanical

by

Carl Hendrickson

B.S. United States Merchant Marine Academy, 2014

May, 2019

Acknowledgement

I would like to convey my gratitude and respect for my thesis advisor, Dr. Martin Guillot. He pushed me to properly research and produce a detailed and comprehensive report. I am thankful for his constant guidance and feedback throughout this entire process.

I would also like to thank my wife, Maria, who always offered her unconditional support throughout this program. She helped me to schedule my time efficiently and was always a source of motivation.

Additionally, I would like to thank my parents for their endless support and love. They taught me the importance of dedication and ambition, both of which were instrumental in putting together this thesis.

Lastly, I would like to thank the University of New Orleans Master of Science in Engineering program. The thorough graduate education I have received has made it possible to construct a research thesis that will provide insight into the regulations regarding fire safety aboard ships.

Table of Contents

List of Figures

List of Tables

Nomenclature

(x, y, z) Cartesian Coordinates

(u, v, w) Velocity Components

H Height (m)

L Length (m)

g Gravitational Acceleration (m/s^2)

T Temperature (K)

p Pressure (Pa)

h Convection Coefficient (W/m^2K)

V Volume (m^3)

c_p Specific Heat (J/kgK)

m mass (kg)

T_{i1} Surface temperature of fire side surface of insulation (function of time) (K)

T_s, T_i, T_a Temperature of steel, insulation, and air (function of time) (K)

κ Thermal Conductivity (W/mK)

$\bar{\kappa}$ Average Thermal Conductivity (W/mK)

t time (s)

M_w Molecular Weight of Gas

q'' Heat Flux, Heat Transfer per Unit Area (W/m^2)

Pr Prandtl number

Gr Grashof number

Bi Local Convective Heat Transfer Parameter

Ra Rayleigh number

Nu Nusselt number

Re Reynolds number

Lumped Capacitance

q_0 Heat Transfer from Fire to Insulation (W)

q_1 Heat Transfer Insulation to Steel (W)

q_2 Heat Transfer Steel to Air (W)

Lumped Capacitance Parallel Flow

q_0 Heat Transfer from Fire to Attachment (W)

q_1 Heat Transfer from Attachment to Air (W)

q_2 Heat Transfer from Fire to Insulation (W)

q_3 Heat Transfer from Insulation to Steel (W)

q_4 Heat Transfer from Steel to Air (W)

$s1$ Attachment

$s2$ Steel

L_T Length of Attachment

Greek Symbols

μ Viscosity (kg/ms)

ν Kinematic Viscosity (m^2/s)

α Thermal Diffusivity (m^2/s)

β Thermal Expansion Coefficient $(1/K)$

ρ Density (kg/m^3)

Subscript

i insulation

s steel

a air

f fire

j Index

Abstract

Structural fire protection is an integral component of shipboard fire safety. There are national and international regulations that delineate requirements for the insulation placed throughout ships. The attachments that penetrate the insulation for hanging wires and pipes can disrupt the integrity of the division, and cause a failure to adhere to the regulations. This problem will be analyzed by using a simplified lumped capacitance model and ANSYS FLUENT CFD. A standard time-temperature fire curve is applied to the fire side of the enclosure. The thermal conductivity of the insulation and steel are made to be temperature dependent. The density of the air of the non-fire side is then approximated using the Boussinesq approximation for lower temperature differences and the incompressible ideal gas law for higher temperature differences. Different attachments of varying surface areas and volumes are exposed to the standard time-temperature fire curve and their heat transfer capabilities are analyzed.

Keywords: fire safety, insulation, fire curve, ship safety, CFD, lumped capacitance, Boussinesq approximation, incompressible ideal gas

I. Introduction

Safety is vital in the proper functioning of vessels and adequate protection of both people and materials aboard ships. Among the various threats to shipboard safety, fires are some of the most devastating disasters that can lead to loss of both life and property. As a result, this has led to the implementation of broad regulations for ships to maintain a minimum standard of safety in regard to fire protection.

The regulations regarding fire control boundaries can be found in SOLAS (Safety of Life at Sea) Chapter II-2 and CFR (Code of Federal Regulations) 46. CFR considers the provisions provided by SOLAS to be equivalent to their own federal regulations. SOLAS states the requirements for the constraints of bulkheads and decks, but also references the FTP (Fire Testing Procedure) Code for methods regarding testing the materials.

The purpose of SOLAS in regard to its requirement for fire safety is to "prevent the occurrence of fire and explosion; reduce the risk to life caused by fire; reduce the risk of damage caused by fire to the ship, its cargo and the environment; contain, control and suppress fire and explosion in the compartment of origin, and provide adequate and readily accessible means of escape for passengers and crew" (SOLAS Consolidated Edition, 2014).

In order to properly implement these regulations, each vessel needs to have emergency arrangements in place in order to combat fires. Additionally, the crew must be trained in firefighting and have ample, competent fireteams to effectively combat a potential fire. Lastly, there needs to be installed passive fire protection and fire suppression systems (SOLAS Consolidated Edition, 2014).

The passive fire protection is accomplished onboard a ship through insulation. The bulkheads and decks of ships are made to be resistant to fire. However, the multiple penetrations for hanging wires, cables, and pipes may not be as impervious as the bulkheads. When these penetrations are not insulated

properly, there can be a disruption in their integrity and a failure of the ship's fire suppression capabilities, potentially inducing a catastrophic loss of property and life (Beene et al., 1988).

This thesis studies attachments. Attachments and penetrations are very similar. A penetration goes not only through the insulation, but also through the steel bulkhead or deck. An attachment will only go through the insulation and then be attached to the steel itself. Attachments raise the same concerns for the temperature requirements on the non-fire side, but are less likely to cause the passage of smoke and flame to the non-fire side because they do not cut into the bulkhead. Although SOLAS does not speak specifically to attachments, it is assumed that the regulations for penetrations are equivalent.

The United States Coast Guard (USCG) has reported that some shipbuilders have raised concerns regarding the necessity of insulating attachments (C. Briggs, personal communication, April 30, 2018). Shipbuilders claim that attachments are too insignificant to cause a failure of the regulations and therefore do not pose a danger to ships when there is a fire onboard. These shipbuilders state that insulating the attachments is an unnecessary costly expenditure in terms of money, resources, and time. They maintain that the fire divisions can meet the criteria stated by the regulations without insulating these attachments. However, the regulations claim that attachments are significant and crucial to the fire protection system (SOLAS Consolidated Edition, 2014). This study explores the implications of attachments without insulation and examines if the attachments meet the expectations held within the established regulations.

II. Background

Ship fire regulations are complex and encompass many different components. Each physical division aboard a ship, including bulkheads and decks, is split into different classes that have separate requirements in regard to shipboard fire safety.

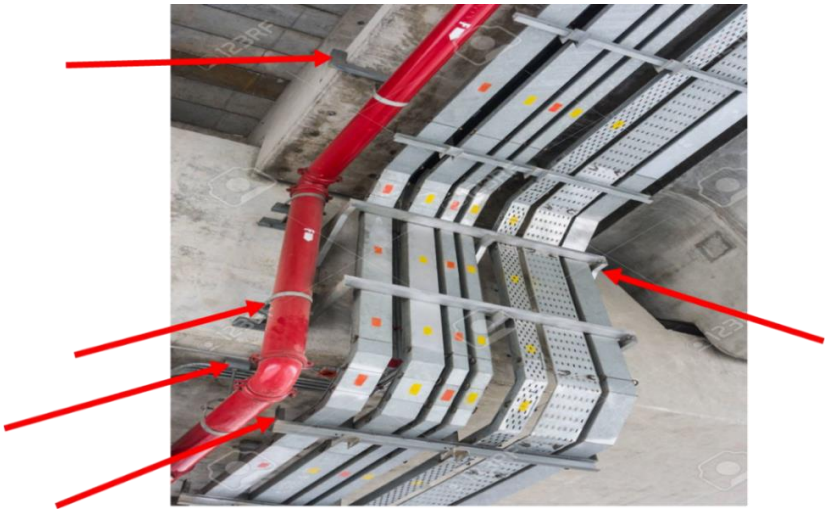

Figure II-1 Wire Hangers on Bulkhead

Figure II-1 illustrates how various attachments could harm the integrity of the fire resistance in any given bulkhead. The USCG specifically requires coat-back, a spray-on insulation, to be applied to the attachments if they cannot meet the criteria for their boundary alone.

Each bulkhead and deck on a ship is then classified as A-60, A-30, A-15, A-0, B-15, B-0, C, or C'. Depending on the location, a bulkhead will need to provide different criteria for its resistance to a fire. The "A" class division has the most stringent of criteria. "'A' class divisions are those divisions formed by bulkheads and decks which comply with the following criteria: they are constructed of steel or other equivalent material; they are suitably stiffened; they are insulated with approved non-combustible materials such that the average temperature of the unexposed side will not rise more than 140^{o} C above the original temperature, nor will the temperature, at any one point, including any joint, rise more than 180^{o} C above the original temperature" (SOLAS Consolidated Edition, 2014, p. 125). The A-60 division

has to maintain these standards for a total of 60 minutes. The "A" class division is then decreased in the time constraints for A-30, A-15, and A-0. This means that these divisions must meet the criteria for A-60 as previously stated, but for 30 minutes, 15 minutes, and 0 minutes, respectively (SOLAS Consolidated Edition, 2014).

SOLAS then goes on to describe how penetrations through fire boundaries should be treated. "Where a[n] "A" class division is penetrated, the penetration shall be tested in accordance with the FTP Code" (SOLAS Consolidated Edition, 2014). The United States accepts the testing procedures laid out in ASTM E-119 as an equivalent to the FTP Code (NVIC 9-97, 2010).

The next lower standard for the fire resistance of a bulkhead and deck is the "B" class division. Within this class, materials must be non-combustible like in the "A" class, however the difference between the two is with the temperature threshold. "B" class materials "have an insulation value such that the average temperature of the unexposed side will not rise more than 140^{o} C above the original temperature, nor will the temperature at any one point, including any joint, rise more than 225^{o} C above the original temperature" (SOLAS Consolidated Edition, 2014, p. 126). B-15 boundaries must conform to these regulations for 15 minutes, and B-0 for 0 minutes. In terms of penetrations, "arrangements shall be made to ensure that the fire resistance [within the 'B' division] is not impaired" (SOLAS Consolidated Edition, 2014, p.168).

The United States Coast Guard provides directives in order to explain the complicated regulations for the shipping industry. In regard to shipboard fire protection, the Coast Guard's provided directive is NVIC 9-97. NVIC 9-97 explains the procedure for testing structural fire protection. The regulation is as follows:

> "The required type approval tests for A-60 structural insulations are described in 46 CFR 164.007. All materials submitted for approval in this category must first pass the required test for noncombustible materials under 46 CFR 164.009. 46 CFR 164.007 is a small-scale furnace test that evaluates the fire endurance of a 1000 mm x 1500 mm (40 in

by 60 in) specimen subjected to a one-hour fire exposure. In the test, the insulation is applied to a 5 mm (3/16 inch) steel plate that is mounted in the test furnace with the insulation exposed to the fire. The furnace is then controlled at the ASTM E-119 standard time temperature curve for a one-hour period. The acceptance criteria require that the insulation must prevent the passage of flame and the emission of appreciable volumes of smoke and toxic gases from the unexposed surface during the 60 minute test period, and must also prevent the temperature on the unexposed side of the bulkhead from exceeding an average temperature rise of 139° C (250° F) above ambient, and a maximum temperature rise of 180° C (325° F) above ambient at any one thermocouple." (NVIC 9-97, 2010, p. 20)

Most of the modeling included in this thesis will be based off of the measurements mentioned in the above regulation.

United States regulations for the ASTM Standard E-119 test methods are equivalent to the IMO International Maritime Organization (IMO) Fire Testing Procedures (FTP). For the E-119 method, the test fire specimen panel, which includes physical divisions like bulkheads and decks, is set on one face of a test furnace. The furnace is then fired, and the rate of temperature produced is controlled by a standard-time temperature curve (NVIC 9-97, 2010).

$$T_f(t) = 345\log_{10}(8t+1) + 20 \tag{0.1}$$

The E-119 test then measures the fire resistance of the specimen until failure. Failure occurs when there is passage of smoke or flame or there is excessive heat transmission through the specimen.

There are also standards specifically testing the fire resistance of penetrations. These standards are ASTM E-814 and UL 1479; both of these tests incorporate the standard time-temperature curve from E-119 and have the same constraints for smoke, flame, and heat transmission (Beene et al., 1988).

In order to provide a model to research this topic, a plethora of heat transfer aspects need to be combined. These topics include time-dependent fire curves, temperature-dependent thermal material properties at elevated temperatures, and buoyancy-driven convective flow. For the proposed model, the fire curve is driving a temperature on the surface of the insulation, and provides a boundary condition for the models. The temperature of the insulation, penetration, and steel will then increase, and, as the temperature is elevated, their thermal conductivity changes. This in turn heats the air for the adjacent space to the fire. The buoyancy-driven convection displaces the heat throughout the room, and a viscous and thermal boundary layer is formed at the steel. This study combines these factors to provide a model and determine whether or not a non-insulated penetration causes a failure of the regulations.

The purpose of this study is to determine if insulating attachments that penetrate fire divisions is necessary. In order to prove the necessity of the insulation, a model is created where a non-insulated attachment is present. This model is then evaluated to determine if it conforms to the regulations. This study evaluates varying surface areas exposed to the standard time temperature curve for a total of 15 minutes. If insulating them is significant to the fire division's integrity, then this study will reinforce the regulations. If not, then further studies and experimentation will need to be conducted to determine the validity of the regulation.

III. Literature Review

Shipboard fires can be highly devastating and can easily end in the loss of property and life. A ship's passive fire protection and active fire protection are both highly complex systems that are subject to national and international regulations. In order to make a model compatible for a shipboard fire, the first item that needs to be simulated is the behavior of the fire. According to the United States Coast Guard's NVIC 9-97, when PFP is tested, the temperature of the fire should be controlled by ASTM's E-119. E-119 proposes a standard fire curve of the form:

$$T_f(t)=345\log_{10}(8t+1)+20 \tag{1.1}$$

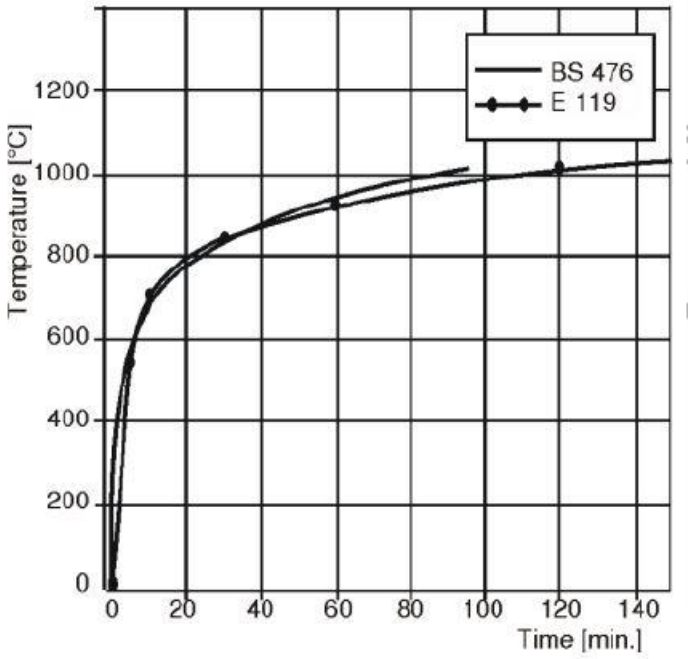

Figure III-1 E 119 Standard Fire Curve. Note. Reprinted from "A New Curve for Temperature-Time Relationship in Compartment Fire", by Blagojevic, M., 2011, Thermal Science, 15, p. 342.

Figure III-1 shows the standard fire curve where the temperature, T is the average furnace temperature in degrees Celsius and t is time in minutes. According to NVIC 9-97 and the Fire Test Procedures (FTP) Code of the International Maritime Organization (IMO), a fire endurance test of

structural insulations, bulkhead panels, doors, windows, fire dampers, and penetration seals determines if they qualify as “A” class or “B” class divisions. A specimen of the material is mounted in a full-scale laboratory furnace with gas burners that are controlled to expose the test specimen to flames and heat that follow a standard time-temperature curve (NVIC 9-97, 2010).

Studies have been conducted to challenge the accuracy of this fire curve. Blagojevic and Pesic (2011) claim that the standard fire curve does not include all the phases of a fire. According to their research, “a proper fire curve includes three distinct phases: a growth phase, which is the development phase from ignition to flashover, a steady-burning (fully developed) phase, and a decay phase” (Blagojevic and Pesic, 2011). The growth phase is not perfectly modeled within the standard fire curve. In addition, the decay phase is not represented adequately (Blagojevic and Pesic, 2011).

The SFPE Handbook of Fire Protection (2008) depicts an idealized fire curve that encompasses these three phases. The Handbook also explains the phenomena that occurs during the different phases. The first phase of the fire is the growth period. During this phase, heat begins to accumulate in the enclosure. This accumulation can cause other materials in the room to ignite as well. This phenomenon is situational and wholly depends on the materials immediately available; in terms of ships, these materials generally include steel, paint, and fuel oil, and can influence the temperature and growth of the fire. During the growth phase, there is dramatic rise in the gas temperatures which will result in a flashover. Flashover can be defined as, “A transition in the development of a compartment fire when surfaces exposed to thermal radiation from fire gases in excess of 1100°F reach ignition temperature more or less simultaneously. This causes the fire to spread rapidly throughout the space, resulting in fire involvement of the entire compartment or enclosed space” (Firefighting Procedures, 2010). Once flashover occurs, then the steady-burning or fully developed phase begins. With this idealized curve in mind, the temperature during the growth phase is relatively low and it can be assumed that the influence on the fire resistance is negligible. Therefore, the actual risk begins during the steady-burning phase. During the steady-burning phase, temperatures in excess of 1000^{o} C can be attained. This excessive and dramatic increase in temperature will have a major impact on the fire resistance of the structural members and

attachments. It is important to note that this risk of the excessive increase in temperature can still occur during the decay phase (SFPE Handbook of Fire Protection, 2008, p. 4-201).

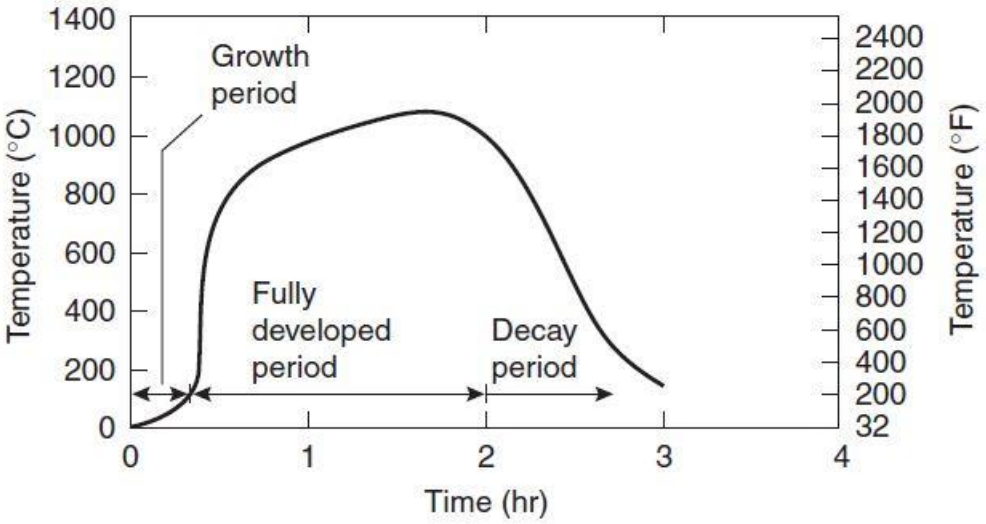

Figure III-2 Idealized Fire Curve. Note. Reprinted from SFPE Handbook of Fire Protection Engineering (4-201), by T. T. Lie, 2002, Bethesda, Maryland: National Fire Protection Association.

Figure III-2 shows the idealized fire curve and has proper representation of the three periods of a fire. The standard fire curve is more robust and experiences on-average higher temperatures than a curve representing the three phases of a fire. The standard fire curve is also still stated as the acceptable fire curve in the Coast Guard's NVIC 9-97 and the International Maritime Organization's (IMO) FTP Code.

The next important aspect of modeling a shipboard fire is to evaluate the thermal properties of insulation and steel. There are various materials used for insulation, but a commonly used one for ships is mineral wool. Budaiwi and Abdou (2005) concluded that the thermal conductivity of mineral wool increases with an increase in temperature. The thermal conductivity is also proportional to the density of the mineral wool. To determine this, Jansson (2004) used two different types of sensors: Kapton and Mica. In this study, there was a discrepancy between the measurements taken between the two sensors; the Mica sensor measured different values for the thermal conductivity than the Kapton sensor. The Mica

sensor took measurements at higher temperatures for the thermal properties. Therefore, these measurements were used for this thesis. This study uses the TPS (Transient Plane Source) method, which incorporates the Mica sensor, in order to determine the thermal properties of mineral wool. The thermal conductivity, diffusivity, and the volumetric specific heat were found at room temperature and at elevated temperatures (Jansson, 2004).

The TPS method is performed by placing a flat round hot disc sensor between two pieces of a material, as shown in Figure III-3.

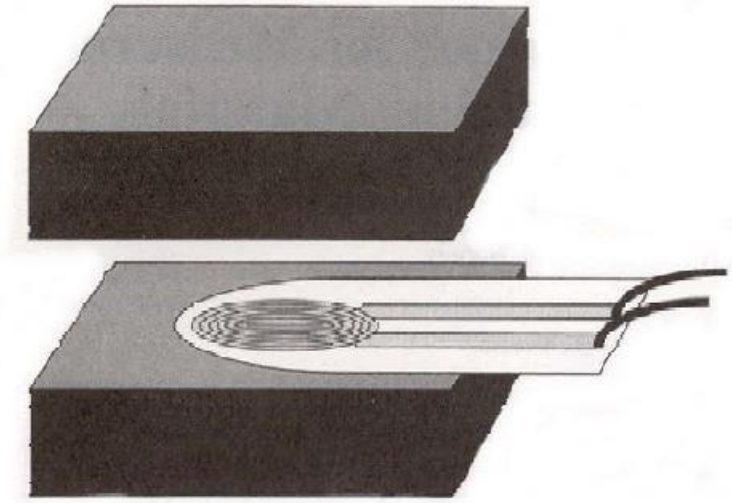

Figure III-3 Set up for TPS Method. Note. Reprinted from "Measurement of thermal properties at elevated temperatures", by Jansson, R., 2004, Swedish National Testing and Research Institute, p. 15.

The sensor is constructed of a thin nickel foil spiral, which is 10 μm thick and is placed in between two sheets of electrical insulation material. The hot disc sensor then acts as a constant effect generator and a resistance thermometer simultaneously. The beginning of the measurement starts with a stepwise power pulse being applied to the sensor. Then, when a constant electrical effect is applied, the temperature rises in the sensor and heat flows to the tested material. The time-dependent resistance rise is recorded and converted with a temperature coefficient of resistivity for nickel to a temperature response curve (Jansson, 2004).

The temperature rise in the sensor is related to the thermal properties of the tested material. In the case of the material having good insulation properties, low conductivity and diffusivity, the temperature of the sensor will rapidly rise with heat being applied. When the material has good conducting properties, the heat will be transported faster inside the material, resulting in a lower rise in temperature for the sensor. Jansson's research aptly shows how temperature affects the thermal conductivity of mineral wool. The findings from his work are important for modeling insulation at elevated temperatures (Jansson, 2004).

After the temperature of the fire affects the thermal properties of the insulation, the fire curve temperature will then affect the steel of the bulkhead. The thermal properties of the steel need to be examined. Figure III-4 shows the thermal conductivity of steel and the effect of increasing temperature. Franssen and Real (2012) evaluate the thermal properties of carbon steel and propose algebraic relations for the time-temperature dependence.

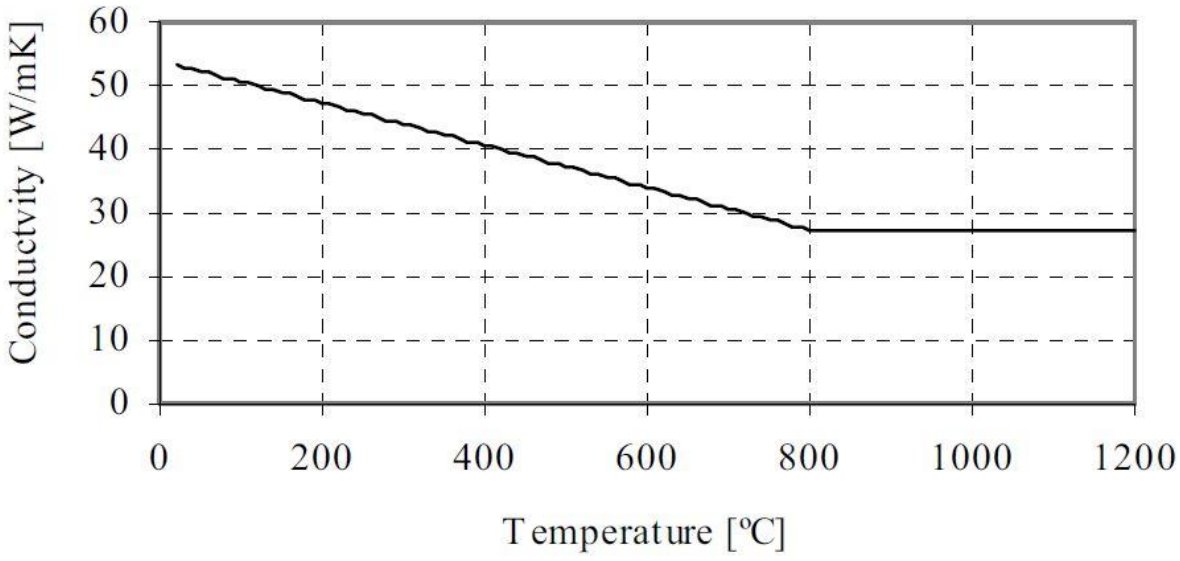

Figure III-4 Thermal Conductivity of Steel and Temperature. Reprinted from Fire Design of Steel Structures (321), by J. Franssen and P.V. Real, 2012, European Convention for Constructional Steelwork.

When $T_s < 1073.5\,K$ then;

$$\kappa = 54 - 0.033(T_s - 273.15) \tag{1.2}$$

When $T_i > 873.15\,K$ then;

$$\kappa = 0.0009T_i - 0.425835 \tag{1.3}$$

The topics of natural convection in 3-D enclosures and the thermal and viscous boundary layers produced on vertical walls have been studied extensively by many researchers: Makinde and Olanrewaju (2010), Baskak et al. (2006), and Zitzmann et al. (2005). Natural convection is caused by buoyancy forces in an enclosure. Buoyancy occurs when heat is added to a fluid causing a change in fluid density. A flow will then be induced by gravity acting upon the density variations. These buoyancy-driven flows are called natural-convection or mixed-convection. Convection Heat Transfer by Arpaci and Larsen (1984) provides a concise explanation of buoyancy driven flows. They state that the most frequently encountered buoyancy is due to gravity and is seen in the heating and cooling of spaces. "The other type of buoyancy driven flow is due to centrifugal forces, which is commonly observed in the cooling of turbine blades and inertial forces, which has an impact on the cryogenic liquids in accelerating rockets" (Convection Heat Transfer, 1984).

Many researchers have studied thermal boundary layers and convection occurring on flat vertical plates and in square enclosures. According to Makinde and Olanrewaju (2010), when there is an increase in the Prandtl number and the Grashof numbers, there is a decrease in the thermal boundary layer thickness. Below are the equations for the Prandtl and Grashof numbers.

$$\mathrm{Pr} = \frac{\nu}{\alpha} \tag{1.4}$$

$$\nu = \frac{\mu}{\rho} \tag{1.5}$$

$$Gr = \frac{\nu x g \beta \left(T_f - T_\infty\right)}{U_\infty^2} \tag{1.6}$$

An increase in temperature at the wall will therefore cause the density of air to decrease. This decrease in density causes thermal boundary layer thickness to decrease as well.

Natural convection in a square cavity has also been investigated thoroughly. Baskak et al. (2006) demonstrates the formation of thermal boundary layers with both uniform and non-uniform heating at the wall. They found that the thermal boundary layer formed from non-uniform heating is less than that developed from uniform heating. Zitzmann et al. (2005) concluded in their study of natural convection that, at the walls of an enclosure, a significant inflation factor or bias is required, like in Figure III-5, in order to obtain convergence.

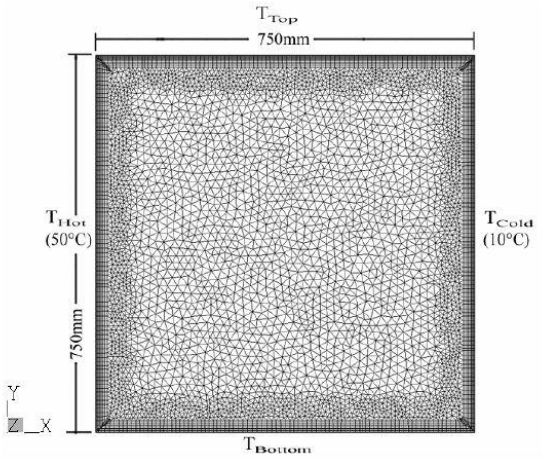

Figure III-5 80 x 80 Inflation on Walls of Square Cavity. Note. Reprinted from "Simulation of Steady-State Natural Convection Using CFD", by Zitzmann, T. et al., 2005, Building Simulation, p. 1451.

Fusegi et al. (1991) proposed natural convection in a 3-D enclosure. In this study, the boundary conditions at the walls were varied. The boundary conditions of the walls were varied by either being thermally insulated, of a constant temperature, adiabatic, or perfectly conducting. The computations for

this air-filled 3-D enclosure were computed at Rayleigh numbers of 10^5 and 10^6. The authors discussed how, through computations, it is relatively easy to specify clearly defined boundary conditions; however, it is much more difficult to achieve the same results through well-controlled experiments. For example, in an actual experiment, a perfect insulator at a wall cannot be realized. Also, heat transfer through adiabatic surfaces is always present, which causes direct comparisons between computations and experimental results difficult. Therefore, in order to compare the two results, they are limited to the difference between idealized computational conditions and real experimental situations. An example for the boundary conditions of a 3-D enclosure with the varying boundary conditions can be shown in Figure III-6.

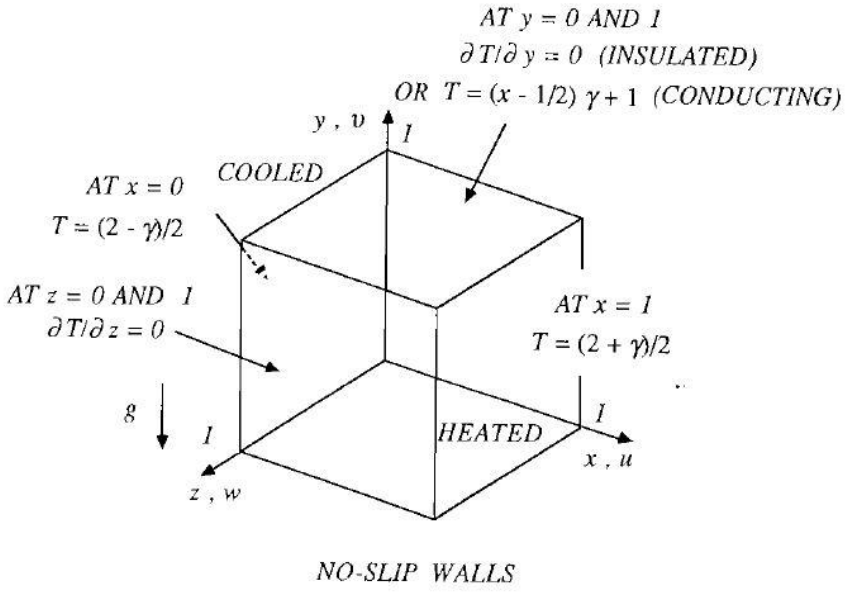

Figure III-6 3-D Enclosure Geometry and Boundary Conditions. Note. Reprinted from "A numerical study of 3D natural convection in a cube: effects of the horizontal thermal boundary conditions", by Fusegi, T. et al., 1991, Fluid Dynamics Research, 8, p. 222.

Fusegi et al. (1991) concluded that the adiabatic and perfectly conducting boundary conditions on the horizontal walls greatly influence the flow inside the enclosure. When heat transfer was allowed at the horizontal wall, the flow was greatly intensified.

The final aspect to analyze is the combination of the last three topics of discussion: fire modeling for enclosures. Wickstrom et al. (2007) introduces an adiabatic surface temperature as a means to transfer data from fire models to thermal/structural models. The authors state that the adiabatic surface temperature can be obtained as an output from a fire model, and that it can be measured in real fire tests or experiments by the use of a plate thermometer. Therefore, the adiabatic surface temperature would be measured by an ideal plate thermometer. The plate thermometer is used in fire resistance testing (E119 and ISO834) to control the furnace temperature. The temperature measured by the plate thermometer is required in the calculation of the exposed structural element.

Wickstrom (1985) analyzed the temperature of heavily insulated steel structures that were exposed to fire. He applied the ISO 834 Fire Curve to the insulation surface and crafted a 1-D model, Figure III-7, for conductive heat transfer.

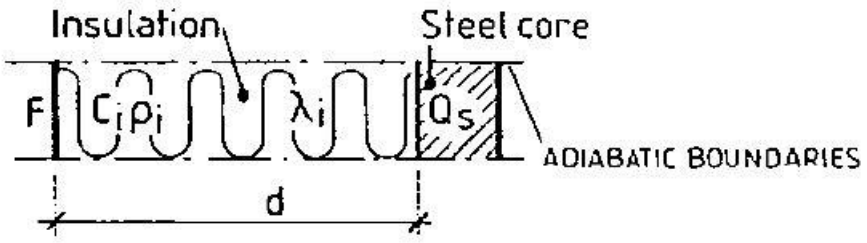

Figure III-7 1-D Model for Heat Conduction. Note. Reprinted from "Temperature Analysis of Heavily-Insulated Steel Structures Exposed to Fires", by Wickstrom, U., 1985, Fire Safety Journal, 9, p. 281.

His research concluded that the material properties at elevated temperatures were a necessary aspect for finding the temperature of the insulation and steel.

Zhang and Li (2012) presented a 1-D model with the addition of radiation and convection, as seen below in Figure III-8.

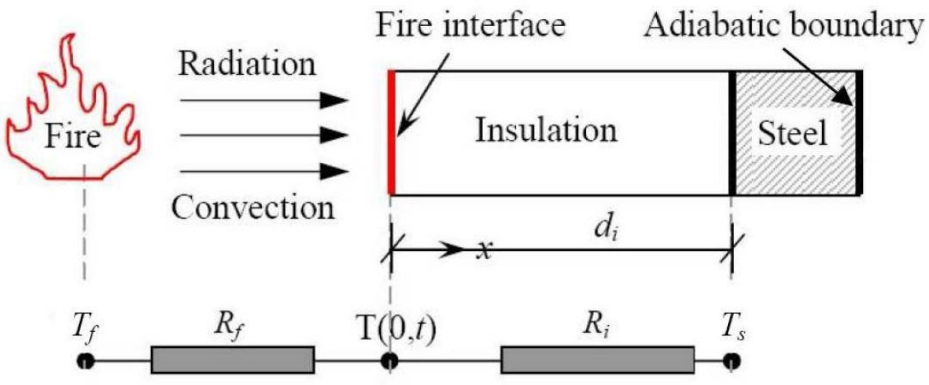

Figure III-8 1-D Condensed Heat Transfer Model. Note. Reprinted from "Modified One Zone Model for Fire Resistance Design of Steel Structures", by Zhang, C., 2012, Advanced Steel Construction, 9, p. 284.

The model in Figure III-8 can be computed via techniques such as the finite differential method (FDM) and the finite element method (FEM). These researchers utilized ANSYS in order to solve their proposed model.

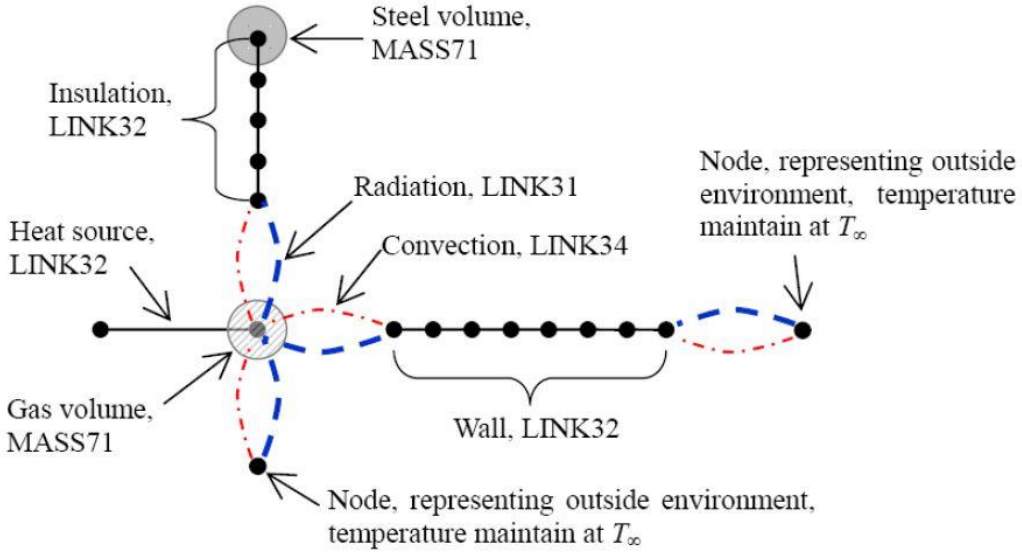

Figure III-9 FEM Model. Note. Reprinted from "Modified One Zone Model for Fire Resistance Design of Steel Structures", by Zhang, C., 2012, Advanced Steel Construction, 9, p. 290.

In their research, Zhang and Li described a finite element model for modeling the fire resistance of a steel structure, as mentioned below:

> "Starting with LINK32, in Figure III-9, the conduction bar, it is a uniaxial element which conducts heat between its nodes. It has one singled degree of freedom which is temperature at each point. It is applicable to 2D, steady-state or transient thermal analysis. The element has two nodes with a cross-sectional area, and material properties. The thermal conductivity is in the element's longitudinal direction. Also, heat generation rates can be inputted as element body loads at the nodes" (p. 289). "The next element is LINK34, in Figure III-9, or the convection link. This link is a uniaxial element that convects heat between its two nodes. It has a single degree of freedom, the temperature at both points. This convection element can be applied to a 2D or 3D, steady-state or transient thermal analysis. The element has two nodes, a convective surface area, two empirical terms, and a film coefficient" (p. 289). "LINK31 is the radiation link, in Figure III-9, it's a uniaxial element which models the radiation heat flow rate between two different points. This link has a single degree of freedom, the temperature at both points. This radiation element can be applied to a 2D or 3D, steady-state or transient thermal analysis. The element has two nodes, a radiating surface area, a geometric form factor, emissivity, and the Stefan-Boltzman constant" (p. 289). "Finally, MASS71, in Figure III-9, is a point element that has one degree of freedom, the temperature at the node. This element can be used in a transient thermal analysis to represent a body having thermal capacitance capability but negligible internal thermal resistance. This means that no significant temperature gradients within the body. This element can be applied to 1D, 2D, or 3D steady-state or transient thermal analysis. This lumped thermal mass element is defined by one node and a thermal capacitance" (Zhang and Li, p. 289-290, 2012).

The model in Zhang and Li (2012) concludes that the presence of steel in a fire compartment will act as a heat sink and thus lower the overall temperature in the room. It's found that, when fire compartments have insulated steel members, the steel heat sink effect is greater when there is a large floor area, a smaller opening, higher fire load density, and more steel members with thinner insulation (Zhang and Li, 2012).

The Marine Safety Laboratories for the United States Coast Guard conducted multiple tests in order to obtain information on the passage of flame, smoke, and heat through penetrations in deck assemblies (Beene et al., 1988). The furnace for testing can be seen in Figure III-10 below. An example of a test specimen is also shown in Figure III-11. In Beene et al. (1988), Class A-60 deck assemblies consisted of the penetrant, the steel plate, and approved structural insulation attached to the penetration assembly. There were 18 combinations of penetration types that were evaluated in 38 fire tests. Eight penetrations were tested for a A-0 rating and thirty were tested for A-60 rating. Nine of those tested were insulated on the fire side, eighteen were insulated on the non-fire side, and three were only partially insulated. From this experiment, six of eight penetrations passed the A-0 rating. Four of nine penetrations on the fire side passed the A-60 rating and all eighteen insulated on the non-fire side failed the requirements for A-60 (Beene et al., 1988).

After testing multiple penetrations, it was found that many did not meet the A-60 rating. These penetrations failed due to an excessive heat rise on the non-fire wall. Because of this, the assemblies with penetrations were then downgraded to A-15 ratings or even to B-15 ratings. The penetrations that were able to obtain an A-60 rating had additional insulation surrounding part of the penetration (Beene et al., 1988). From these results, it can be concluded that it is necessary for insulation to be on the fire side (Beene et al., 1988).

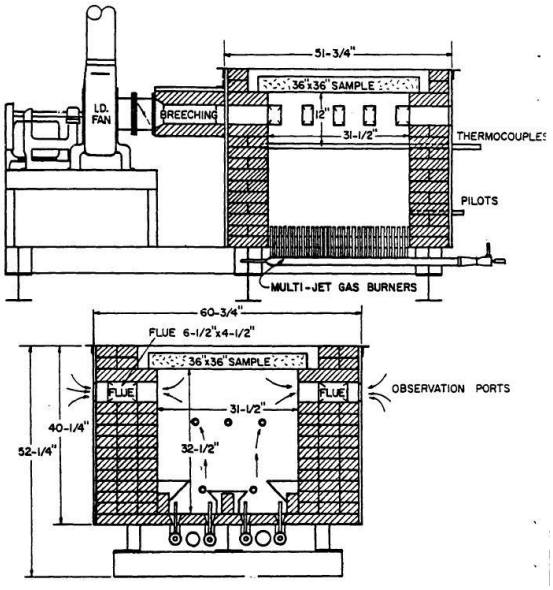

Figure III-10 Small Scale Horizontal Exposure Furnace/Underwriter's Laboratories 1 m Furnace. Note. Reprinted from "Fire Resistance Testing of Bulkhead and Deck Penetrations", by Beene, D. et al., Year, Marine Safety Laboratories, p. C-12.

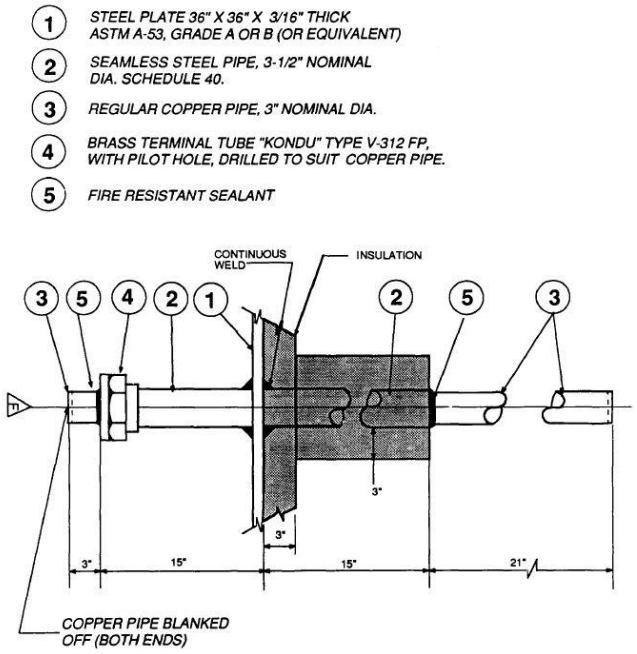

Figure III-11 Test Piece for Fire Test Note. Reprinted from "Fire Resistance Testing of Bulkhead and Deck Penetrations", by Beene, D. et al., Year, Marine Safety Laboratories, p. C-15.

Modeling a fire and the structural response to that fire are highly complex processes. The temperature and duration of a fire are both influenced by multiple factors and can have different effects on the structures surrounding them. When modeling a fire and its structural response, it is important to be aware of the temperature's rise and behavior, the thermal properties of the structure, and the ensuing convection currents created by the temperature rise. These items can lead to proper modeling of a ship structure's response to a fire. The research delineated above is crucial to providing background into the components of this thesis.

IV. Mathematical Modeling

Two different approaches were utilized to solve the proposed model. The first approach is a lumped capacitance model and the second uses ANSYS FLUENT with fluid structure interaction. These two methods are then compared and contrasted.

Fundamentals of Heat and Mass Transfer by Incropera et al. (2007) shows that the lumped capacitance method assumes that the temperature of the solid is spatially uniform at any time during the transient process. This method neglects spatial gradients in the solid. The resulting temperatures calculated by the lumped capacitance method represent spatial averages of temperature within each domain. The next assumption is that the resistance to conduction in the solid is insignificant compared to the resistance to heat transfer between the solid and what surrounds it. Finally, according to Fourier's law, when there is an absence of a temperature gradient in heat conduction, infinite thermal conductivity can be implied (Fundamentals of Heat and Mass Transfer, 2007).

The second method is Computational Fluid Dynamics (CFD) with fluid structure interaction. CFD is adept at predicting fluid flow and heat and mass transfer. It accomplishes this by approximating the set of governing differential equations such as the mass, momentum, and energy conservation equations. ANSYS Fluent solves these governing differential equations by using the finite volume method. This means that the domain is discretized into a finite set of control volumes. Then the conservation equations for mass, momentum, and energy are solved on this set of control volumes.

$$\frac{\partial}{\partial t}\int_V \rho\phi dV + \oint_A \rho\phi \mathbf{V}\cdot d\mathbf{A} = \oint_A \Gamma\nabla\phi\cdot d\mathbf{A} + \int_V S_\phi dV \tag{1.1}$$

The terms from left to right are as follows; unsteady, convection, diffusion, and generation. Fluent then will discretize the partial differential equations into a system of algebraic equations. These algebraic equations are then solved numerically in order to render a solution field (Introduction to CFD Methodology, 2010).

A. Lumped Capacitance Model

In order to establish a baseline for the heat transfer modeling proposed, a lumped capacitance model was formed. A lumped capacitance model applies the first law of thermodynamics to an unsteady system. The lumped capacitance model ignores spatial gradients, such as conduction in the body. The purpose of this model is to investigate whether a simplified lumped capacitance model can adequately simulate a fire. The thickness of the insulation, 102 mm, was found in a material properties table listed in Heating, Ventilating, and Air Conditioning Analysis and Design (2005, p. 126). The thickness of the steel, 5 mm, was determined by the testing procedures described in NVIC 9-97. The lumped capacitance model is then contrasted with the CFD model. Figure IV-1 shows the physical model tested using the lumped capacitance method.

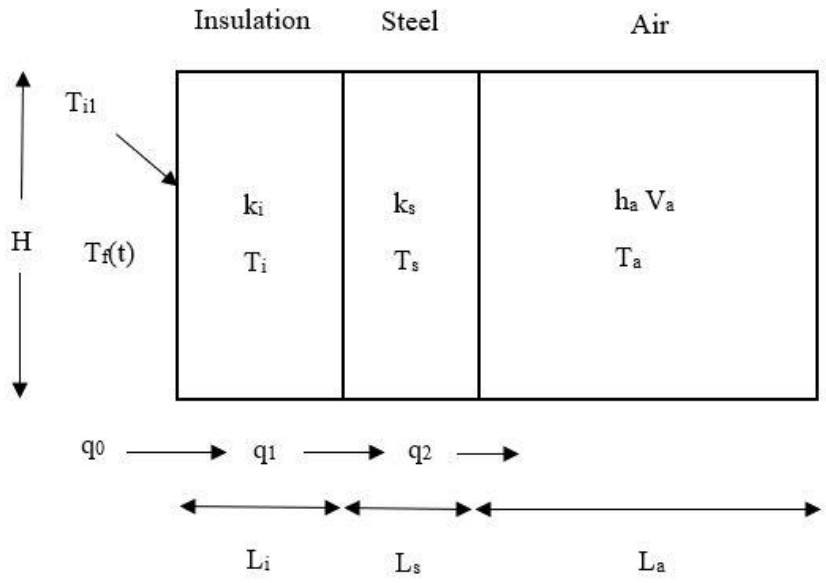

Figure IV-1 Lumped Capacitance Model

$$V_a = L_a \times H \times 1 \tag{1.2}$$

For (1.2) the value 1 is the unit depth. In order to develop a lumped capacitance model, the 1st law of Thermodynamics has to be written for each material (insulation, steel, and air). Figure IV-2 through Figure IV-4 show the heat flux through each material.

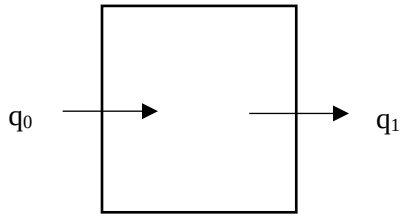

Figure IV-2 Lumped Capacitance Heat Flux Insulation

$$q_0 - q_1 = m_i c_{pi} \frac{dT_i}{dt} \tag{1.3}$$

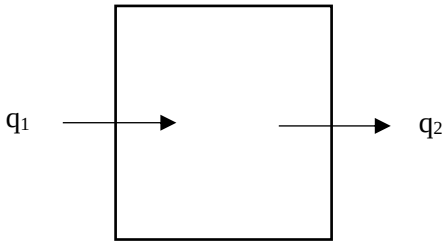

Figure IV-3 Lumped Capacitance Heat Flux Steel

$$q_1 - q_2 = m_s c_{ps} \frac{dT_s}{dt} \tag{1.4}$$

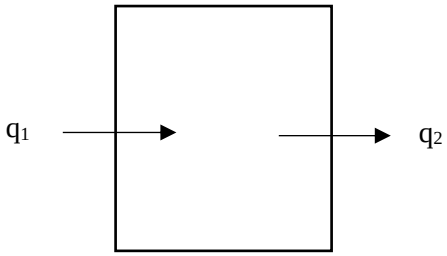

Figure IV-4 Lumped Capacitance Heat Flux Air

$$q_2 = m_a c_{pa} \frac{dT_a}{dt} \tag{1.5}$$

This is a system of 3 differential equations for T_s , T_i, and T_a as functions of time. In order to close the set of equations, expressions for q_0 , q_1 , and q_2 as functions of time also need to be approximated. The heat transfer q_0 into the wall could be modeled with a confection coefficient as:

$$q_0 = h_f A(T_f - T_i) \tag{1.6}$$

However, the heat flux is approximated assuming that the surface at the insulation is at the fire temperature T_f and uses a conduction approximation. This is written as (Fourier's Law):

$$q_0 = \kappa_i A \left(\frac{T_f - T_i}{\frac{L_i}{2}} \right) \tag{1.7}$$

At the interface between the steel and insulation, the heat flux is also approximated by using Fourier's Law:

$$q_1 = \bar{\kappa} A \left[\frac{T_i - T_s}{\frac{1}{2}(L_i + L_s)} \right] \tag{1.8}$$

The quantity $\bar{\kappa}$ represents the average thermal conductivity at the interface. The harmonic average is often used and given by (Patankar, 1980):

$$\bar{\kappa} = \frac{2\kappa_i \kappa_s}{\kappa_i + \kappa_s} \tag{1.9}$$

The heat flux q_2 is the natural convection coefficient involving the Raleigh Number as well as $(T_s - T_a)$.

$$q_2 = h_a A(T_s - T_a) \tag{1.10}$$

This is found from the Nusselt Number for the air (Nu_a). The Nusselt number is the dimensionless temperature gradient at the surface. It also allows convective heat transfer to be measured at the surface. The Grashof number (Gr) is the ratio of buoyancy forces to viscous forces in the velocity boundary layer. The Prandtl number (Pr) is the ratio of momentum diffusivity ν to the thermal diffusivity α. The Prandtl number also provides "a measure of the relative effectiveness of momentum and energy transport by diffusion in the velocity and thermal boundary layers" (Incropera et al., 2007, p. 375). The Rayleigh number (Ra) represents the relative magnitude of the buoyancy and viscous forces in a fluid. The Rayleigh number is the product of the Grashof and Prandtl numbers (Incropera et al., 2007).

$$\mathrm{Nu_a} = \left[0.865 + \frac{0.387\mathrm{Ra}^{1/6}}{\left[1+(0.429/\mathrm{Pr})^{9/16}\right]^{8/27}} \right]^2 \tag{1.11}$$

$$\mathrm{Ra}=\mathrm{GrPr} \tag{1.12}$$

$$\mathrm{Gr} = \frac{H^3 \rho^2 g (T_s - T_a)\beta}{\mu^2} \tag{1.13}$$

$$H = vertical\ height\ of\ wall$$

$$\beta = \frac{1}{T_a}\ (T_a\ in\ absolute\ temperature)$$

The volume of each section is $(L)(H)(1)$ and the cross-sectional area is $A = H(1)$.

$$\dot{m} = \rho V = \rho L H(1) \tag{1.14}$$

Therefore, the system of equations can be written as:

$$\frac{dT_i}{dt} = \frac{2\kappa_i}{\rho_i c_{pi} L_i^2} \times \left(T_f - T_i\right) - \frac{\bar{\kappa}}{\rho_i c_{pi} L_i} \times \left[\frac{T_i - T_s}{\frac{1}{2}\left(L_i + L_s\right)} \right] \tag{1.15}$$

$$\frac{dT_s}{dt} = \frac{\bar{\kappa}}{\rho_s c_{ps} L_s} \times \left[\frac{T_i - T_s}{\frac{1}{2}(L_i + L_s)} \right] - \frac{h_a}{\rho_s c_{ps} L_s} \times (T_s - T_a) \tag{1.16}$$

$$\frac{dT_a}{dt} = \frac{h_a}{\rho_a c_{pa} L_a} \times \left(T_s - T_a \right) \tag{1.17}$$

The initial conditions are $T_i(0), T_s(0), T_a(0) = T_0$.

1. Thermal Conductivity Model

In order to create a more realistic model, the thermal conductivity of both the insulation and steel are made temperature dependent. This was accomplished using piecewise polynomial functions. According to Jansson (2004), the measurements for thermal conductivity for the insulation are stated in Table IV-1:

Table IV-1 Temperature vs. Thermal Conductivity of Insulation. Adapted from "Measurement of thermal properties at elevated temperatures", by Jansson, R., 2004, Swedish National Testing and Research Institute, p. 86.

Temperature (K)	Conductivity (W/mK)
293.15	0.064
363.15	0.075
383.15	0.08
473.15	0.1
573.15	0.14
773.15	0.27
873.15	0.36

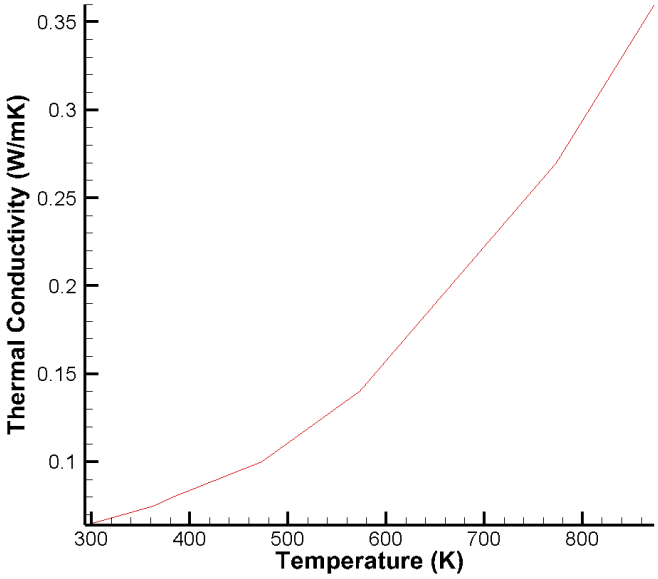

Figure IV-5 Thermal Conductivity vs. Temperature of Insulation. Adapted from "Measurement of thermal properties at elevated temperatures", by Jansson, R., 2004, Swedish National Testing and Research Institute, p. 89.

Figure IV-5 is a visual representation of how an increasing temperature affects the thermal conductivity of insulation. A second order polynomial was then used to approximate the curve in order to input a thermal conductivity verses temperature relationship. This relationship is depicted in Figure IV-5. Since the fire temperature is in excess of 873.15 K, a linear trendline was found for the last two points on the graph above.

When $T_i \le 873.15\,K$ then:

$$\kappa = 8\times10^{-7}T_i^2 + 0.0004T_i + 0.1213 \tag{1.18}$$

When $T_i > 873.15\,K$ then:

$$\kappa = 0.0009T_i - 0.425835 \tag{1.19}$$

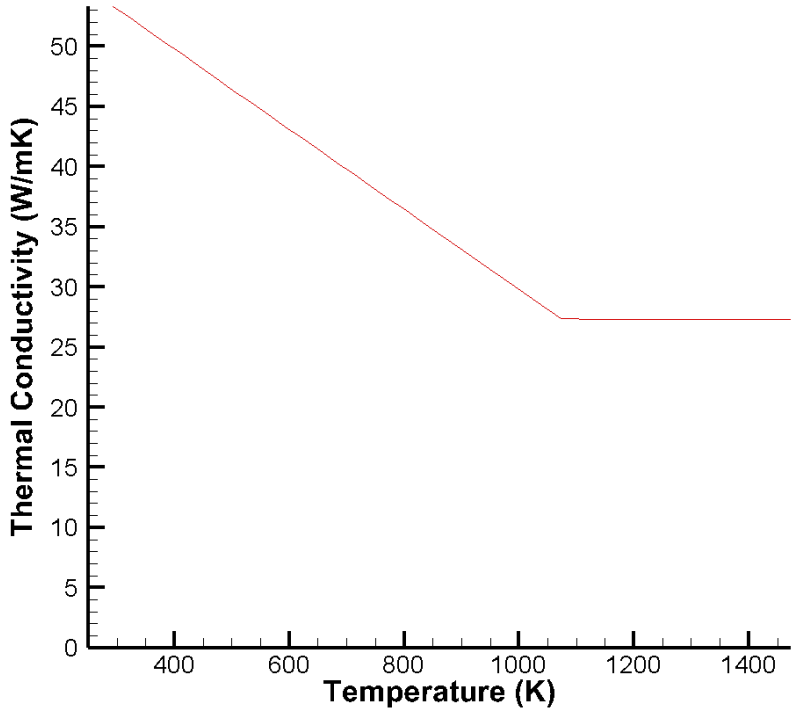

Figure IV-6 Thermal Conductivity vs. Temperature of Steel. Adapted from Fire Design of Steel Structures (321), by J. Franssen and P.V. Real, 2012, European Convention for Constructional Steelwork.

According to Franssen and Real (2012), Figure IV-6 is the thermal conductivity of steel with the ISO 834 Standard Fire Curve applied.

When $T_s < 1073.5\,K$ then:

$$\kappa = 54 - 0.033(T_s - 273.15) \tag{1.20}$$

When

$T_s \geq 1073.5\,K$ then:

$$\kappa = 27.3 \tag{1.21}$$

The fire equation is:

$$T_f(t) = 345\log_{10}(8t+1) + 20 \tag{1.22}$$

2. Runge-Kutta Method

The lumped capacitance model results in a coupled system of 1st Order Ordinary Differential Equations, which are solved with a 4th Order Runge-Kutta method. The Runge-Kutta method solves a system of equations of the form:

$$\frac{dT_j}{dt} f\left(t, T_j\right) j = 1, 2, 3...(i, s, a) \tag{1.23}$$

There are many variants of the Runge-Kutta method, but a common one is the 4th order method. If the current (known) time level is t^n, then the solution is advanced to the new or unknown level by intermediate evaluations of T with various weighed values applied. In order to achieve stability, the timestep size was experimented within the code. The largest timestep size was selected because it produced a stable and converged solution.

The solution T^n at t^n is assumed known. This solution T^{n+1} at t^{n+1} is found as follows:

Simulation time $0 \le t \le t_{final}$ choose t_{final} & Δt to satisfy stability constraints

Timestep: $\Delta t = t^{n+1} - t^n$

The Runge-Kutta method advances the solution from time level t^n to time level t^{n+1} by defining the following intermediate values:

$$k_{11j} = \Delta t f\left(t^n, T_j^n\right) \tag{1.24}$$

$$k_{21j} = \Delta t f\left(t^n + \frac{1}{2}\Delta t, T_j^n + \frac{1}{2}k_{11j}\right) \tag{1.25}$$

$$k_{31j} = \Delta t f\left(t^n + \frac{1}{2}\Delta t, T_j^n + \frac{1}{2}k_{21j}\right) \tag{1.26}$$

$$k_{41j} = \Delta t f\left(t^n + \Delta t, T_j^n + k_{31j}\right) \tag{1.27}$$

The solution at t^{n+1} is then written as:

$$T_j^{n+1} = T_j^n + \frac{1}{6}k_1 + \frac{1}{3}k_2 + \frac{1}{3}k_3 + \frac{1}{6}k_4 \tag{1.28}$$

The solution is advanced from $t = 0$ to $t = t_{final}$, the final simulation time. The number of time steps used is $\frac{t_{final}}{\Delta t}$.

The solution algorithm proceeds as follows:

1. Set the total simulation time, t_{final}
2. Set the number of time steps, N_t. $\Delta t = \frac{t_{final}}{N_t}$
3. Calculate k_1, k_2, k_3, and k_4 at times required by the Runge-Kutta Method by evaluating $f(t,T)$ at appropriate conditions. Do for equations (1.15) - (1.17) sequentially.
4. Update T_i, T_s, and T_a to $n+1$ using weighted update formula
5. Repeat 1-4 until t_{final} is reached

B. Lumped Capacitance Parallel Flow

The Lumped Capacitance Parallel Flow model utilizes the same procedure as the Lumped Capacitance model, but with the addition of an attachment protruding from the steel through the insulation.

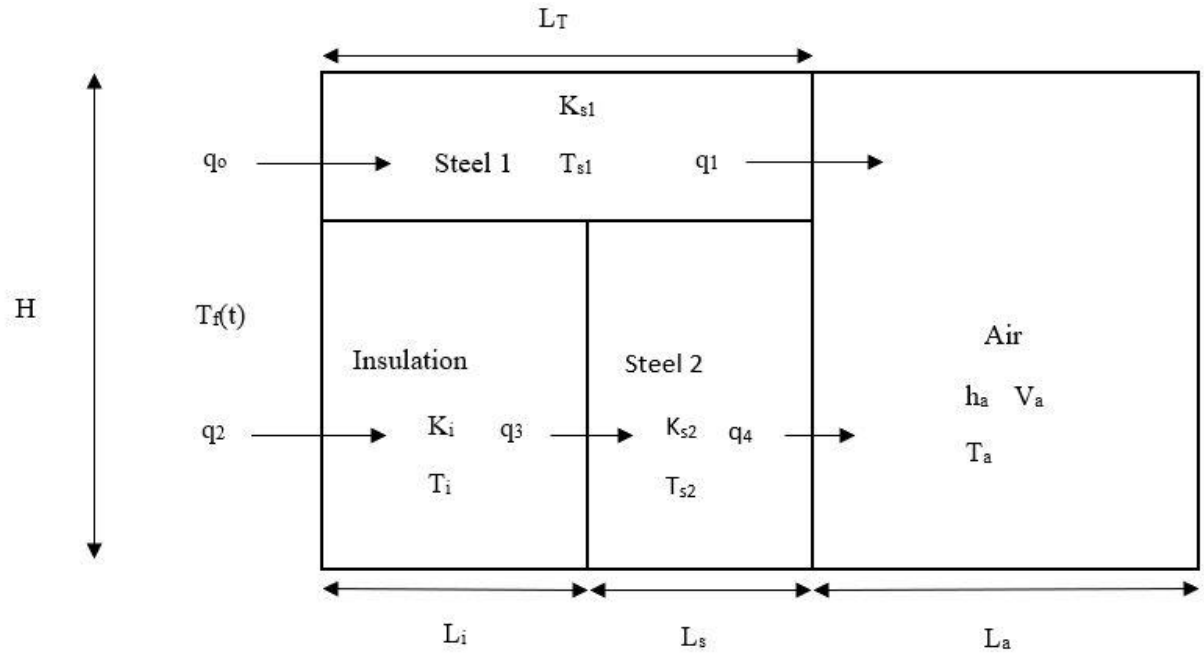

Figure IV-7 Lumped Capacitance Parallel Flow Model

$$L_T = L_i + L_s \tag{1.29}$$

A_s = Area of Steel Exposed to $T_f \left(m^3\right)$

A_i = Area of Insulation Exposed to $T_f \left(m^3\right)$

Because the Parallel Flow Model uses the same mathematical formulation as the Lumped Capacitance Model, equations (1.3) - (1.13) can be referenced. Figure *IV-8* through Figure *IV-11* show the separate heat flux through the different materials.

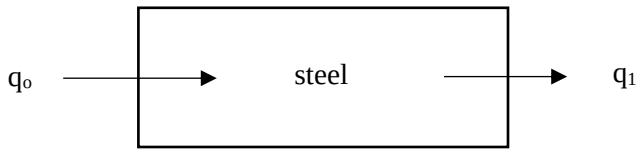

Figure IV-8 Lumped Capacitance Heat Flux Attachment

$$q_0 - q_1 = m_{s1} c_{ps1} \frac{dT_{s1}}{dt} \tag{1.30}$$

This is a system of 3 differential equations for T_{s1}, T_{s2}, T_i, and T_a as functions of time. In order to close the set of equations, expressions for q_0 , q_1 , q_2, and q_3 as functions of time also need to be approximated. The heat transfer q_0 into the wall could be modeled with a convection coefficient as shown in (1.6). However, the heat flux is approximated by assuming that the surface at the insulation is at the fire temperature T_f and by using a conduction approximation. This is written as Fourier's Law:

$$q_0 = \kappa_s A_{s1} \left(\frac{T_f - T_{s1}}{\frac{L_T}{2}} \right) \tag{1.31}$$

The heat flux q_1 is the natural convection coefficient involving the Raleigh Number as well as $\left(T_{s1} - T_a\right)$:

$$q_1 = h A_{s1} \left(T_{s1} - T_a\right) \tag{1.32}$$

The natural convection coefficient can be found by referencing equations (1.11) - (1.13). Then finally referencing equation (1.14) yields:

$$\frac{dT_{s1}}{dt} = \frac{2\kappa_s}{\rho_s c_{ps} L_T^2}\left(T_f - T_{s1}\right) - \frac{h}{\rho_s c_{ps} L_T}\left(T_{s1} - T_a\right) \tag{1.33}$$

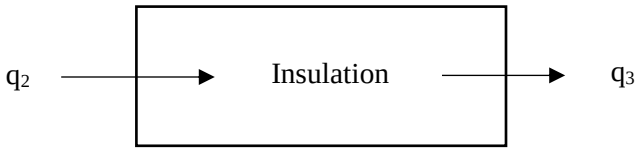

Figure IV-9 Lumped Capacitance Heat Flux Insulation

$$q_2 - q_3 = m_i c_{pi} \frac{dT_i}{dt} \tag{1.34}$$

Again, the heat flux is approximated by assuming that the surface of the insulation is at the fire temperature T_f and by using a conduction approximation. This is written by use of Fourier's Law:

$$q_2 = \kappa_i A_i \left(\frac{T_f - T_i}{\frac{L_i}{2}} \right) \tag{1.35}$$

At the interface between the insulation and steel, the heat flux is also approximated by using Fourier's Law. Referencing the harmonic average (1.9):

$$q_3 = \bar{\kappa} A_i \left(\frac{T_i - T_{s2}}{\frac{1}{2}\left(L_T\right)} \right) \tag{1.36}$$

Therefore, the equation can be written as:

$$\frac{dT_i}{dt} = \frac{2\kappa_i}{\rho_i c_{pi} L_i^2}\left(T_f - T_i\right) - \frac{\bar{\kappa}}{\rho_i c_{pi} L_i} \frac{T_i - T_{s2}}{\frac{1}{2} L_T} \tag{1.37}$$

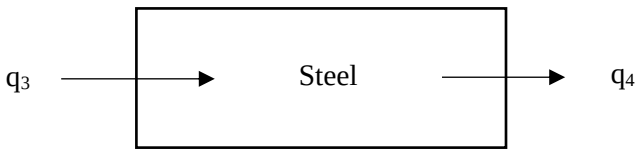

Figure IV-10 Lumped Capacitance Heat Flux Steel

$$q_3 - q_4 = m_s c_{ps} \frac{dT_{s2}}{dt} \tag{1.38}$$

The heat flux q_4 is the natural convection coefficient involving the Raleigh Number as well as $(T_{s2} - T_a)$:

$$q_4 = hA_i (T_{s2} - T_a) \tag{1.39}$$

The natural convection coefficient can be found by referencing equations (1.11) - (1.13). Then finally referencing equation (1.14) yields:

$$\frac{dT_{s2}}{dt} = \frac{\bar{\kappa}}{\rho_s c_{ps} L_s} \frac{T_i - T_{s2}}{\frac{1}{2} L_T} - \frac{h}{\rho_s L_s c_{ps}} (T_{s2} - T_a) \tag{1.40}$$

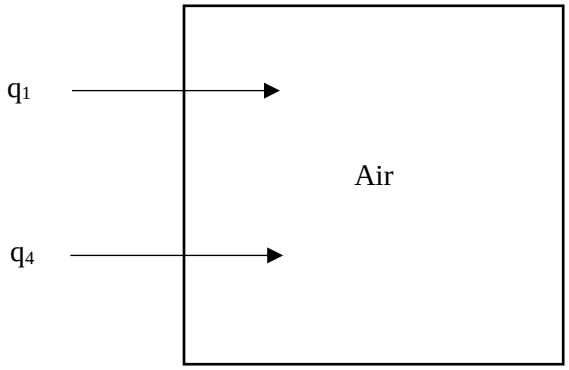

Figure IV-11 Lumped Capacitance Heat Flux Air

$$q_1 + q_4 = m_a c_{pa} \frac{dT_a}{dt} \tag{1.41}$$

The system of equations can then be written by adding the two heat fluxes from the parallel paths that travel into the air:

$$\frac{dT_a}{dt} = \frac{hA_s}{\rho_a V_a c_{pa}} (T_{s1} - T_a) + \frac{hA_i}{\rho_a V_a c_{pa}} (T_{s2} - T_a) \tag{1.42}$$

The initial conditions are $T_i(0), T_{s1}(0), T_{s2}(0), T_a(0) = T_0$.

The same 4th Order Runge-Kutta Method was then applied to equations (1.33), (1.37), (1.40), and (1.42).

C. CFD Model

1. Solver Theory

The CFD model is solved using ANSYS Fluent. ANSYS Fluent uses a finite volume method to solve the Navier-Stokes equations. This program solves the mass, momentum, and energy conservation equations. When heat transfer or compressibility is present, the energy conservation equation is then solved. The following equations are the general equations that ANSY FLUENT solves; they are not the governing differential equations for this thesis. Starting with the mass conservation equation:

$$\frac{\partial \rho}{\partial t} + \nabla \cdot \left(\rho \vec{v} \right) = S_m \tag{2.1}$$

The next equation solved is the conservation of momentum:

$$\frac{\partial}{\partial t}\left(\rho \vec{v} \right) + \nabla \cdot \left(\rho \vec{v}\vec{v} \right) = -\nabla p + \nabla \cdot \left(\bar{\bar{\tau}} \right) + \rho \vec{g} + \vec{F} \tag{2.2}$$

According to ANSYS Fluent Theory Guide, "p is the static pressure, $\bar{\bar{\tau}}$ is the stress tensor, and $\rho \vec{g}$ and $\vec{F}$ are the gravitational body force and the external body forces" (2009).

The stress tensor $\bar{\bar{\tau}}$ is given by:

$$\bar{\bar{\tau}} = \mu \left[\left(\nabla \vec{v} + \nabla \vec{v}^{T} \right) - \frac{2}{3} \nabla \cdot \vec{v} I \right] \tag{2.3}$$

The conservation of energy equation solved is:

$$\frac{\partial}{\partial t}\left(\rho E \right) + \nabla \cdot \left[\vec{v}\left(\rho E + p \right) \right] = \nabla \cdot \left[\kappa_{eff} \nabla T - \sum_j h_j \vec{J_j} + \left(\bar{\bar{\tau}}_{eff} \cdot \vec{v} \right) \right] + S_h \tag{2.4}$$

For this equation, κ_{eff} is the effective conductivity ($\kappa + \kappa_t$, where κ_t is the turbulent thermal conductivity defined by the turbulence model used). $\vec{J_j}$ is the diffusion flux of species j. For the energy

equation, the first three terms on the right-hand side represent energy transfer due to conduction, species diffusion, and viscous dissipation. The term S_h includes the heat of chemical reaction and other volumetric heat sources that are defined (ANSYS Fluent Theory Guide, 2009).

In Equation (2.4), the energy term is as follows:

$$E = h - \frac{p}{\rho} + \frac{v^2}{2} \tag{2.5}$$

The sensible enthalpy h is defined for ideal gases as:

$$h = \sum_j Y_j h_j \tag{2.6}$$

For incompressible flows:

$$h = \sum_j Y_j h_j + \frac{p}{\rho} \tag{2.7}$$

For Equations (2.6) and (2.7), Y_j is the mass fraction of species j:

$$h_j = \int_{T_{ref}}^{T} c_{p,j} dT \tag{2.8}$$

For Equation (2.8), T_{ref} is 298.15 K.

For solid regions, ANSYS FLUENT solves the following energy transport equation:

$$\frac{\partial}{\partial t}(\rho h) + \nabla \cdot (\vec{v} \rho h) = \nabla \cdot (k \nabla T) + S_h \tag{2.9}$$

The second term on the left-hand side of Equation (2.9) represents convective energy transfer due to rotational or translational motion of the solids. The velocity field $\vec{v}$ is computed from the motion

specified for the solid zone. For the right-hand side of Equation (2.9), the terms are the heat flux due to conduction and the volumetric heat sources within the solid (ANSYS Fluent Theory Guide, 2009).

ANSYS FLUENT will then use a control-volume-based technique in order to convert a general scalar transport equation to an algebraic equation that can be solved numerically. This technique integrates the transport equation about each control volume and yields a discrete equation that expresses the conservation law on a control-volume basis (ANSYS Fluent Theory Guide, 2009). The transport equation can be written as:

$$\int_V \frac{\partial \rho\phi}{\partial t} dV + \oint \rho\phi\vec{v} \cdot d\vec{A} = \oint \Gamma_\phi \nabla\phi \cdot d\vec{A} + \int_V S_\phi dV \tag{2.10}$$

In this equation, ρ is the density, $\vec{v}$ is the velocity vector, $\vec{A}$ is the surface area vector, Γ_ϕ is the diffusion coefficient for ϕ, ∇_ϕ is the gradient of ϕ, and S_ϕ is the source of ϕ per unit volume. Equation (2.10) is applied to each control volume or cell for the computational domain (ANSYS Fluent Theory Guide, 2009). Discretization of equation (2.10) on a given cell yields:

$$\frac{\partial(\rho\phi)}{\partial t} V + \sum_f^{N_{faces}} \rho_f \vec{v}_f \phi_f \cdot \vec{A}_f = \sum_f^{N_{faces}} \Gamma_\phi \nabla_{\phi f} \cdot d\vec{A} + \int_V S_\phi dV \tag{2.11}$$

The term N_{faces} is the number of faces enclosing the cell, ϕ_f is the value of ϕ convected through face f, $\rho_f \vec{v}_f \cdot \vec{A}_f$ is the mass flux through the face, $\vec{A}_f$ is the area of face f, $\nabla_{\phi f}$ is the gradient of ϕ at face f, and V is the cell volume (ANSYS Fluent Theory Guide, 2009).

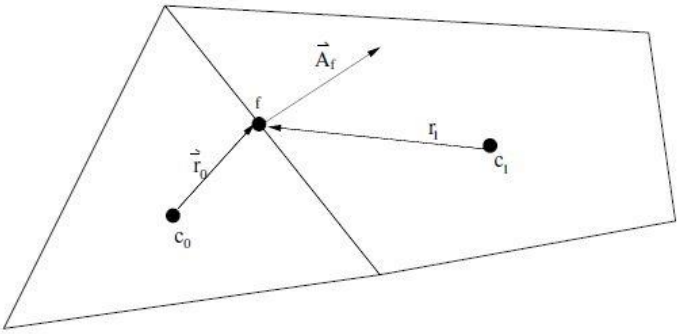

Figure IV-12 Control Volume for Discretization of Scalar Transport Equation. Reprinted from "ANSYS Fluent Theory Guide", p. 18-9.

Figure IV-12 is an example of how the scalar transport equation is discretized for a control volume. The previous equations were the general form. Once assumptions are applied, the equations simplify and become the governing differential equations for the proposed CFD model (ANSYS Fluent Theory Guide, 2009).

2. Fluent Convection

ANSYS Fluent uses multiple methods to solve convection. The two methods that will be used by this thesis are the Boussinesq approximation and the incompressible ideal gas law. The strength of the buoyancy forces is determined by the Rayleigh Number (FLUENT 6.3 User's Guide, 2006).

$$\mathrm{Ra} = \frac{g\beta\Delta T L^3 \rho}{\mu\alpha} \tag{2.12}$$

Where β is the thermal expansion coefficient:

$$\beta = -\frac{1}{\rho}\left(\frac{\partial\rho}{\partial T}\right)_p \tag{2.13}$$

For an ideal-gas, β is:

$$\beta = \frac{1}{T} \tag{2.14}$$

Where T is in absolute and α is the thermal diffusivity:

$$\alpha = \frac{k}{\rho c_p} \tag{2.15}$$

It should also be noted that when the Rayleigh number is less than 10^8, the flow is buoyancy-induced laminar. The flow will then transition to turbulent over the range of $10^8 < Ra < 10^{10}$ (FLUENT 6.3 User's Guide, 2006).

For many natural-convection flows, faster convergence is achieved with the Boussinesq approximation than by setting up the problem with fluid density as a function of temperature. This model treats density as a constant value in all solved equations, except for the buoyancy term in the momentum equation (FLUENT 6.3 User's Guide, 2006):

$$(\rho - \rho_0)g \approx -\rho_0\beta(T - T_0)g \tag{2.16}$$

For this equation ρ_0 is considered the constant density of the flow, T_0 is the operating temperature, and β is the thermal expansion coefficient. It should be noted that Equation (2.16) comes from the Boussinesq approximation (FLUENT 6.3 User's Guide, 2006):

$$\rho = \rho_0(1-\beta\Delta T) \tag{2.17}$$

This equation eliminates ρ from the buoyancy term. It can also be noted that the Boussinesq approximation is only accurate when the changes in density are small. The constraint for accuracy is (FLUENT 6.3 User's Guide, 2006):

$$\beta(T-T_0) \square\ 1 \tag{2.18}$$

In the event that the Boussinesq model cannot be used, the incompressible ideal gas model can be an appropriate choice. The relationship between density and temperature for this model can be defined as (FLUENT 6.3 User's Guide, 2006):

$$\rho = \frac{p_{\text{op}}}{\frac{R}{M_w}T} \tag{2.19}$$

3. Physical Model

For the physical model, the insulation was made 1 x 1 m with a thickness of 102 mm. The thickness of the insulation was determined from Heating, Ventilating, and Air Conditioning Analysis and Design (2005, p. 126). For the baseline model, there was an absence of an attachment. The attachment varied in surface area being either 6.25 cm^2, 25 cm^2, and 100 cm^2. The thickness of each attachment is 102 mm. The steel bulkhead was 1 x 1 m with a thickness of 5 mm (NVIC 9-97, 2010). Finally, the air section has the dimensions of 1 x 1 x 1 m. The physical model was designed as follows:

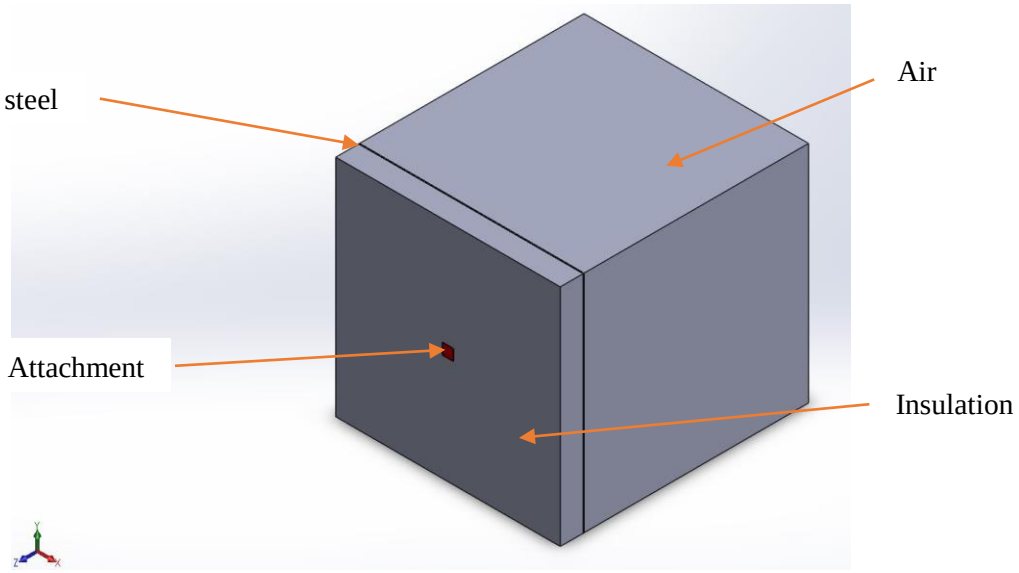

Figure IV-13 Fluid and Solid Region, CFD Model

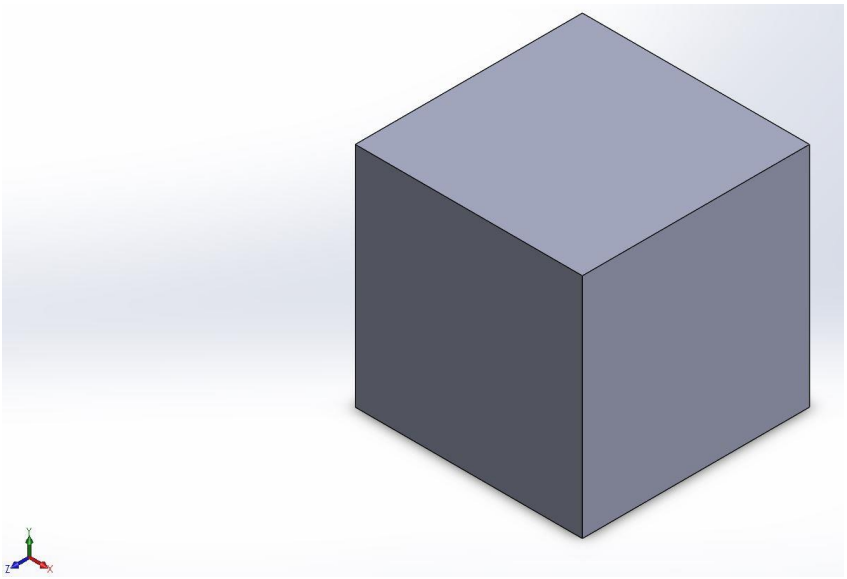

Figure IV-14 Fluid Region, CFD Model

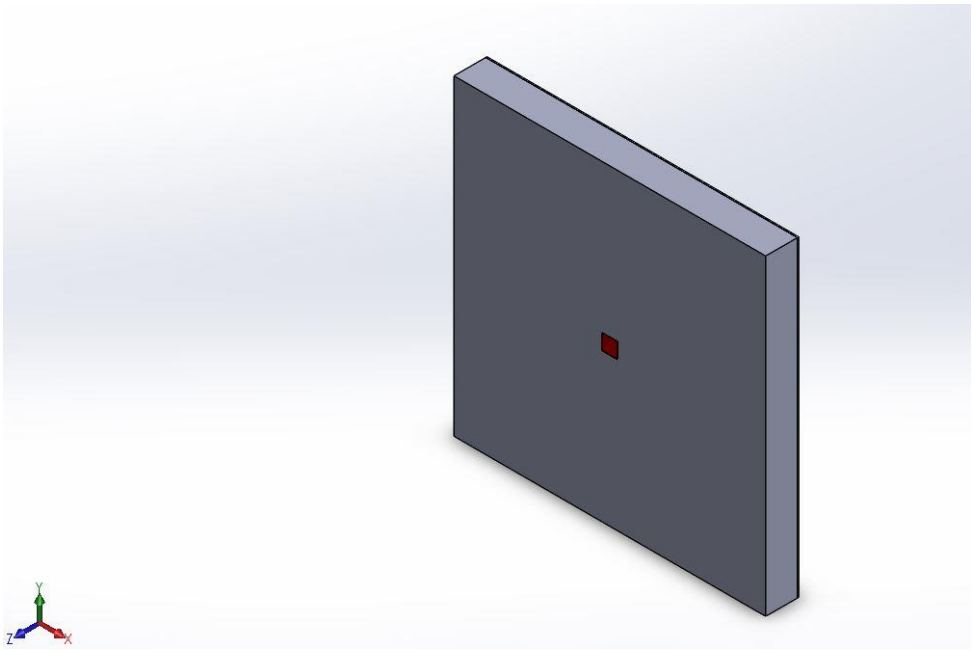

Figure IV-15 Solid Region, CFD Model

4. Governing Differential Equations and Boundary Conditions

The conservation equations of continuity, momentum, and energy have the following assumptions: 3-D Cartesian, unsteady, laminar, incompressible, Newtonian fluid, and subsonic flow. These equations are written in terms or primitive variables ρ, u, T and P, for the fluid region:

Continuity:

$$\frac{\partial u}{\partial x}+\frac{\partial v}{\partial y}+\frac{\partial w}{\partial z}=0 \tag{2.20}$$

Momentum:

$$X:\frac{\partial u}{\partial t}+u\frac{\partial u}{\partial x}+v\frac{\partial u}{\partial y}+w\frac{\partial u}{\partial z}=-\frac{1}{\rho}\frac{\partial p}{\partial x}+\nu\left(\frac{\partial^2 u}{\partial x^2}+\frac{\partial^2 u}{\partial y^2}+\frac{\partial^2 u}{\partial z^2}\right) \tag{2.21}$$

$$Z:\frac{\partial w}{\partial t}+u\frac{\partial w}{\partial x}+v\frac{\partial w}{\partial y}+w\frac{\partial w}{\partial z}=-\frac{1}{\rho}\frac{\partial p}{\partial z}+\nu\left(\frac{\partial^2 w}{\partial x^2}+\frac{\partial^2 w}{\partial y^2}+\frac{\partial^2 w}{\partial z^2}\right) \tag{2.22}$$

Boussinesq Approximation:

$$Y:\frac{\partial v}{\partial t}+u\frac{\partial v}{\partial x}+v\frac{\partial v}{\partial y}+w\frac{\partial v}{\partial z}=-\frac{1}{\rho}\frac{\partial p}{\partial y}+\nu\left(\frac{\partial^2 v}{\partial x^2}+\frac{\partial^2 v}{\partial y^2}+\frac{\partial^2 v}{\partial z^2}\right)+g\beta\left(T-T_o\right) \tag{2.23}$$

Incompressible Ideal Gas:

$$Y:\rho\left(\frac{\partial v}{\partial t}+u\frac{\partial v}{\partial x}+v\frac{\partial v}{\partial y}+w\frac{\partial v}{\partial z}\right)=-\frac{\partial p}{\partial y}+\mu\left(\frac{\partial^2 v}{\partial x^2}+\frac{\partial^2 v}{\partial y^2}+\frac{\partial^2 v}{\partial z^2}\right)+\left(\rho-\rho_o\right)g \tag{2.24}$$

Energy:

$$\frac{\partial T}{\partial t}+u\frac{\partial T}{\partial x}+v\frac{\partial T}{\partial y}+w\frac{\partial T}{\partial z}=\alpha\left(\frac{\partial^2 T}{\partial x^2}+\frac{\partial^2 T}{\partial y^2}+\frac{\partial^2 T}{\partial z^2}\right) \tag{2.25}$$

Boundary Conditions:

$$u = v = w = 0 \tag{2.26}$$

Boundary Condition (2.26) is applied to all of the solid walls except where symmetry was applied.

At $x = 0$ and 1, a symmetry boundary condition is applied:

$$\frac{d\phi}{dx} = 0 \tag{2.27}$$

Where $\phi = (T, u, v, w)$

At $y = 0$ and 1 and $z = 0$, an adiabatic boundary condition is applied:

$$\frac{\partial T}{\partial y} = 0 \tag{2.28}$$

$$\frac{\partial T}{\partial z} = 0 \tag{2.29}$$

For the interface between the fluid and solid regions, the interface condition imposes continuity of the heat flux:

$$q_s'' = q_f'' \tag{2.30}$$

$$-\kappa_f \nabla T_f = -\kappa_s \nabla T_s \tag{2.31}$$

The solid region has one governing differential equation: conservation of energy. For this region, a temperature-dependent thermal conductivity was assumed for the attachment, insulation, and steel. Both density and specific heat were held constant for all materials in the solid region.

Energy:

$$\rho c_p \frac{\partial T}{\partial t} = \left[\frac{\partial}{\partial x}\left(\kappa \frac{\partial T}{\partial x} \right) + \frac{\partial}{\partial y}\left(\kappa \frac{\partial T}{\partial y} \right) + \frac{\partial}{\partial z}\left(\kappa \frac{\partial T}{\partial z} \right) \right] \tag{2.32}$$

For the solid region consisting of the attachment, insulation, and steel bulkhead, the Boundary Conditions (2.27), (2.28), (2.29) apply as well.

Additionally, the standard time-temperature fire curve is applied at z = 1:

$$T = T_f(t) = 345 \log_{10}(8t + 1) + 20 \tag{2.33}$$

5. Solution Procedure

The governing differential equations are discretized and solved using the Pressure-Based solver. The equations solved are both non-linear and coupled. At each timestep, an iterative procedure is used to solve the governing differential equations. The algorithm for the Pressure-Based Solver is shown in Figure IV-16 (ANSYS Fluent Theory Guide, 2009):

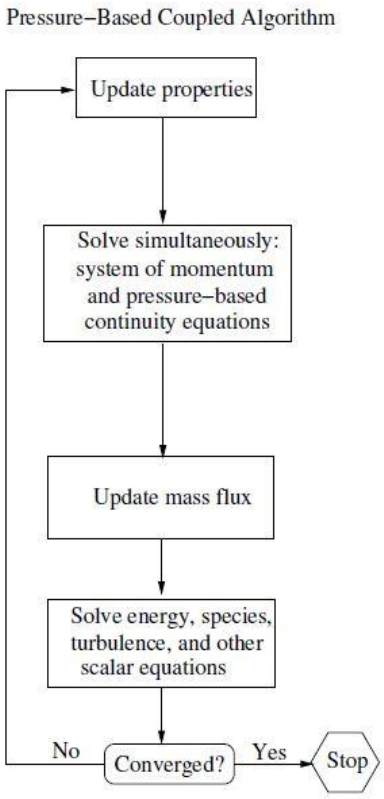

Figure IV-16 Pressure-Based Solution Method. Reprinted from "ANSYS Fluent Theory Guide", p. 18-4.

The pressure-based coupled algorithm solves the governing equations at each timestep. Since these equations are both non-linear and coupled, the solution loop needs to be solved iteratively to obtain a converged numerical solution. By solving the equations coupled, the rate of convergence is greatly improved (ANSYS Fluent Theory Guide, 2009).

The coupled algorithm is the suggested algorithm for solving convection problems in ANSYS Fluent (FLUENT 6.3 User's Guide, 2006). The coupled algorithm solves both the momentum equation and pressure-based continuity equation simultaneously. By implicit discretization of the pressure gradient terms in the momentum equations and implicit discretization of the face mass flux, a fully implicit coupling can be achieved (ANSYS Fluent Theory Guide, 2009). For this thesis a body-force-weighted pressure interpolation scheme was suggested and used (FLUENT 6.3 User's Guide, 2006). "The body-force-weighted scheme computes the face pressure by assuming that the normal gradient of the difference between pressure and body forces is constant" (ANSYS Fluent Theory Guide, 2009). Table IV-2 addresses the settings inputted into ANSYS Fluent.

Table IV-2 CFD Solver Settings

Time	Transient
Type	Pressure-Based
Models	Energy
Viscous	Laminar
Scheme	Coupled
Gradient	Least Squares Cell Based
Pressure	Body Force Weighted
Momentum	Second Order Upwind
Energy	Second Order Upwind

6. Mesh Formulation

Proper mesh creation is necessary to obtaining an accurate solution in ANSYS Fluent. The mesh represents the domain of the solution. The mesh also needs to be fine enough near the walls to properly capture phenomena such as boundary layer flow. This is accomplished by biasing the mesh. It is important to bias the mesh at the walls so that the boundary layer can be properly captured. For this project, the fluid domain was biased toward the steel bulkhead. The element size for this meshing was 0.025 m. The sweep for the insulation and attachment was 10 with no bias; the sweep for the air was 50 with a bias; and the steel had a sweep of 1 in order to maintain a conformal mesh. Figure IV-17 is a side view of the model. The figure shows how a very fine bias was applied at the wall in order to capture the boundary layer flow occurring there.

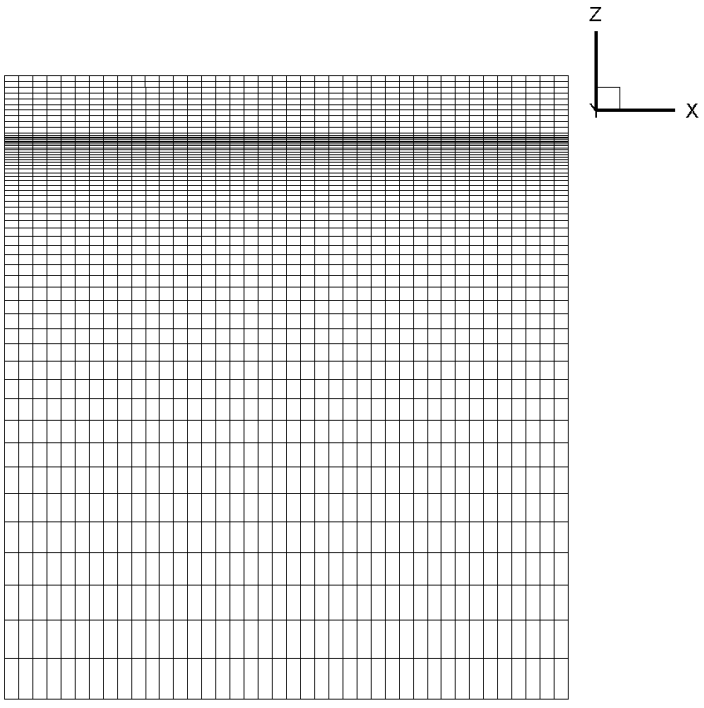

Figure IV-17 Mesh Bias

The bias can be calculated via a geometric sequence:

$$L = \frac{\Delta x_1 \left(1 - \alpha^N\right)}{1 - \alpha} \tag{2.34}$$

Where L is the length determined from the geometry, and N is the number of divisions.

$$\frac{\Delta x_N}{\Delta x_1} = \alpha^{N-1} \tag{2.35}$$

Δx_1 is to be some Δx as adjacent to a cell on the other side of the interface. Set N to desired number of cells. Then α is determined from equation (2.34), by solving iteratively. Once α is found, then $\frac{\Delta x_N}{\Delta x_1}$ is found from equation (2.35). The thickness of the cell at the wall was 2 mm with a bias factor of 36.26. Figure IV-18 shows the entire model with a mesh applied. A very fine mesh was applied at the interface of the steel and the air so that boundary layer flow could be accurately captured.

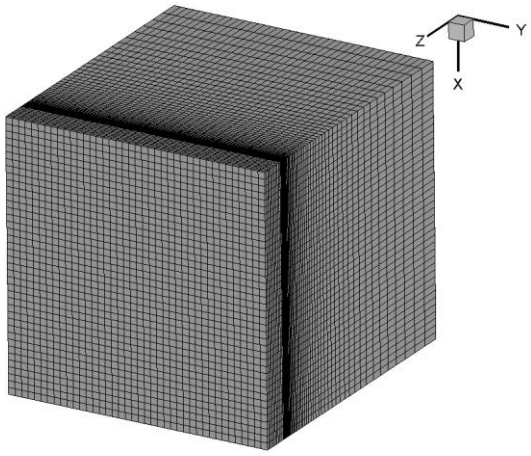

Figure IV-18 Meshing Example

V. Results and Discussion

A. Lumped Capacitance Model

The final temperatures after 15 minutes for each element are shown in the following table:

Table V-1 Temperatures of Elements after 15 minutes

Geometry/ Attachment	Fire Temperature (K)	Attachment Temperature (K)	Steel Temperature (K)	Insulation Temp (K)	Air Temperature (K)
Baseline	1011.71	N/A	304.82	509.95	297.27
6.25 cm^2	1011.71	800.11	304.95	510.00	297.47
25 cm^2	1011.71	800.12	305.24	514.79	298.02
100 cm^2	1011.71	800.17	305.02	510.01	299.47

As the surface area is increased for the attachment, there is a slight increase in the attachment and steel bulkhead temperatures and a slightly more significant rise in the air temperature.

The results for the Lumped Capacitance Model were plotted:

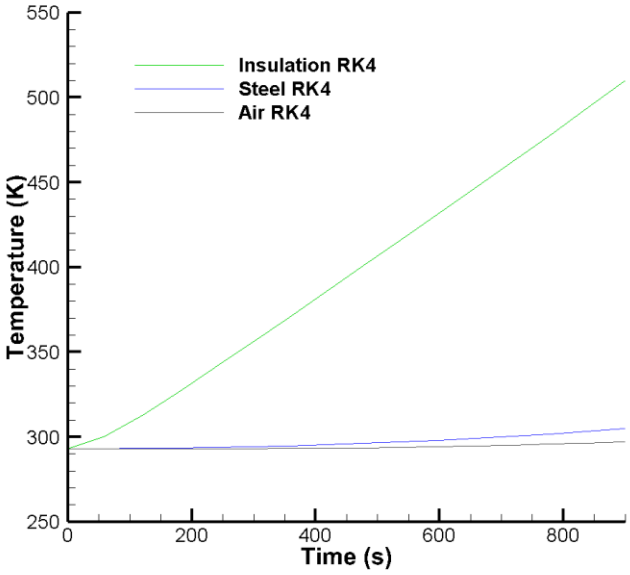

Figure V-1 Lumped Capacitance Results

The results for the different surface areas of the attachment are then plotted:

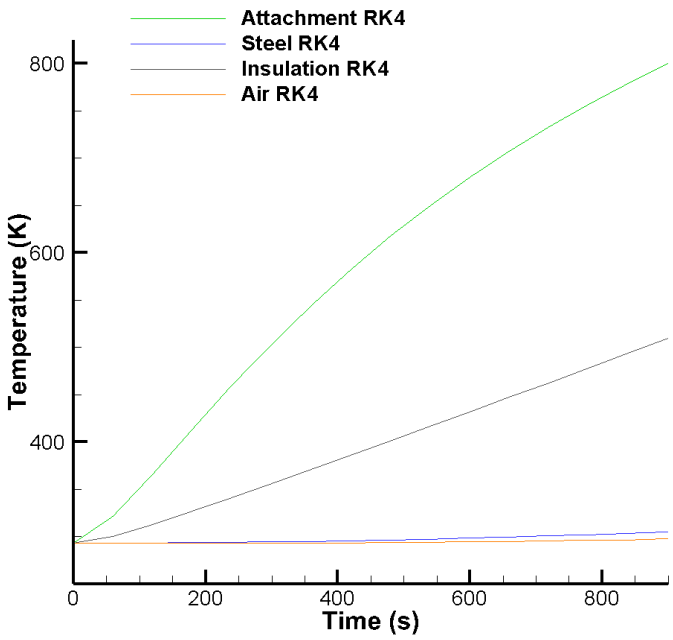

Figure V-2 Lumped Capacitance Parallel Flow, 6.25 cm^2 Attachment Results

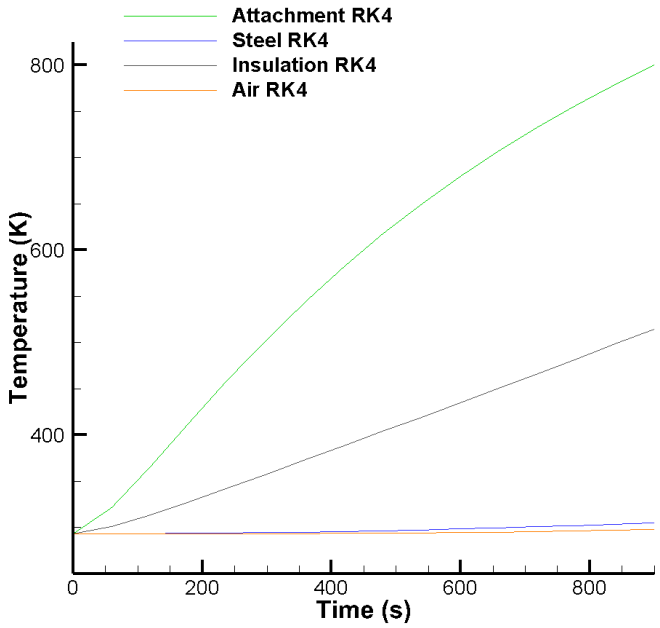

Figure V-3 Lumped Capacitance Parallel Flow, 25 cm^2 Attachment Results

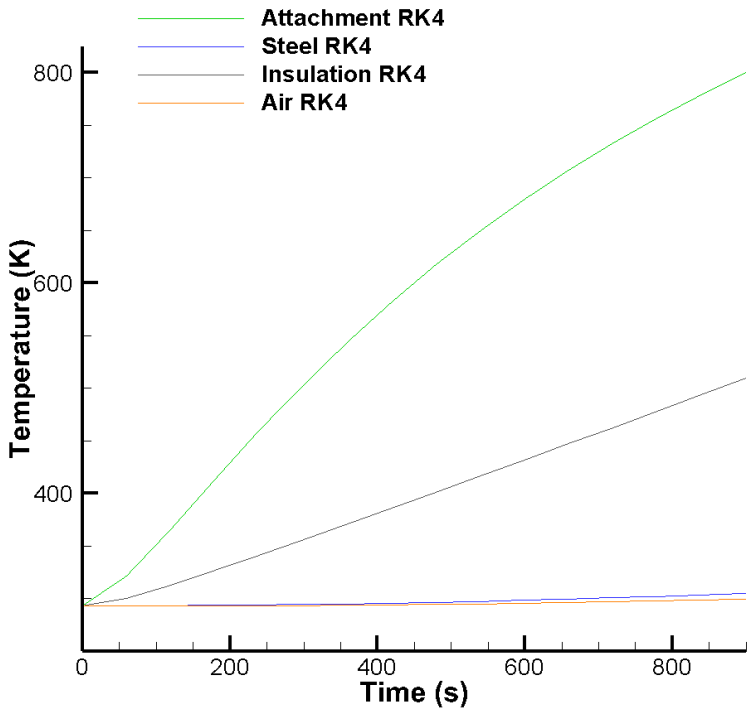

Figure V-4 Lumped Capacitance Parallel Flow, 100 cm^2 Attachment Results

The lumped capacitance model presents the average temperature for each element. Figure V-1 shows the results for the model without an attachment. From consulting Table V-1, it can be determined that, without an attachment, each element results in a lower average temperature. Figure V-2, Figure V-3, and Figure V-4 show the results for each attachment. It was found that when the surface area of the attachment was changed, there were only slight differences in the temperature for the elements. Although, it can be noted that as the surface area and volume of the attachment were increased, the temperature also increased for the elements, with the exception of the 100 cm^2 attachment. This could be due to the fact that the insulation has a lower thermal conductivity and, at a greater volume, could absorb more of the heat being applied to the model. For the 100 cm^2, the increase in volume for the steel attachment could have caused it to act as a heat sink and therefore have a greater increase in temperature than the smaller attachments.

B. CFD Model Baseline

1. Baseline Constant Thermal Conductivity

In order to analyze whether or not an attachment through the insulation would exceed the given boundaries set by the regulations, a baseline was first established. The baseline consisted of a model without any attachments and constant thermal conductivity for all materials. The simulation time was fifteen minutes. The density of the air was computed using the Boussinesq approximation with an initial temperature of 293.15 K.

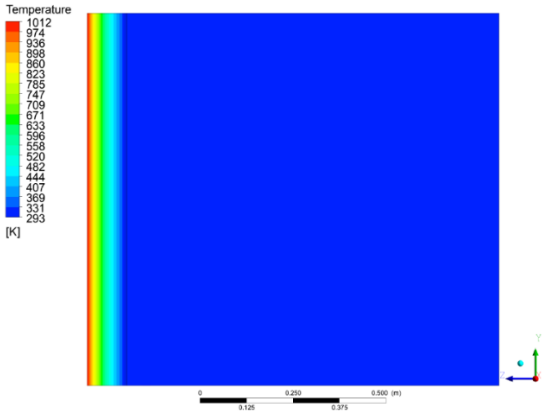

Figure V-5 Baseline Model Side View Temperature Contour, Constant Thermal Conductivity

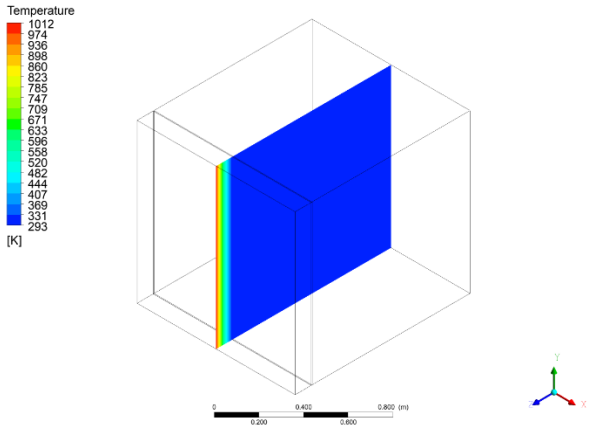

Figure V-6 Baseline Model Isometric View Temperature Contour, Constant Thermal Conductivity

Figure V-5 and Figure V-6 show the temperature distribution after 15 minutes throughout a center line slice of the model. The temperature is highest at the surface of the insulation. The insulation and steel resist the heat transfer and the temperature ultimately decreases to 293.15 K.

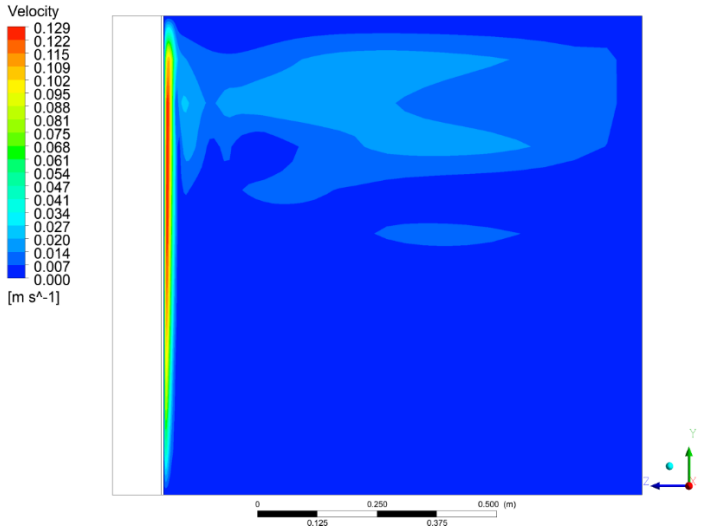

Figure V-7 Baseline Model Side View Velocity Contour, Constant Thermal Conductivity

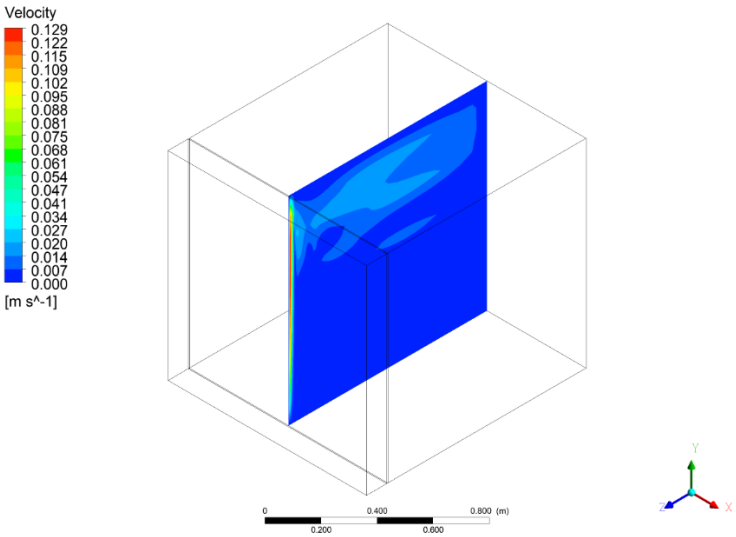

Figure V-8 Baseline Model Isometric View Velocity Contour, Constant Thermal Conductivity

Figure V-7 and Figure V-8 show that a viscous boundary layer formed on the steel wall. This is due to the gravity present in the fluid section and the presence of buoyancy-driven convection currents. The difference in density due to temperature changes and the presence of gravity causes the convection currents.

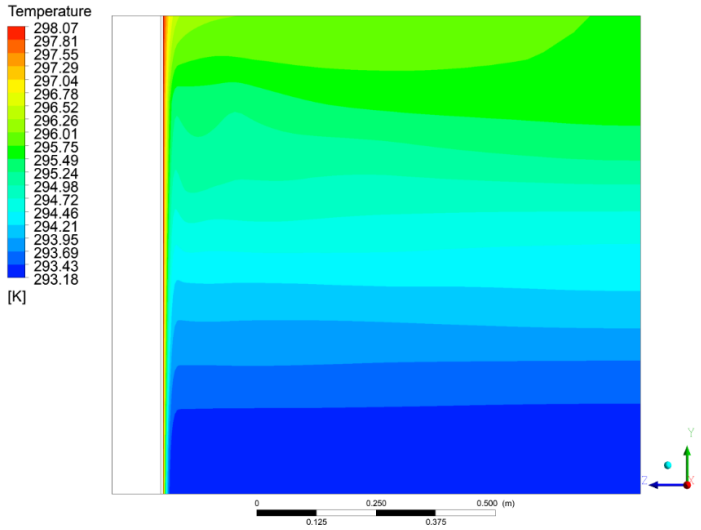

Figure V-9 Baseline Model Side View Temperature Contour Air, Constant Thermal Conductivity

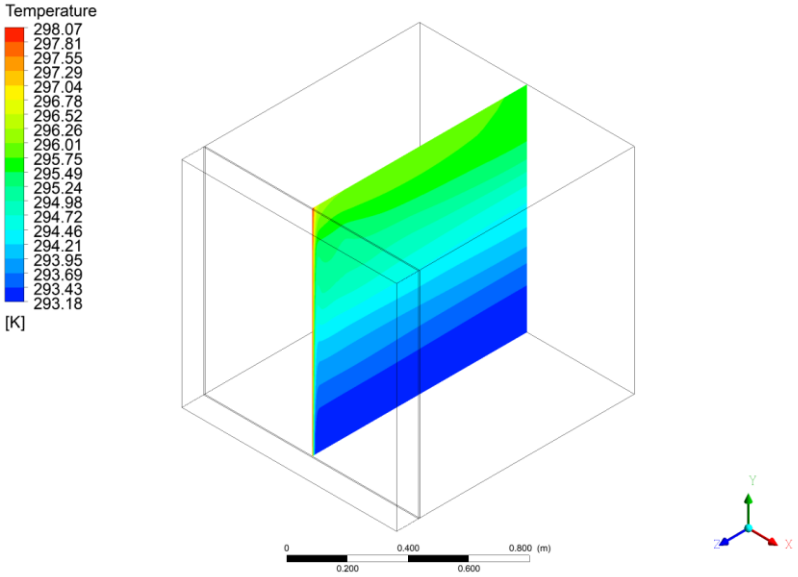

Figure V-10 Baseline Model Isometric View Temperature Contour Air, Constant Thermal Conductivity

During the 15-minute simulation, the steel wall that was exposed to the air increased in temperature. This caused a thermal boundary layer to develop at the wall. The temperature increase caused a density difference in the air leading to natural convection. As seen in Figure V-9 and Figure V-10, the air at a higher temperature rose, while the cooler air sank to the bottom of the model.

Once these results were complete, the CFD model was compared with the Lumped Capacitance Model and the results were graphed against each other in Figure V-11. The temperature was averaged with a CFD model for each domain so that both methods could be compared. This volume averaging is computed by:

$$T_{av}(t) = \frac{1}{V}\int_V T(x,y,z,t)dV \tag{1.1}$$

Where V is the volume of each domain, and the volumetric average in each domain is a function of time.

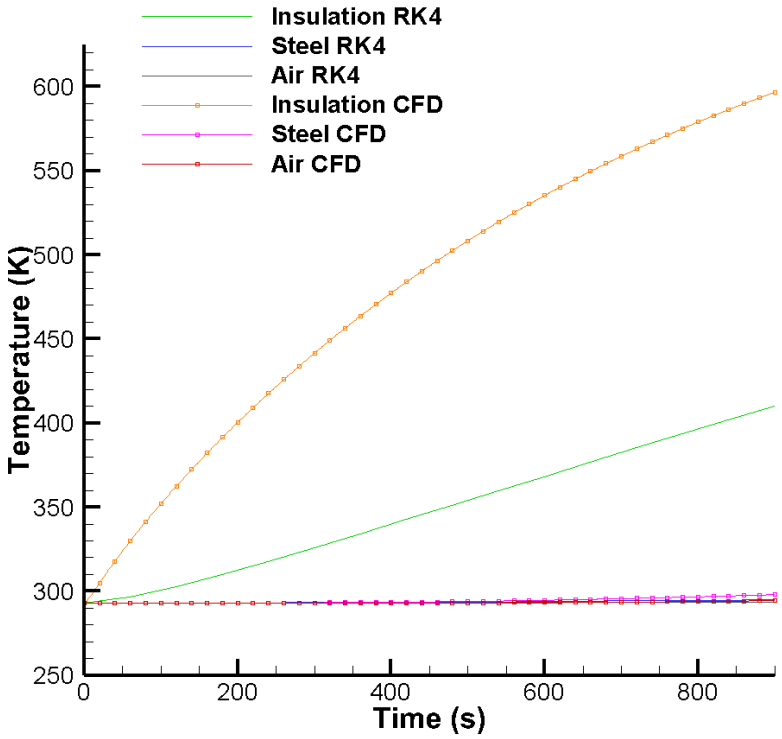

Figure V-11 CFD vs Lumped Capacitance Results, Constant Thermal Conductivity

These results point to discrepancies between the CFD and Lumped Capacitance results for the temperature of the insulation over time. It appears as though the Lumped Capacitance Model significantly underpredicted the temperature average of the insulation. The predictions for both the steel and air were much closer. The percent difference between the lumped capacitance model and the CFD model for insulation was 38.87%, 4.57% for the steel, and 1.99% for the air. This discrepancy could be due to the large increase in temperature at the surface of the insulation and the insulation's low thermal conductivity.

2. Baseline Temperature Dependent Thermal Conductivity

In order to create a more accurate model, the thermal conductivity of the insulation and steel was made temperature dependent. This temperature dependency was illustrated in Figure IV-5 and Figure IV-6. The insulation's ability to resist the heat build-up over time was diminished, while the steel's ability was strengthened. The CFD and Lumped Capacitance runs were held for a 15-minute time domain to test for A-15 compliance.

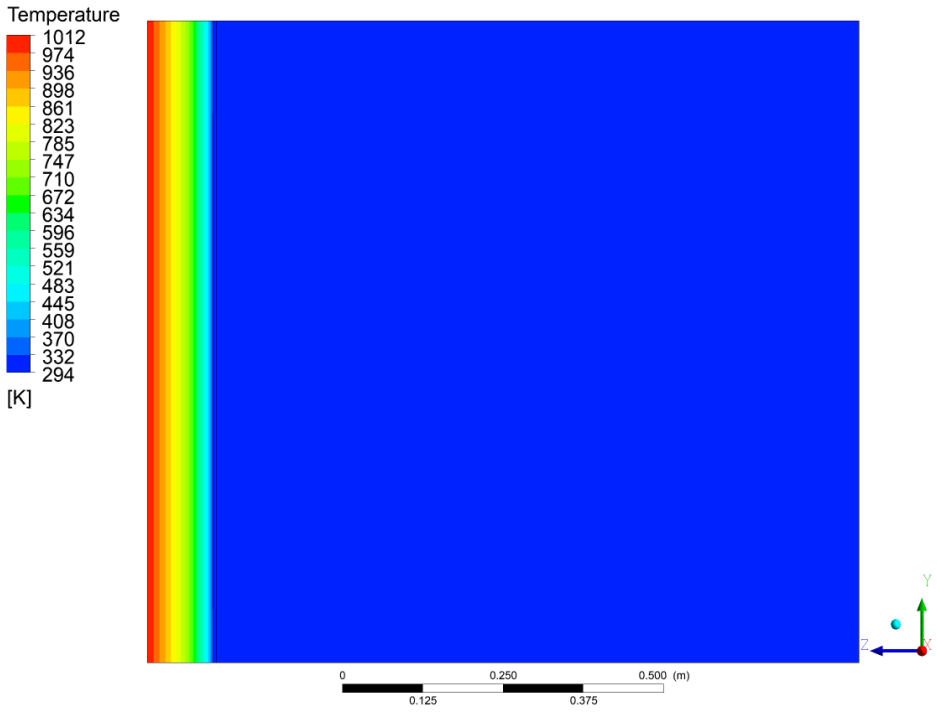

Figure V-12 Baseline Model Side View Temperature Contour

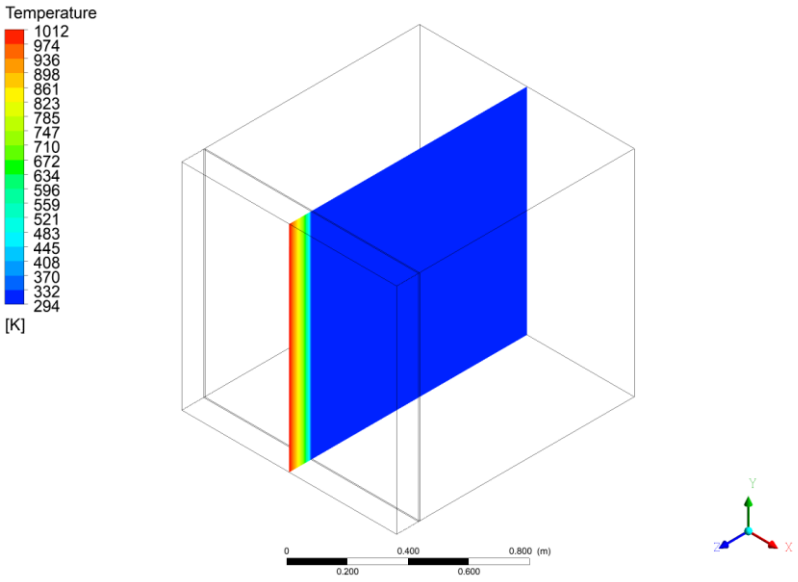

Figure V-13 Baseline Model Isometric View Temperature Contour

Since the thermal conductivity was made temperature dependent, the insulation became less resistant to the increase in temperature and the steel became more resistant. This result can be seen by comparing Figure V-5 and Figure V-6 to Figure V-12 and Figure V-13. Since the insulation's thermal conductivity increased, both the steel and air experienced an increase in temperature.

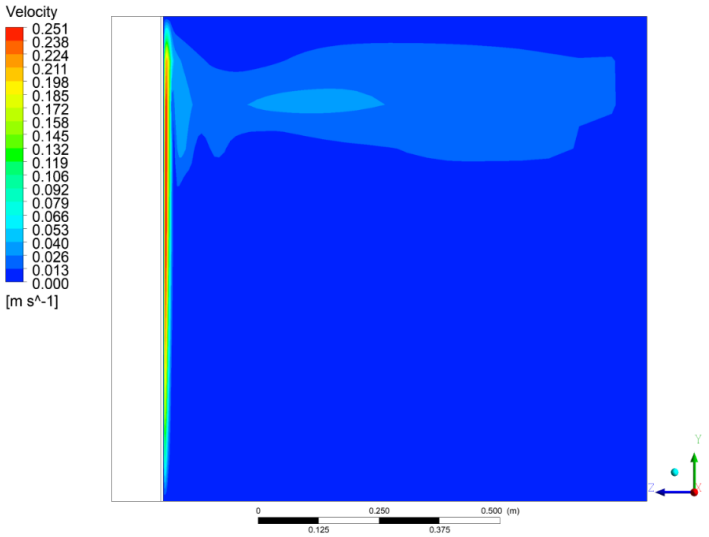

Figure V-14 Baseline Model Side View Velocity Contour

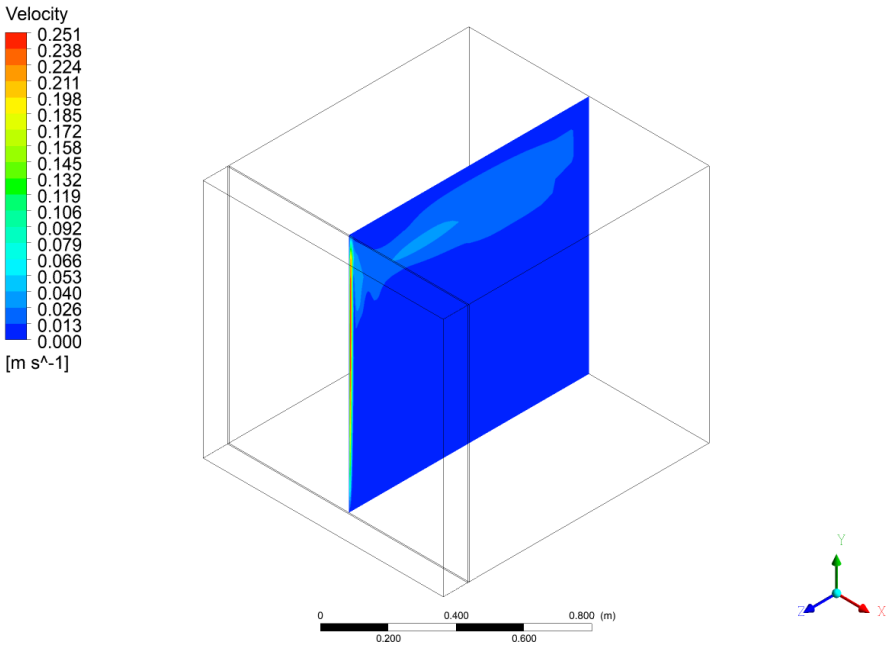

Figure V-15 Baseline Model Isometric View Velocity Contour

For this model, the steel experienced a higher increase in temperature. This increase in temperature caused the velocity of the fluid at the viscous boundary layer shown in Figure V-14 and Figure V-15 to nearly double compared to the constant thermal conductivity model.

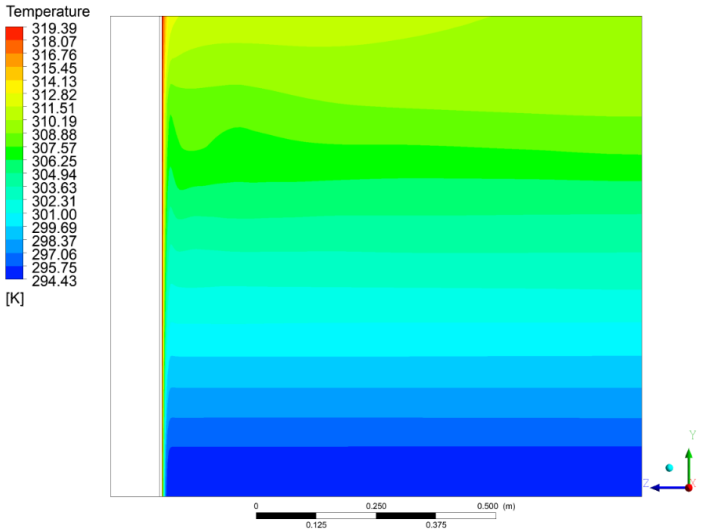

Figure V-16 Baseline Model Side View Temperature Contour Air

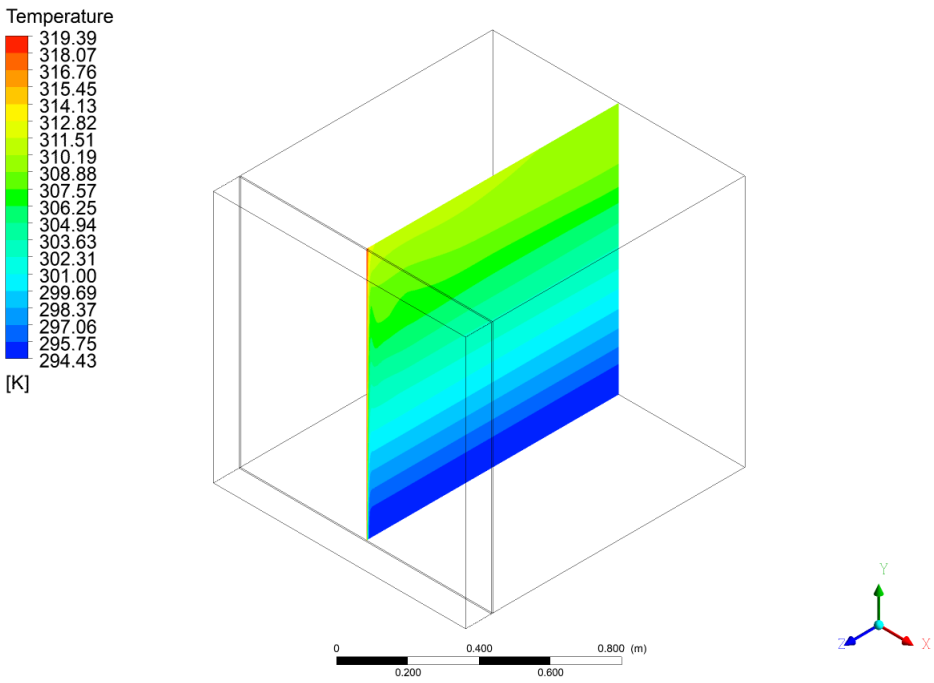

Figure V-17 Baseline Model Isometric View Temperature Contour Air

The temperature of the air for the temperature dependent thermal conductivity model, as shown in Figure V-16 and Figure V-17, experienced a 20 K rise compared to the constant thermal conductivity model. It can be concluded that making a material's thermal conductivity temperature dependent is necessary to ensure accuracy of the model.

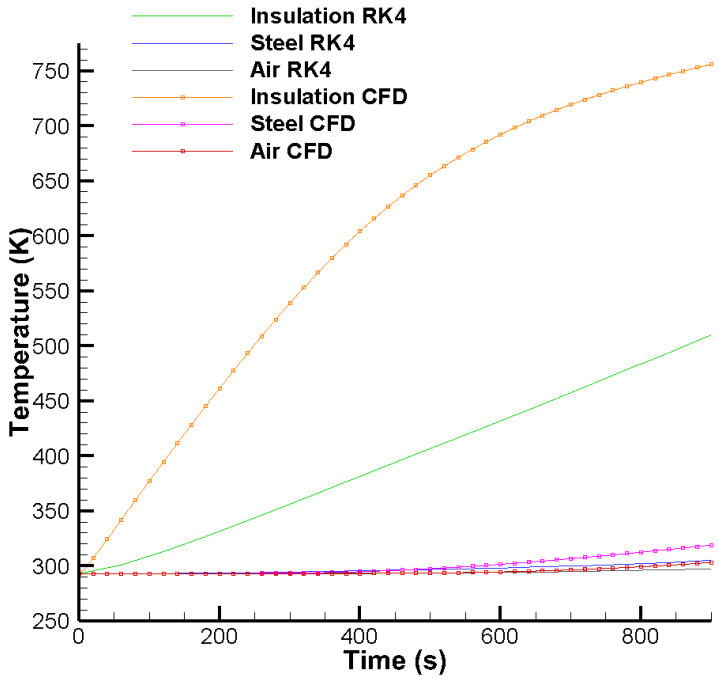

Figure V-18 Baseline CFD vs Lumped Capacitance Results

Figure V-18 compares the results of the lumped capacitance model to the CFD model. Once again, the temperature average of the insulation was significantly less, and the temperature averages of the steel and air were found to be slightly less than the CFD model. The purpose of this model was to establish a baseline and create a model that conforms to the regulations. This is necessary because the baseline model must conform to the regulations to accurately depict a model with an attachment. "Such that the average temperature of the unexposed side will not rise more than 140° C above the original temperature, nor will the temperature, at any one point, including any joint, rise more than 180° C above the original temperature" (SOLAS Consolidated Edition, 2014, p. 125). The initial temperature of the model was set to 293.15 K or 20° C. The average temperature of the air rose to 303.24 K or 30.09° C, making it a 10.09° C rise in temperature. This temperature rise was well below the required 140° C. Also, a point temperature was taken at the top of the steel bulkhead and was found to be 319.44 K or 46.29° C.

This is a 26.29ºC rise in temperature, which is much less than the allowed 180º C rise. Therefore, this baseline model is appropriate for this study.

3. Mesh Independence Study

Following this, a mesh and timestep independence study was carried out where the mesh was varied from a fine mesh to a coarse mesh, and the timesteps were varied. Table *V-2* shows how the timestep and mesh were varied for each CFD run.

Table V-2 Mesh Independence Study

Run	Timestep (s)	Mesh
1	0.5	Original
2	0.5	Coarse 0.5 x
3	0.5	Fine 2 x
4	0.25	Original
5	1	Original

The following average integrals for temperature were taken at 15 minutes for each of the runs in the mesh/time-step independence study:

Table V-3 Mesh Independence Study Temperature Averages

Run	Insulation Temperature (K)	Steel Temperature (K)	Air Temperature (K)
1	756.00	319.09	303.24
2	755.89	319.03	303.58
3	756.03	319.11	303.11
4	756.01	319.08	303.24
5	756.00	319.11	303.26

Table *V-3* shows that there was little variance in the average temperature of each element.

The results for Run 2, the coarse mesh, are as follows:

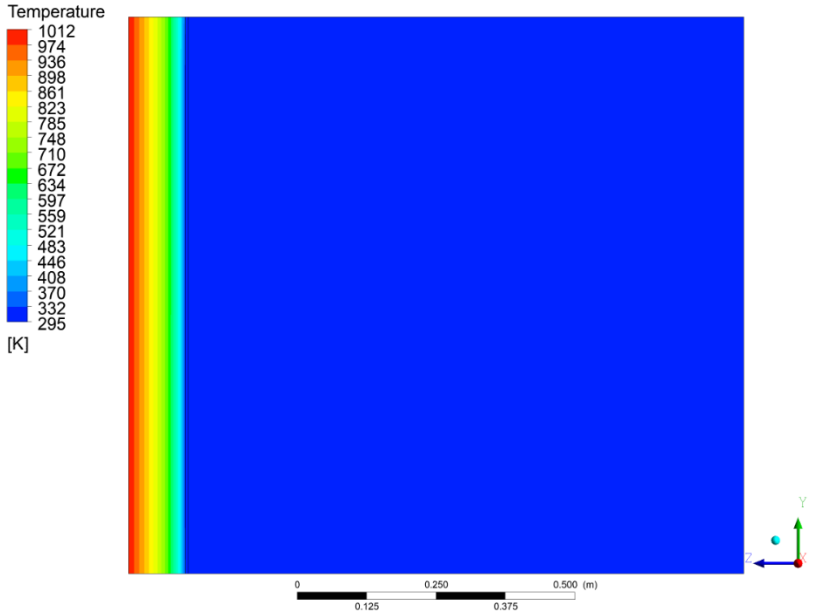

Figure V-19 Baseline Coarse Mesh Side View Temperature Contour

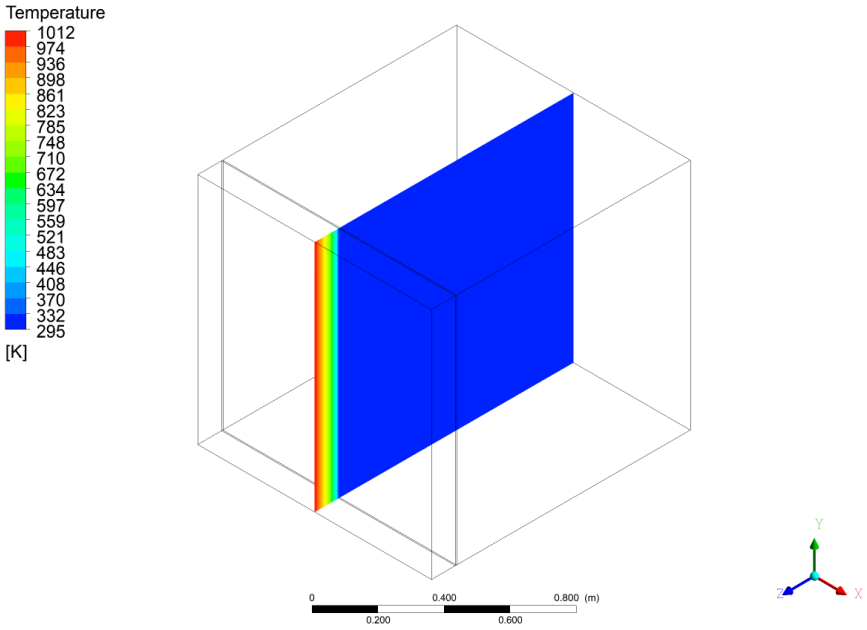

Figure V-20 Baseline Coarse Mesh Isometric View Temperature Contour

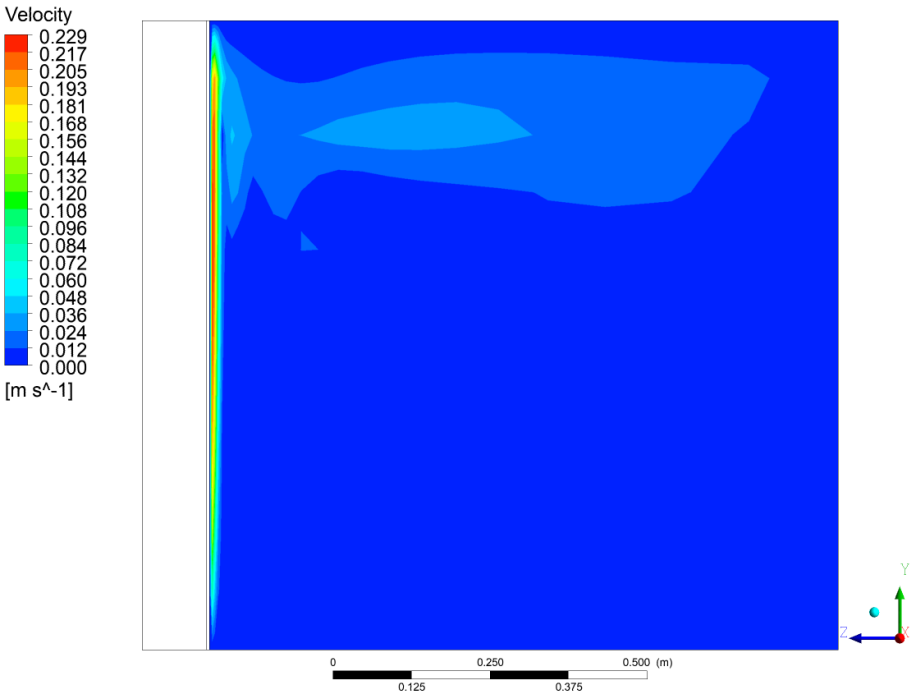

Figure V-21 Baseline Coarse Mesh Side View Velocity Contour

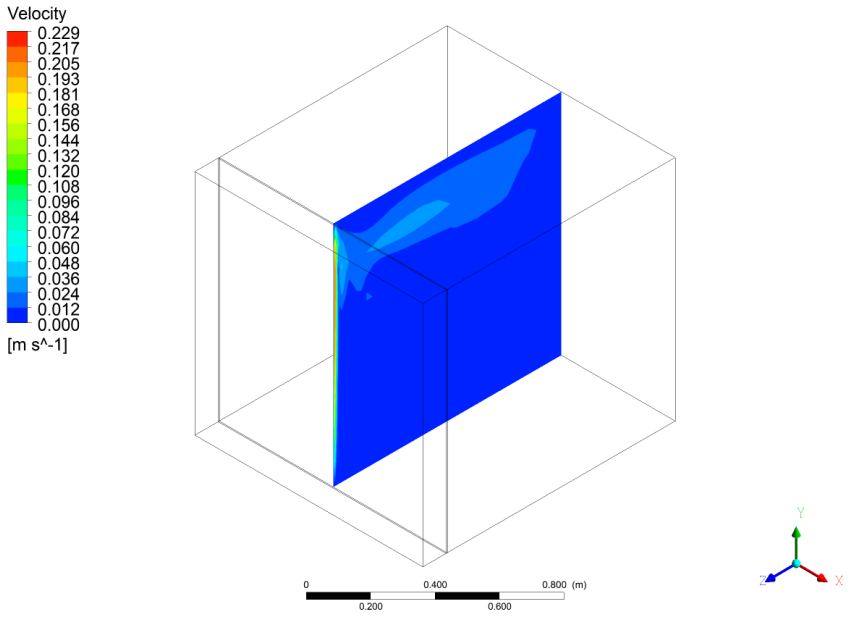

Figure V-22 Baseline Coarse Mesh Isometric View Velocity Contour

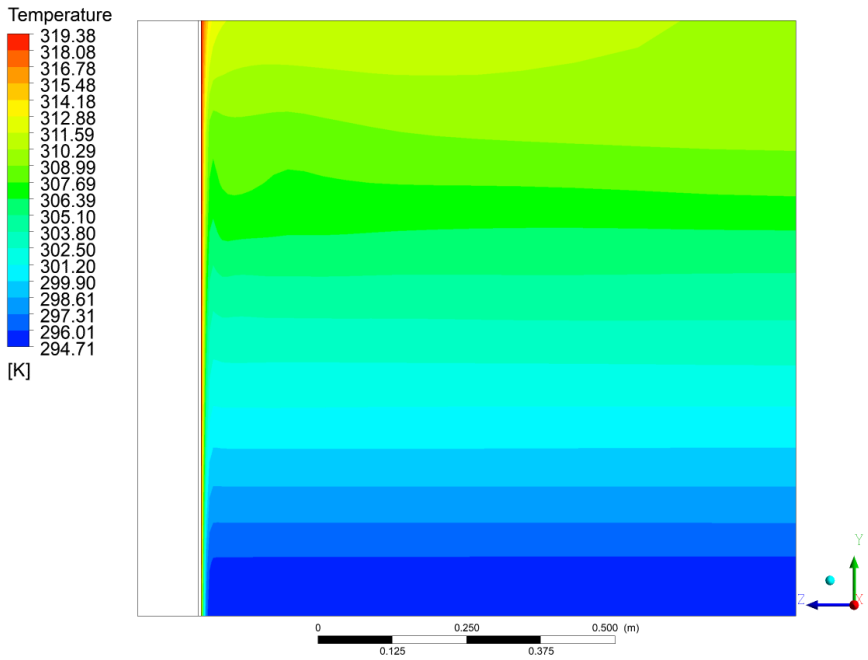

Figure V-23 Baseline Coarse Mesh Side View Temperature Contour Air

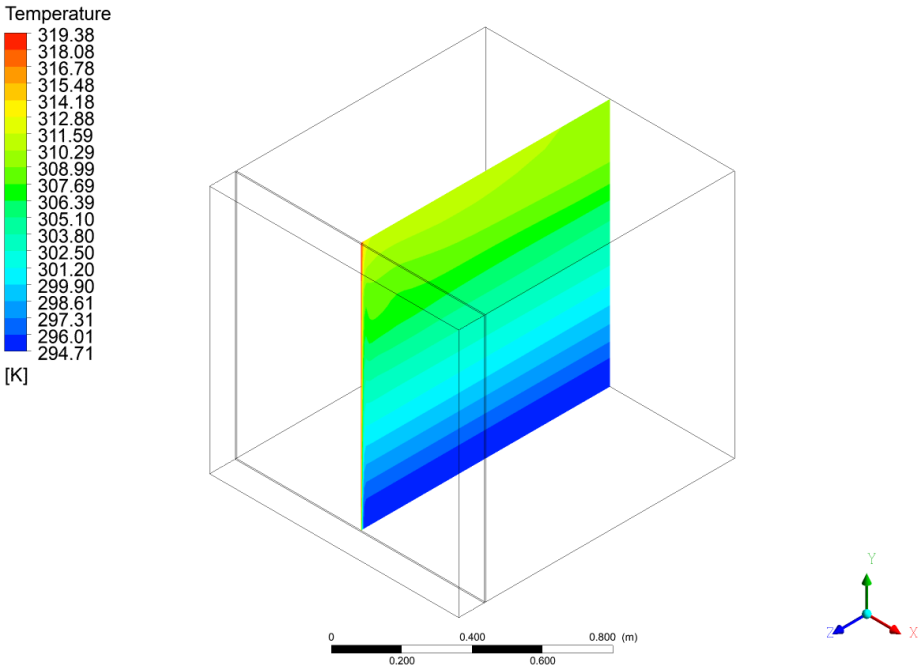

Figure V-24 Baseline Coarse Mesh Isometric View Temperature Contour Air

The results for Run 3, the fine mesh, are as follows:

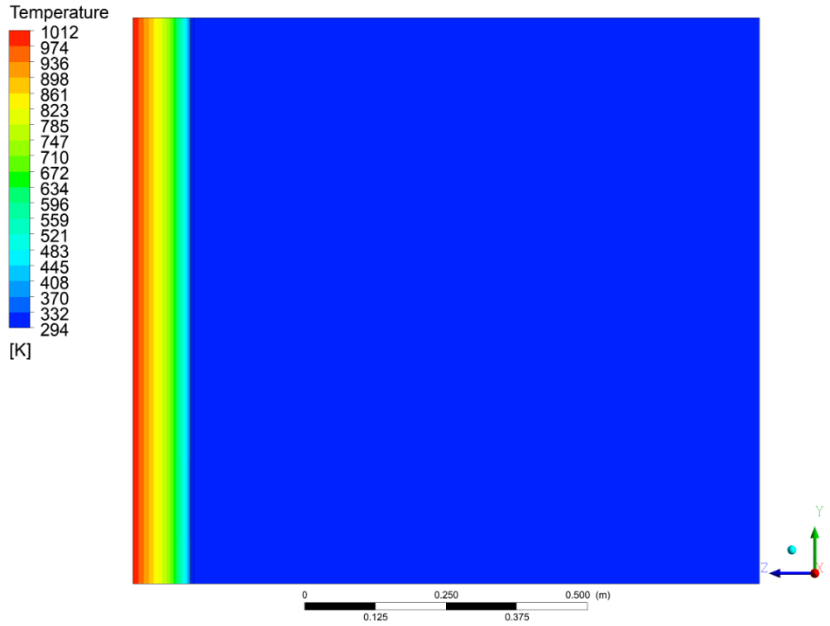

Figure V-25 Baseline Fine Mesh Side View Temperature Contour

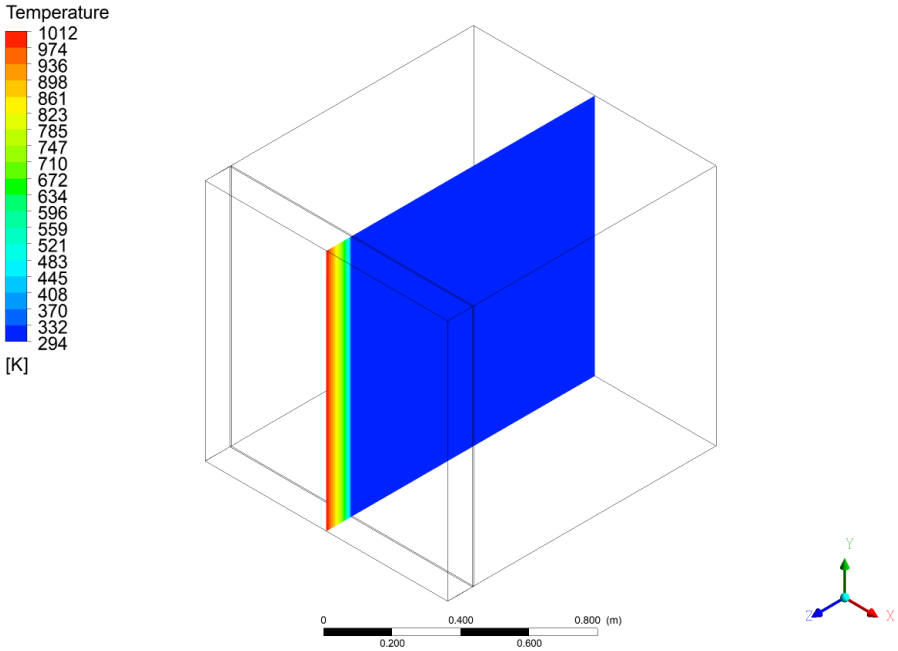

Figure V-26 Baseline Fine Mesh Isometric View Temperature Contour

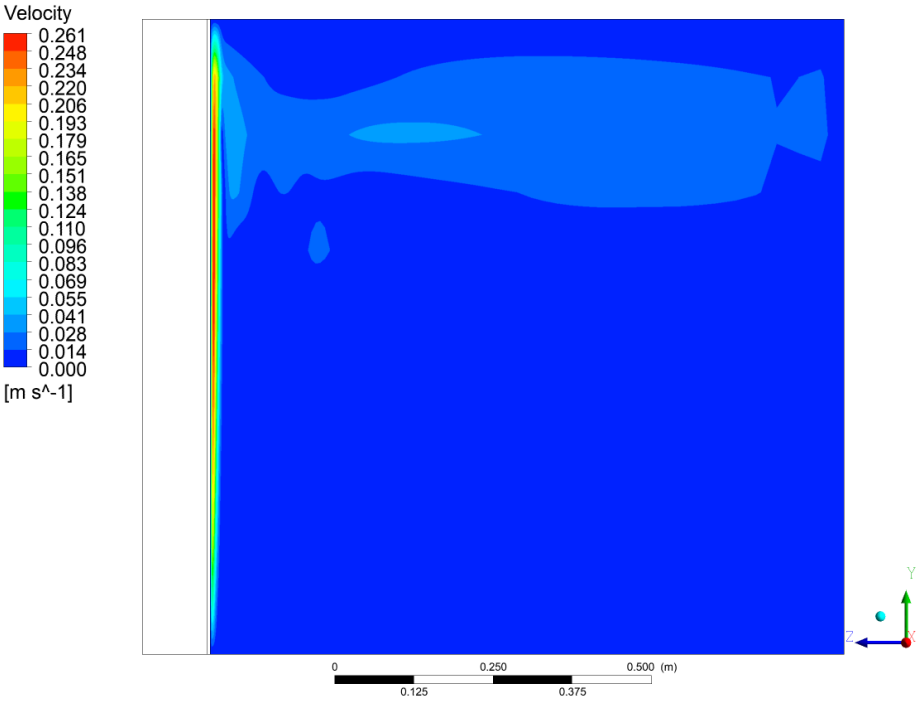

Figure V-27 Baseline Fine Mesh Side View Velocity Contour

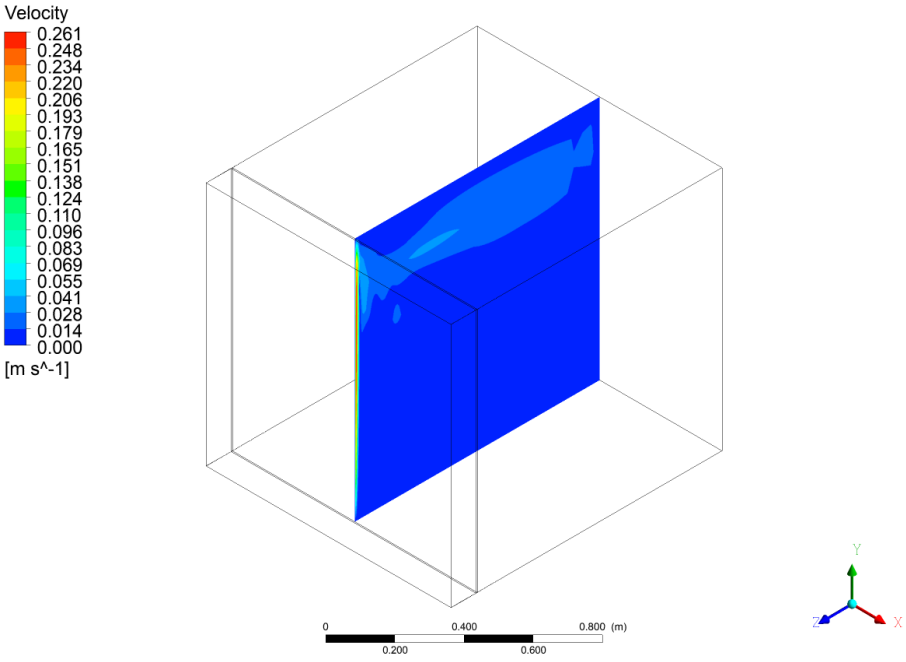

Figure V-28 Baseline Fine Mesh Isometric View Velocity Vector

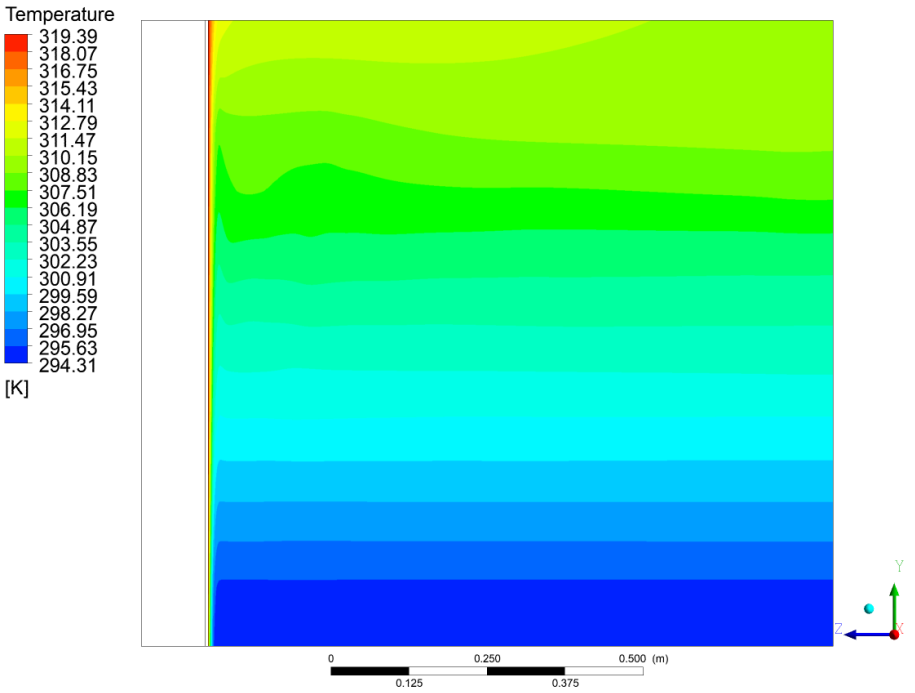

Figure V-29 Baseline Fine Mesh Side View Temperature Contour Air

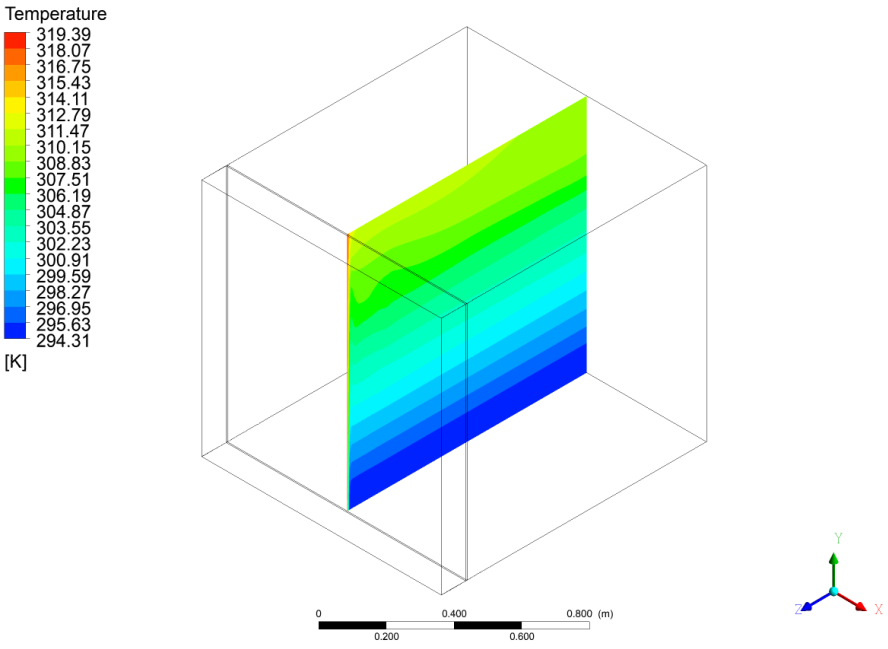

Figure V-30 Baseline Fine Mesh Isometric View Temperature Contour Air

The results for Run 4, the 0.25 second timestep, are as follows:

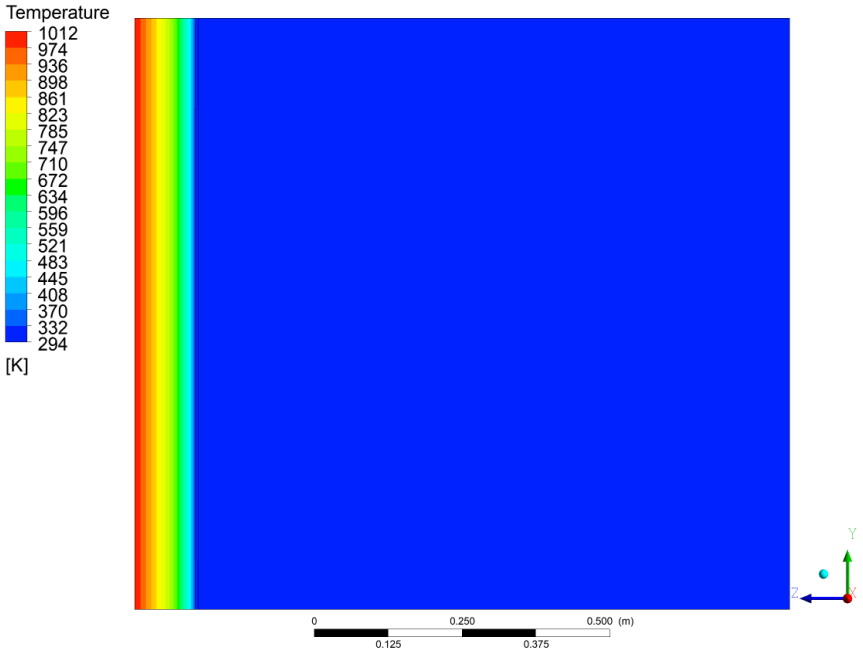

Figure V-31 Baseline 0.25 Second Time-step Side View Temperature Contour

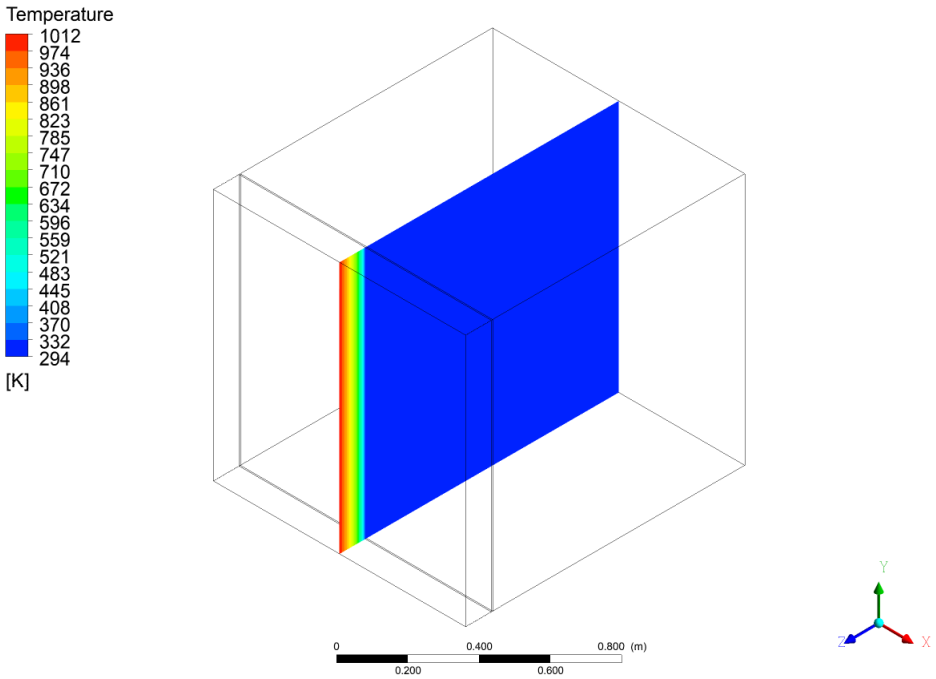

Figure V-32 Baseline 0.25 Second Time-step Isometric View Temperature Contour

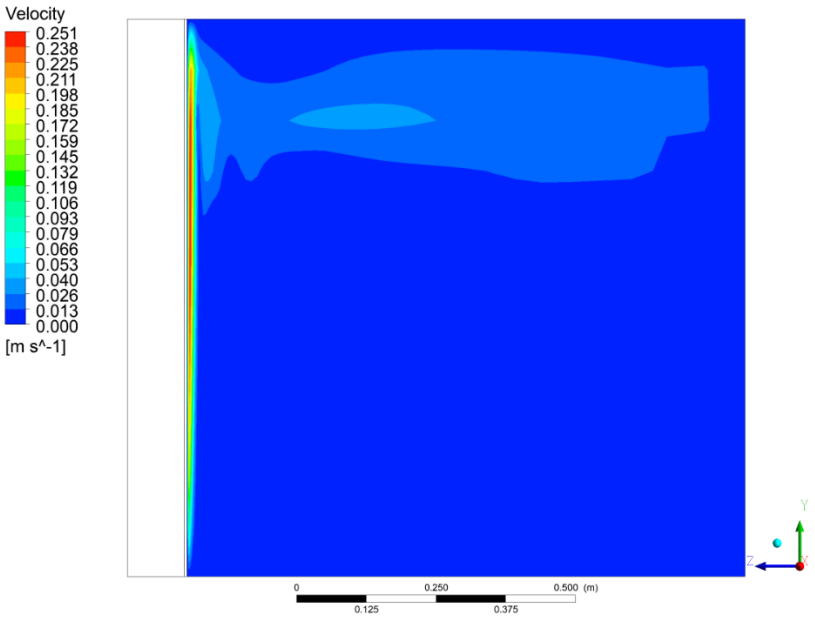

Figure V-33 Baseline 0.25 Second Time-step Side View Velocity Contour

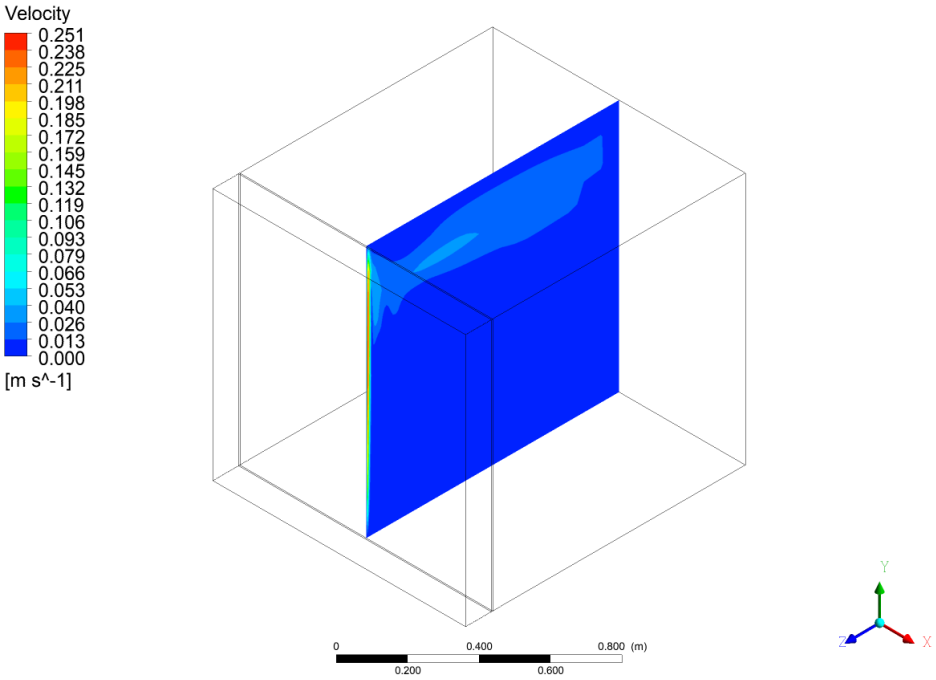

Figure V-34 Baseline 0.25 Second Time-step Isometric View Velocity Contour

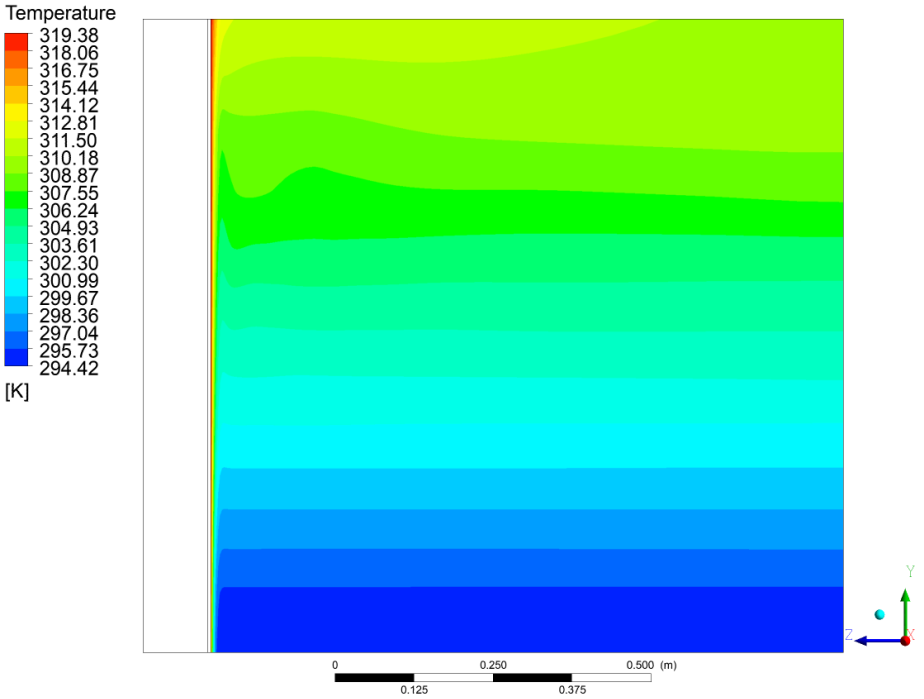

Figure V-35 Baseline 0.25 Second Time-step Side View Temperature Contour Air

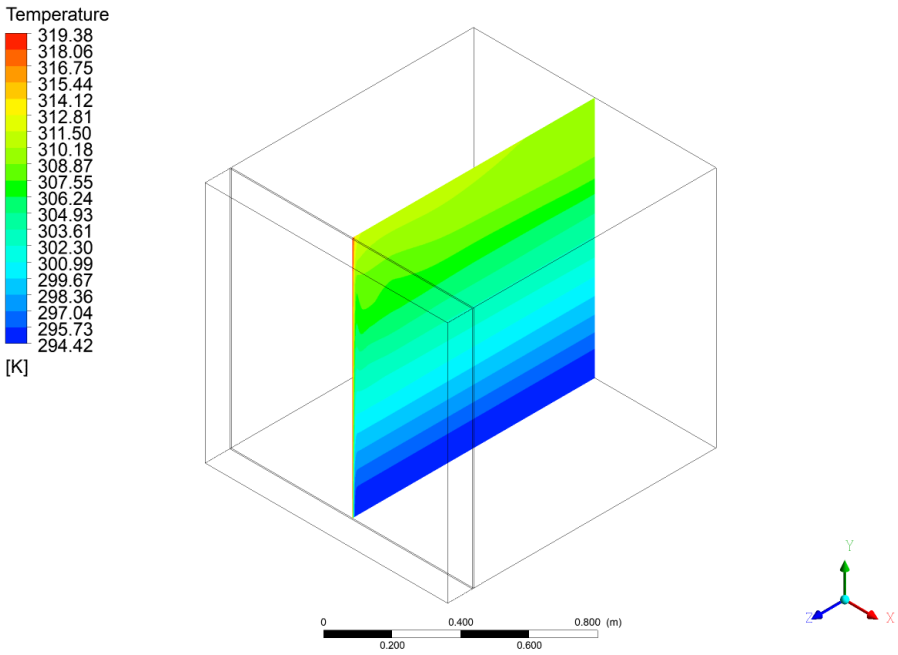

Figure V-36 Baseline 0.25 Second Time-step Isometric View Temperature Contour Air

The results for Run 5, the 1-second timestep, are as follows:

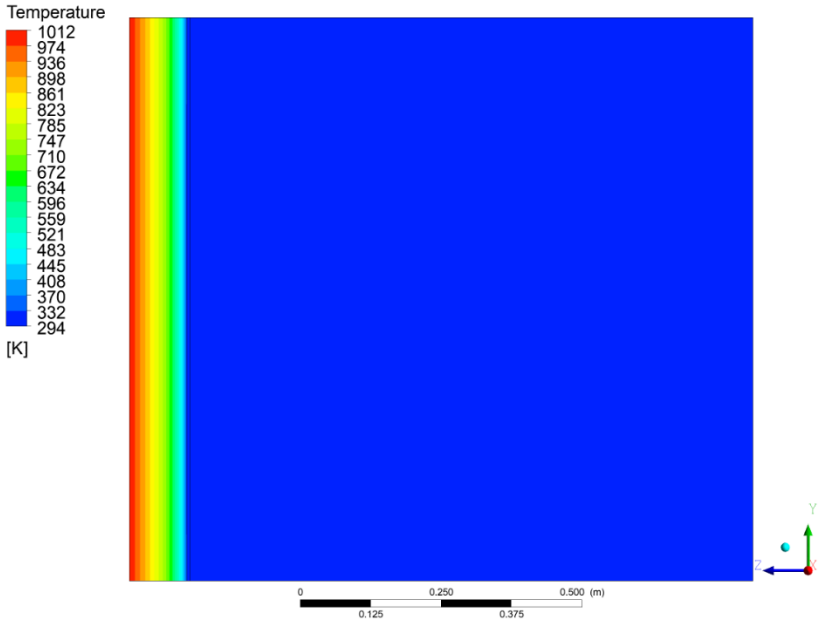

Figure V-37 Baseline 1 Second Time-step Side View Temperature Contour

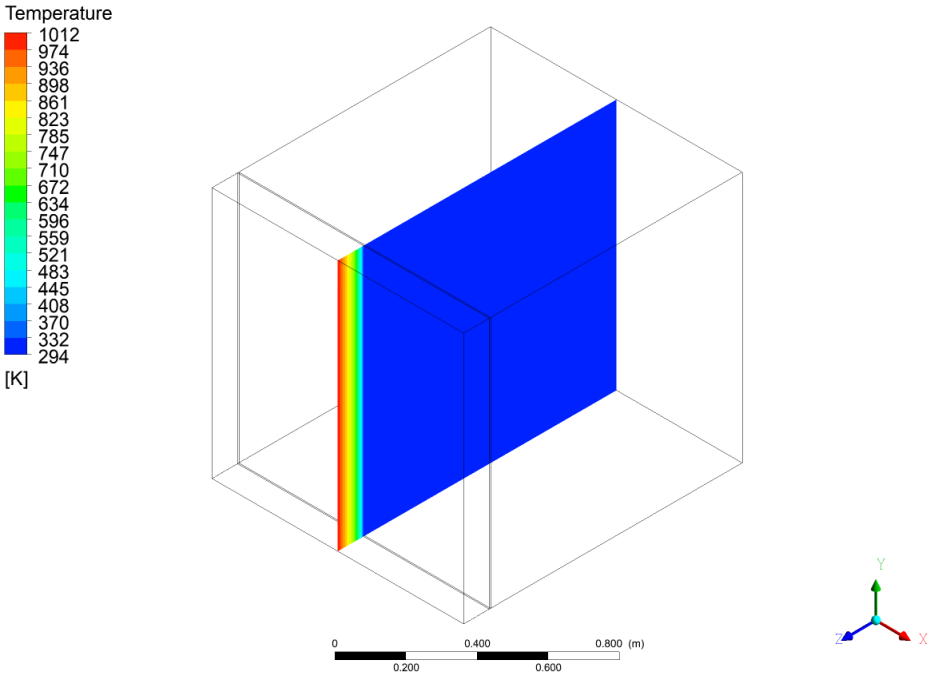

Figure V-38 Baseline 1 Second Time-step Isometric View Temperature Contour

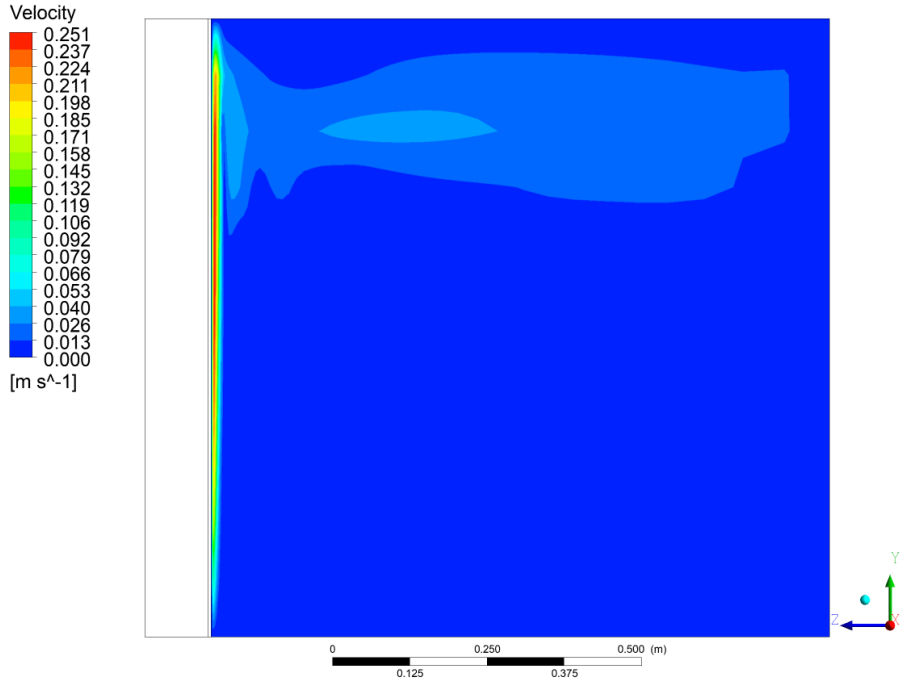

Figure V-39 Baseline 1 Second Time-step Side View Velocity Contour

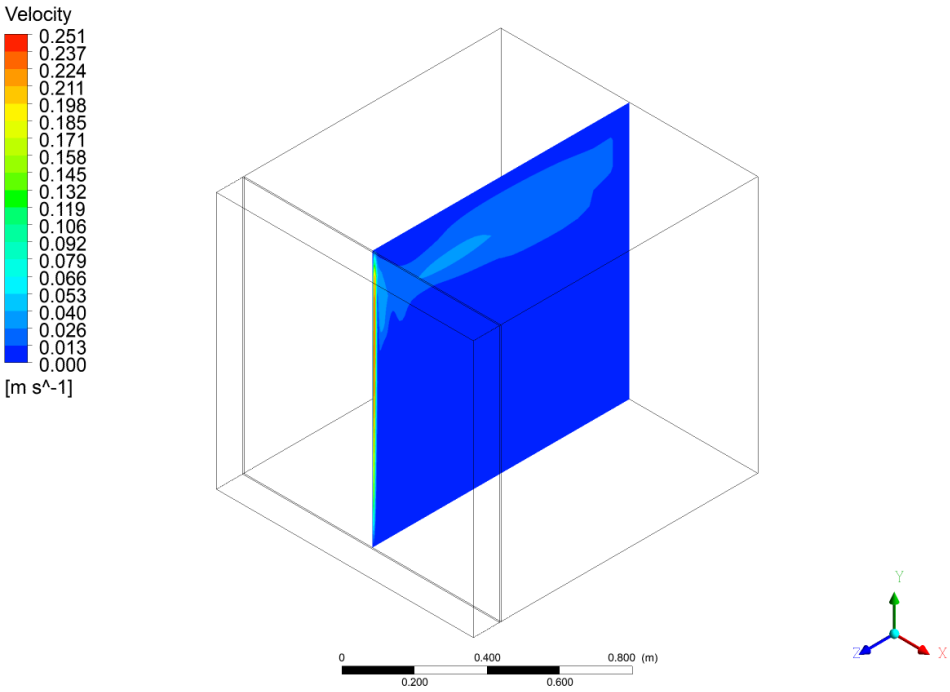

Figure V-40 Baseline 1 Second Time-step Isometric View Velocity Contour

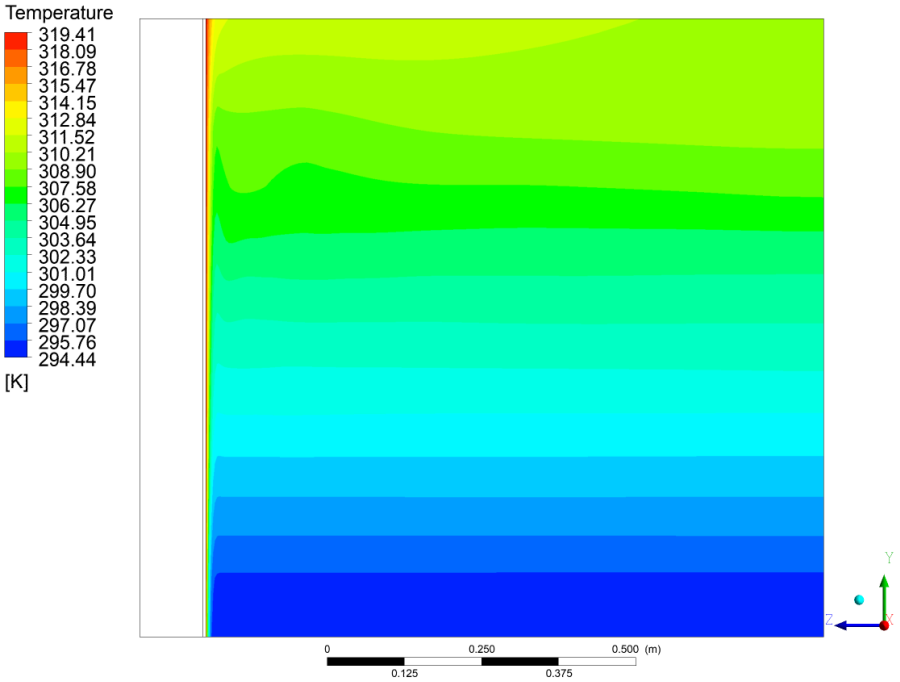

Figure V-41 Baseline 1 Second Time-step Side View Temperature Contour Air

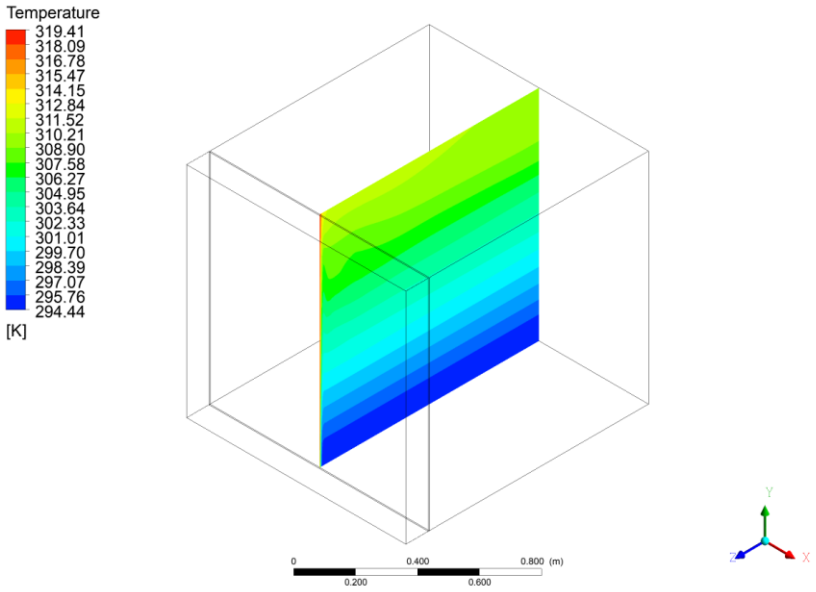

Figure V-42 Baseline 1 Second Time-step Isometric View Temperature Contour Air

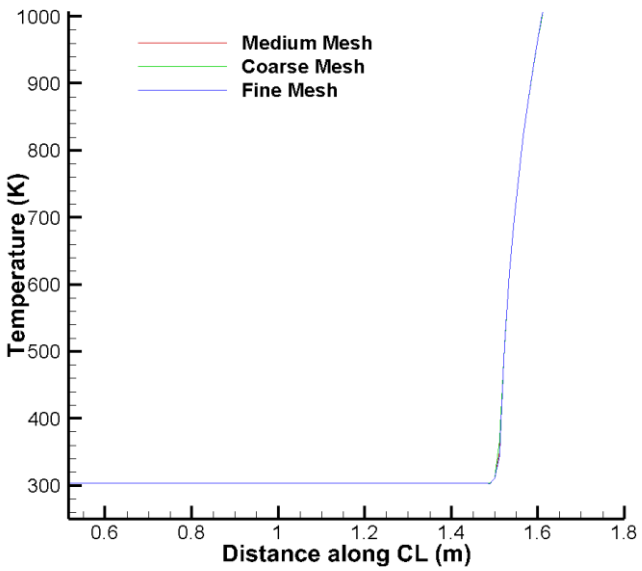

Figure V-43 Comparison of Temperature along CL for Different Meshes

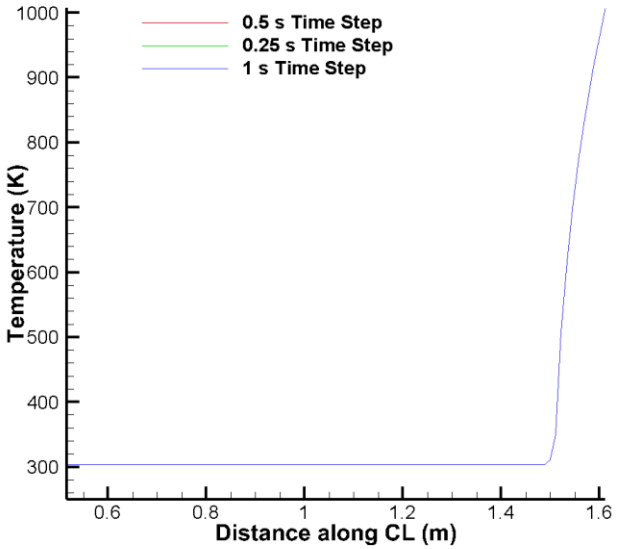

Figure V-44 Comparison of Temperature along CL for Different Time Steps

The mesh/time-step independence study proved that the model was independent of both. The temperature contours at the centerline, including all materials, for Figure *V-19*, Figure *V-20*, Figure *V-25*,

Figure *V-26*, Figure *V-31*, Figure *V-32*, Figure *V-37*, and Figure *V-38* showed little variance when compared to Figure *V-12* and Figure *V-13* of the baseline model. The velocity contours at the centerline for Figure *V-21*, Figure *V-22*, Figure *V-27*, Figure *V-28*, Figure *V-33*, Figure *V-34*, Figure *V-39*, and Figure *V-40* when compared to Figure *V-14* and Figure *V-15* had a maximum variance of 0.022 m/s. The temperature contours for just the air element at centerline for Figure *V-23*, Figure *V-24*, Figure *V-29*, Figure *V-30*, Figure *V-35*, Figure *V-36*, Figure *V-41*, and Figure *V-42* when compared to Figure *V-16* and Figure *V-17* showed a negligible variance. The average integrals of the insulation, steel, and air were very close in value when compared for each run. For Figure V-43 and Figure V-44, the temperature along the center line at the 900-second timestep were compared. Each of the temperature vs. distance center lines matched well for both the mesh and timestep independence studies. Also, the maximum and minimum values for temperature and velocity for each of the figures were similar as well. The largest difference found was between Figure V-22 and Figure V-27. Although, this difference could be expected. Figure V-22 shows that the coarser mesh will have more difficulty representing the boundary layer flow at the wall. Figure V-27 demonstrates that the finer mesh represents the viscous boundary layer more accurately because of the more available cells at the wall.

C. CFD Model with Attachment

In order to determine if an attachment has an effect on the constraints for the adjacent room, three different attachments of differing surface areas were modeled. These are also compared to the Lumped Capacitance Parallel Flow Model that was created. The average temperature integral of each element was taken from the CFD model and contrasted with the Parallel Flow model in Table V-4. It can be noted that as the size of the attachment increased the accuracy of the lumped capacitance method for that element increased.

Table V-4 Comparison of Lumped Capacitance Parallel Flow and CFD Results

	Attachment Temperature (K)	Insulation Temperature (K)	Steel Temperature (K)	Air Temperature (K)
Lumped Capacitance 6.25 cm^2 Attachment	800.11	510.00	304.95	297.47
CFD 6.25 cm^2 Attachment	731.78	755.53	321.46	304.81
Lumped Capacitance 25 cm^2 Attachment	800.12	514.79	305.24	298.02
CFD 25 cm^2 Attachment	778.99	756.32	325.67	307.39
Lumped Capacitance 100 cm^2 Attachment	800.17	510.01	305.02	299.47
CFD 100 cm^2 Attachment	815.66	757.87	335.20	313.44

The results for all three surface areas were analyzed, and varying contours are shown to analyze the results. The first surface area to be presented is an attachment with a 2.5 cm^2 surface area.

1. 6.25 cm^2 Attachment

Figure V-45 and Figure V-46 show that the attachment allows heat to travel through it more readily than the insulation. This will cause a higher temperature build-up where the attachment meets the steel bulkhead.

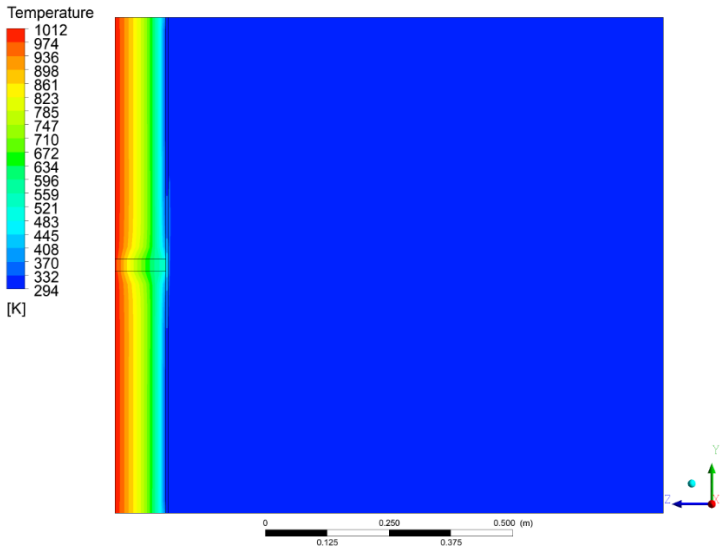

Figure V-45 6.25 cm^2 Attachment Side View Temperature Contour

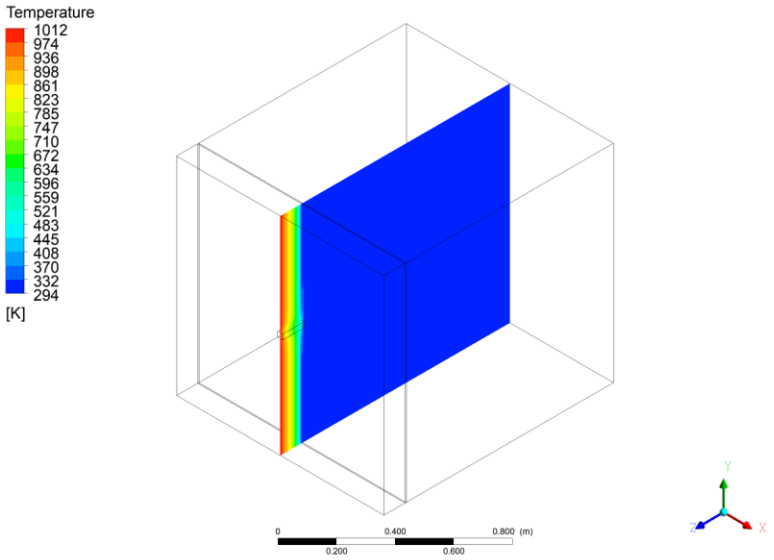

Figure V-46 6.25 cm^2 Attachment Isometric View Temperature Contour

Figure V-47 and Figure V-48 show the viscous boundary layer that developed at the steel bulkhead. From looking at the velocity contours, it can be seen that the flow's velocity is much greater after the attachment. The maximum velocity for the model with the attachment is also much greater than the model without the attachment, see Figure V-14. This could be due to the higher temperature at the intersection of the attachment and the steel bulkhead.

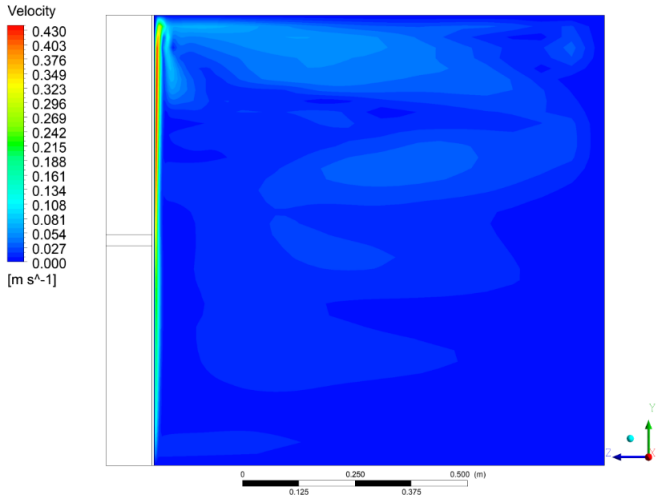

Figure V-47 6.25 cm^2 Attachment Side View Velocity Contour

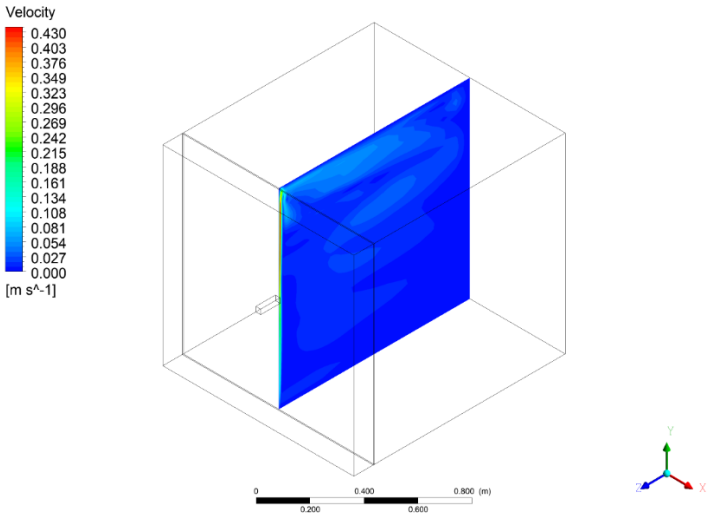

Figure V-48 6.25 cm^2 Attachment Isometric View Velocity Contour

Figure V-49, Figure V-50, and Figure V-51 show the thermal boundary layer formed at the steel bulkhead, and the resulting temperature distribution in the air region. From analyzing these figures, it can be observed that the air has the highest temperature at the wall, specifically where the attachment meets the steel, and at the top of the air region due to natural convection. Figure V-51 shows a zoomed view of where the attachment meets the steel. At this region, the temperature is highest, with a maximum of 426 K. The temperature build-up at this point is due to the steel having a higher thermal conductivity than the insulation.

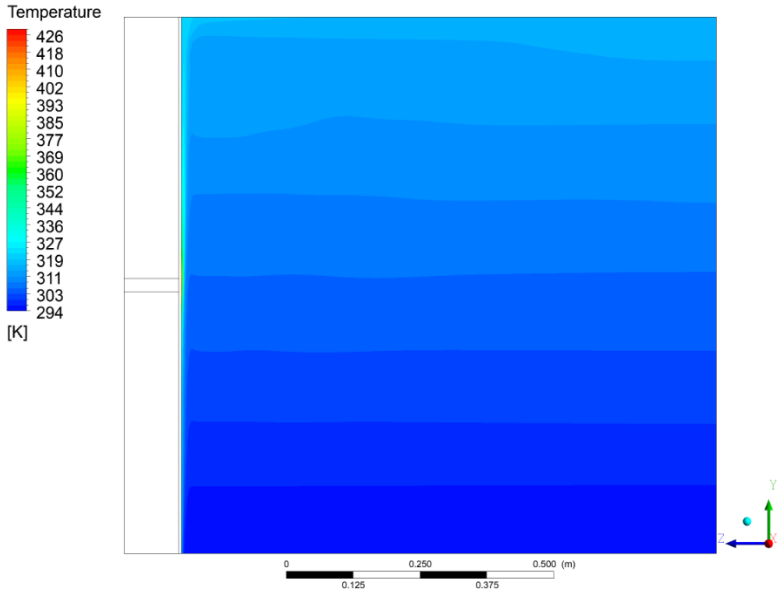

Figure V-49 6.25 cm^2 Attachment Side View Temperature Contour Air

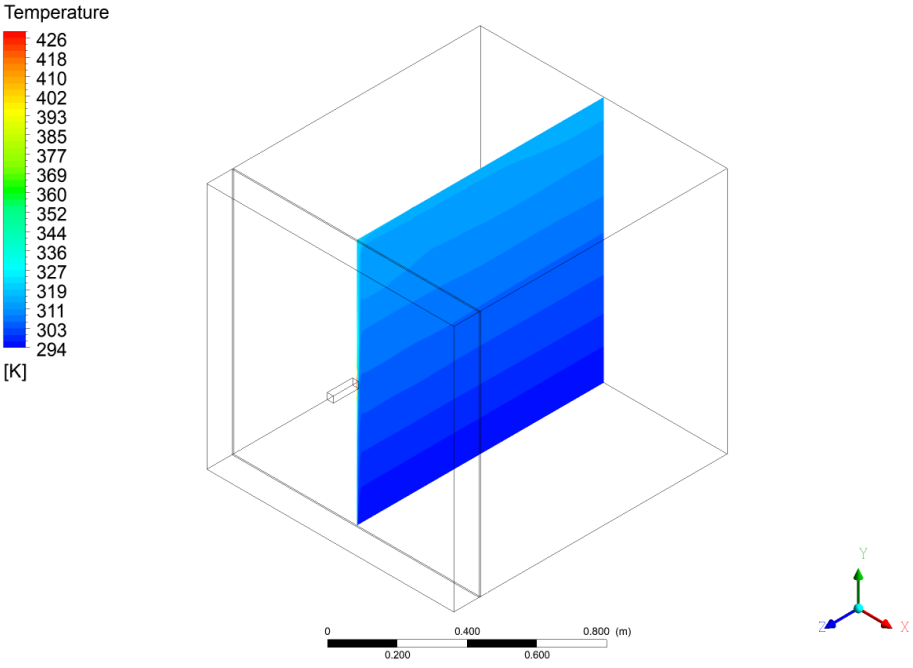

Figure V-50 6.25 cm^2 Attachment Isometric View Temperature Contour Air

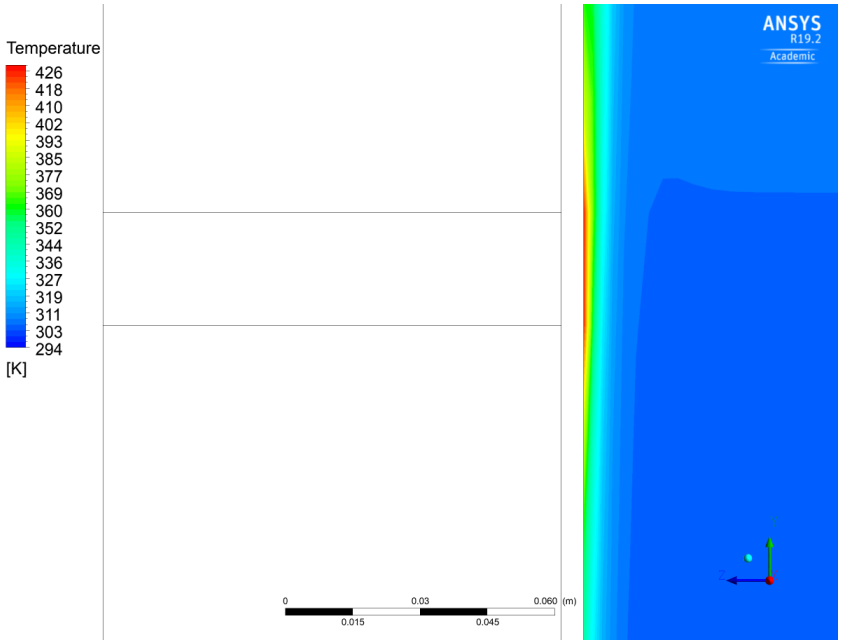

Figure V-51 6.25 cm^2 Attachment Zoomed View Temperature Contour Air

Figure V-52 and Figure V-53 represent the temperature at the steel bulkhead for the non-fire side of the model. It can be seen that the temperature is highest where the attachment meets the steel bulkhead. A point temperature was taken at this hot spot and the temperature was 429.57 K or 156.42^o C.

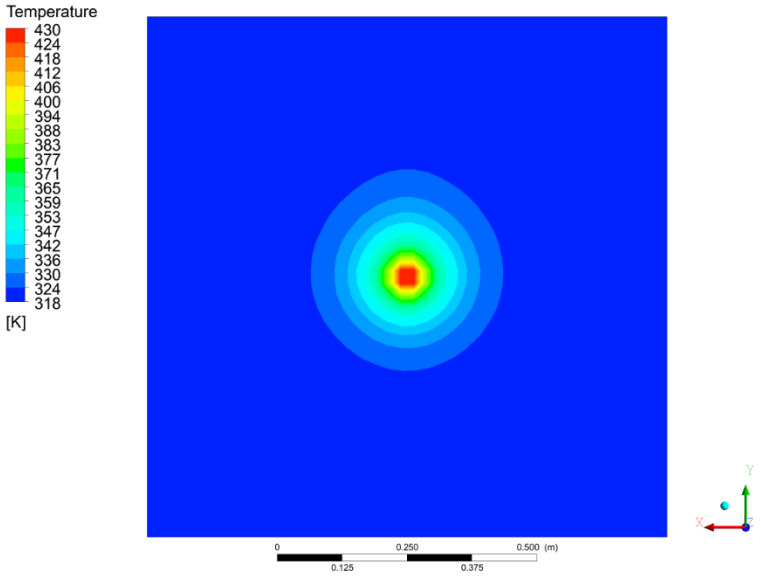

Figure V-52 6.25 cm^2 Attachment Steel Bulkhead Air-side View Temperature Contour

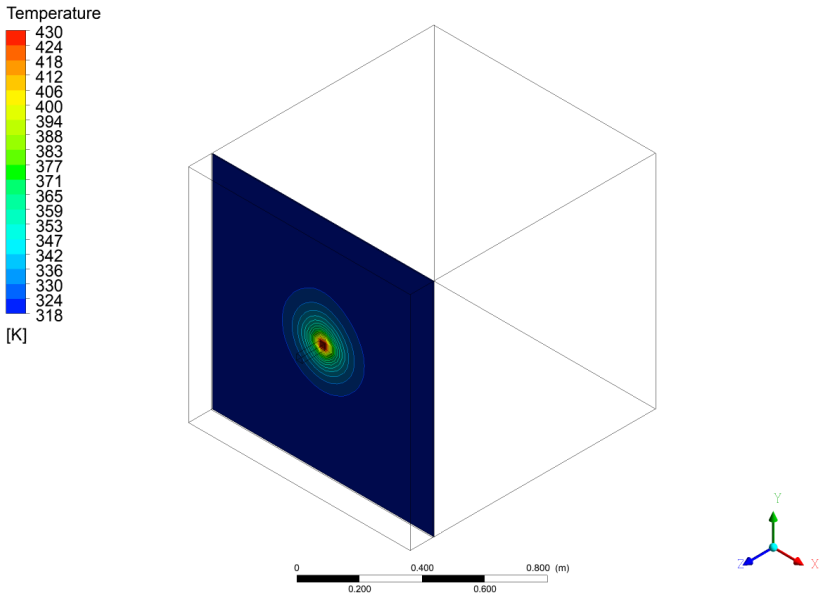

Figure V-53 6.25 cm^2 Attachment Steel Bulkhead Isometric View Temperature Contour

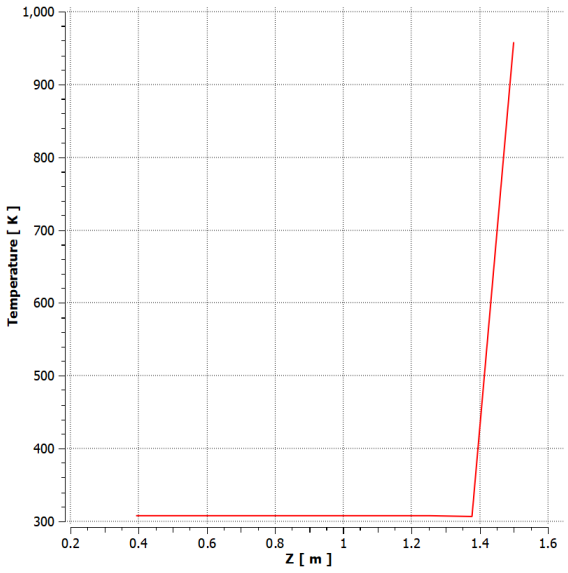

Figure V-54 6.25 cm^2 Attachment Temperature along Centerline

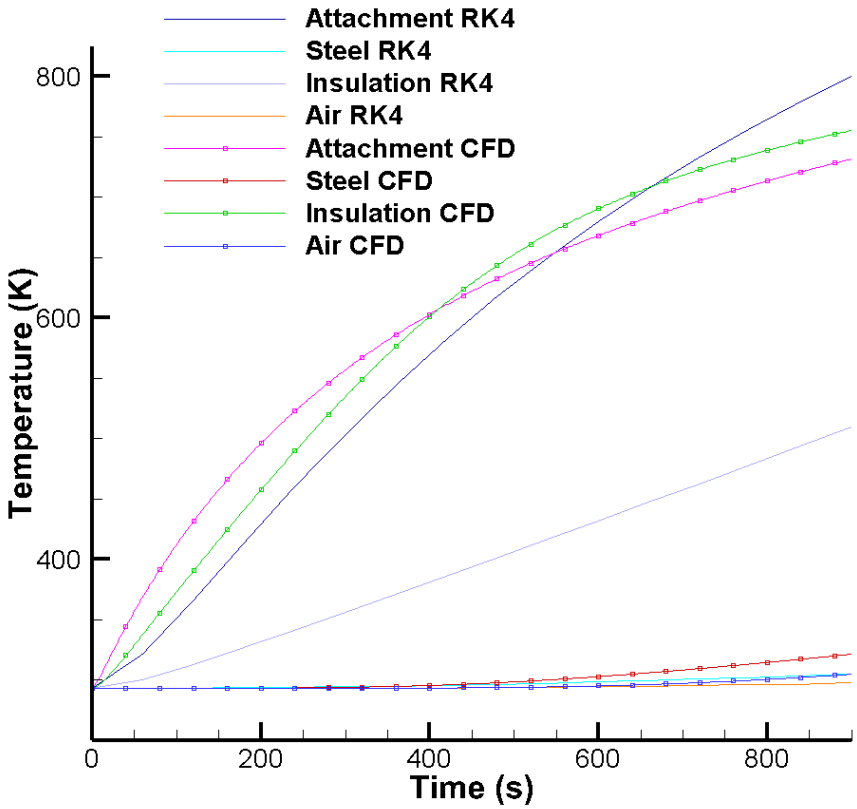

Figure V-55 6.25 cm^2 Attachment CFD Results vs Lumped Capacitance Parallel Flow

Figure V-54 shows how the temperature sharply decreases along the centerline of the model. Figure V-55 is a comparison of the CFD model to the lumped capacitance model. From analyzing this model, it can be determined that the air and steel temperature averages were more accurately predicted than the insulation.

When compared to the regulations, the attachment with a surface area of 6.25 cm^2 complies. "Such that the average temperature of the unexposed side will not rise more than 140° C above the original temperature, nor will the temperature, at any one point, including any joint, rise more than 180° C above the original temperature" (SOLAS Consolidated Edition, 2014, p. 125). The point with highest temperature on the non-fire side of the steel bulkhead was 429.57 K or 156.42° C. This temperature was an increase of 136.42° C, which is well below the requirement of 180° C. Also, the average temperature of

the air for the model was 304.81 K or 31.66^{o} C; this resulted in an 11.66^{o} C rise in temperature. This temperature rise complies with the stated regulation.

2. 25 cm^2 Attachment

Figure V-56 and Figure V-57 show that an attachment with a larger surface area and volume allows heat to travel through it more readily than the insulation and a smaller attachment. This will cause a higher temperature build-up where the attachment meets the steel bulkhead. These contours also show a more impactful temperature increase in the air region.

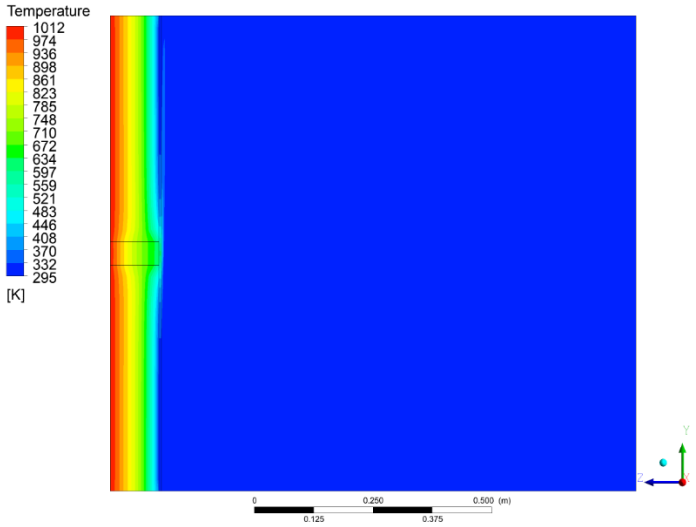

Figure V-56 25 cm^2 Attachment Side View Temperature Contour

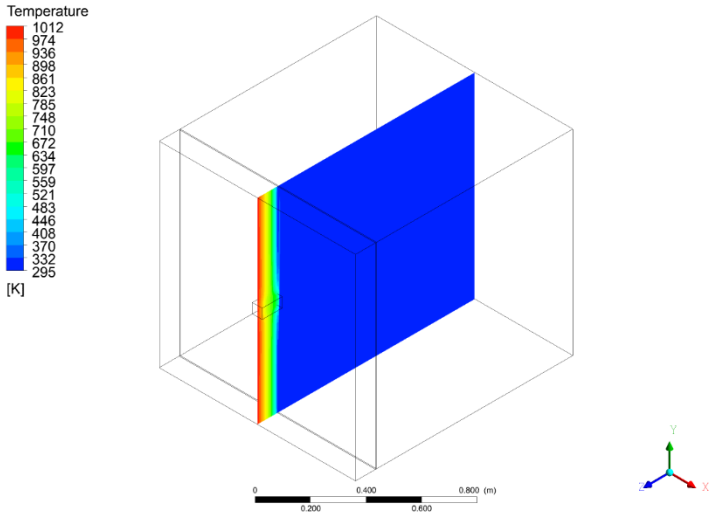

Figure V-57 25 cm^2 Attachment Isometric View Temperature Contour

Figure V-58 and Figure V-59 show the viscous boundary layer that developed at the steel bulkhead. From looking at the velocity contours, it can be seen that the flow's velocity is even more after the larger attachment. The maximum velocity for the model with the attachment is also much greater than the model with the 6.25 cm^2 attachment, see Figure V-47. This could be due to the higher temperature at the intersection of the attachment and the steel bulkhead and more area at a higher temperature.

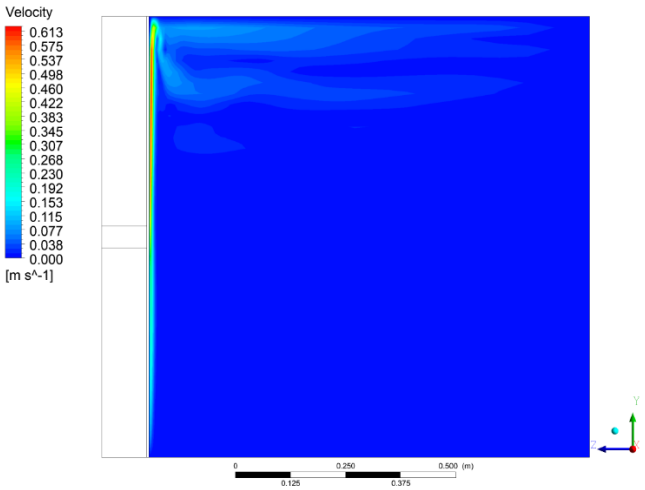

Figure V-58 25 cm^2 Attachment Side View Velocity Contour

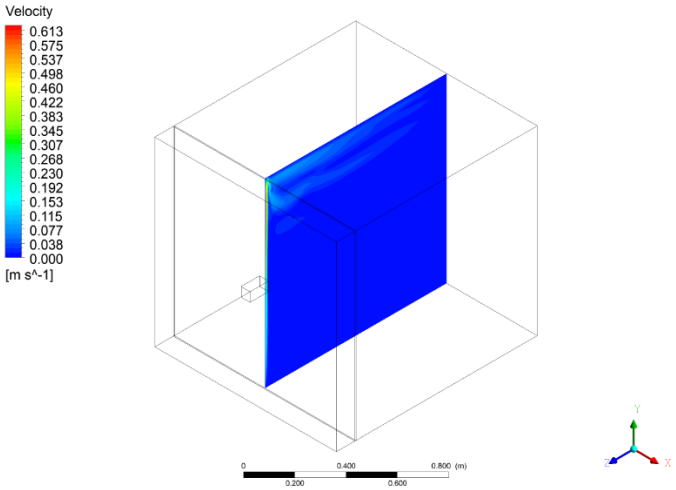

Figure V-59 25 cm^2 Attachment Isometric View Velocity Contour

Figure V-60, Figure V-61, and Figure V-62 show the thermal boundary layer formed at the steel bulkhead for the 25 cm^2 attachment and the resulting temperature distribution in the air region. From analyzing these figures, it can be observed that the air has the highest temperature at the wall, specifically where the attachment meets the steel, and at the top of the air region due to natural convection. Figure V-51 shows a zoomed view of where the attachment meets the steel. At this region, the temperature is highest, with a maximum of 600 K. This temperature is significantly greater than the 6.25 cm^2 attachment. The temperature build-up at this point is due to the steel having a higher thermal conductivity than the insulation and the greater surface area/volume of the attachment.

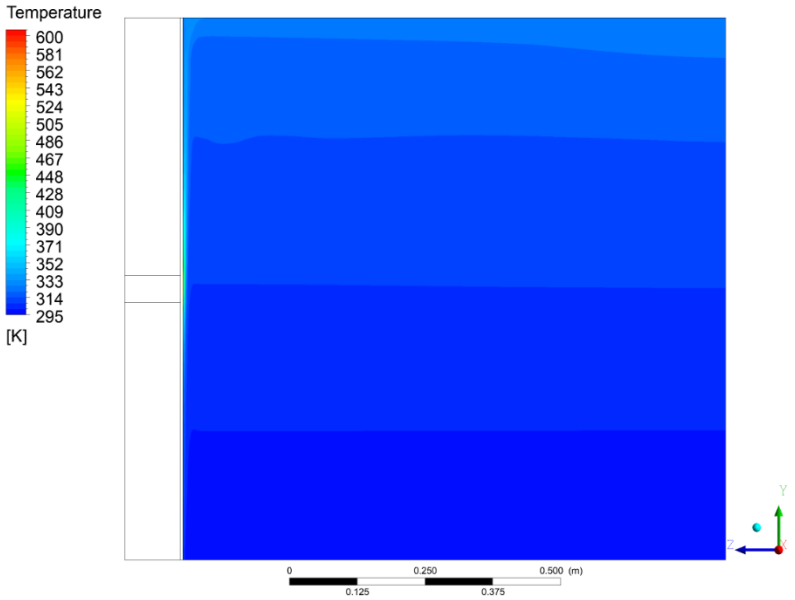

Figure V-60 25 cm^2 Attachment Side View Temperature Contour Air

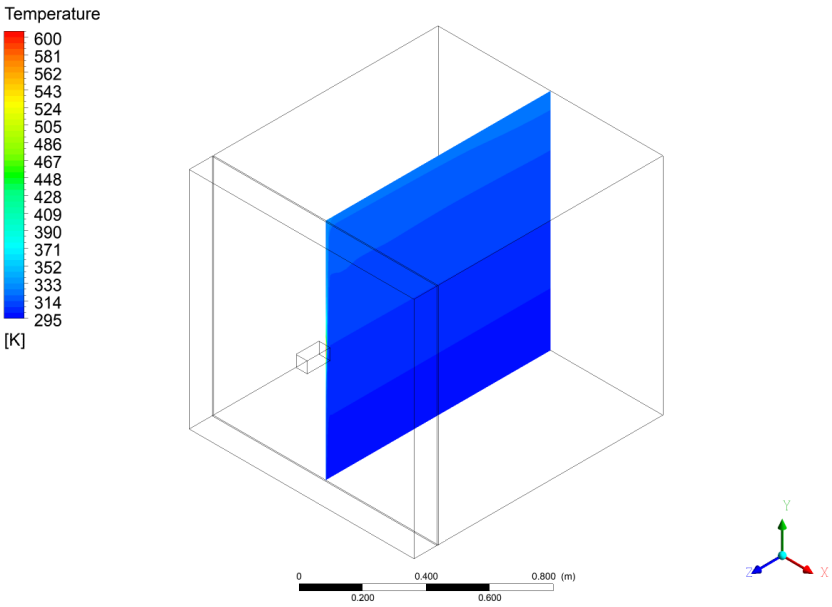

Figure V-61 25 cm^2 Attachment Isometric View Temperature Contour Air

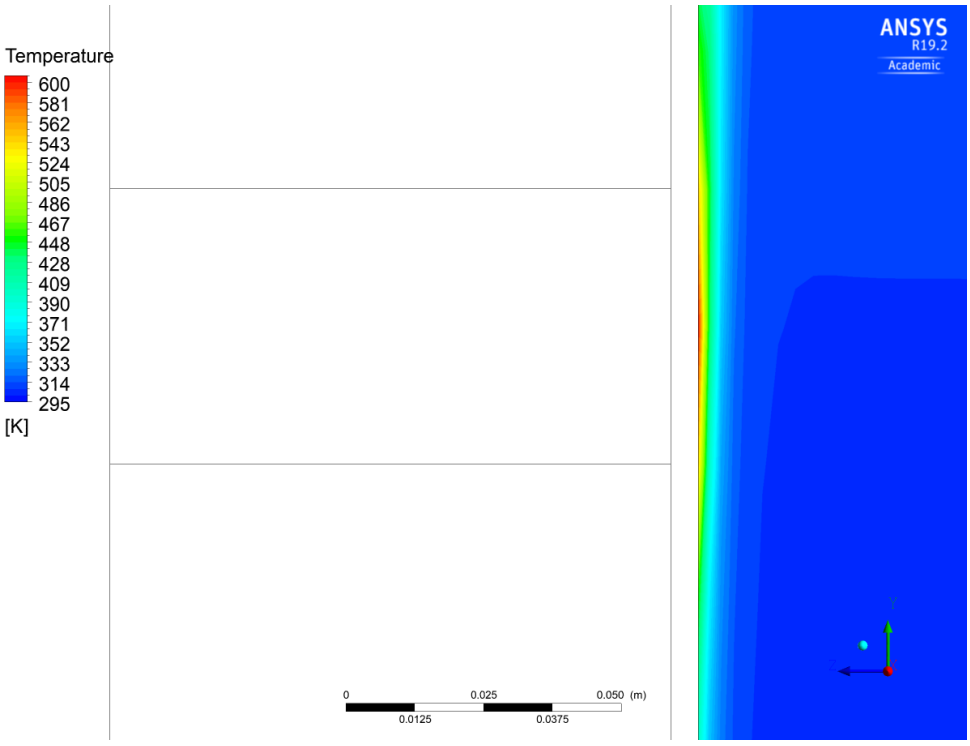

Figure V-62 25 cm^2 Attachment Zoomed View Temperature Contour Air

Figure V-63 and Figure V-64 represent the temperature at steel bulkhead for the non-fire side of the model. The temperature is highest where the attachment meets the steel bulkhead. A point temperature was taken at this hot spot being 606.85 K or 333.70º C.

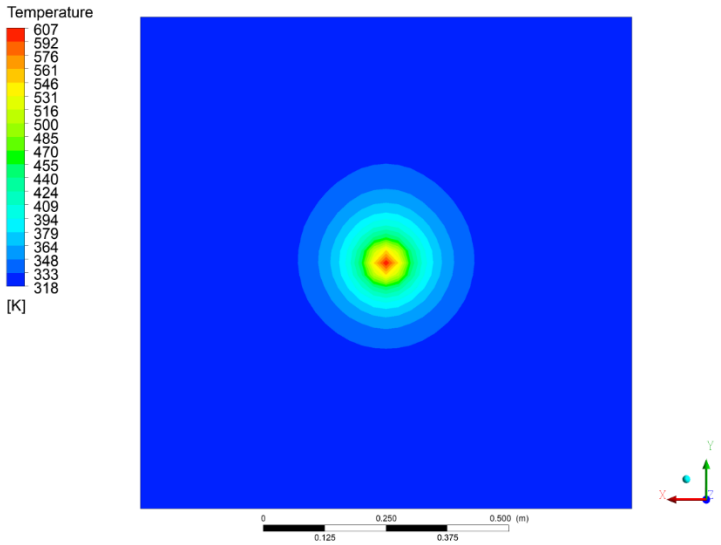

Figure V-63 25 cm^2 Attachment Steel Bulkhead Temperature Contour

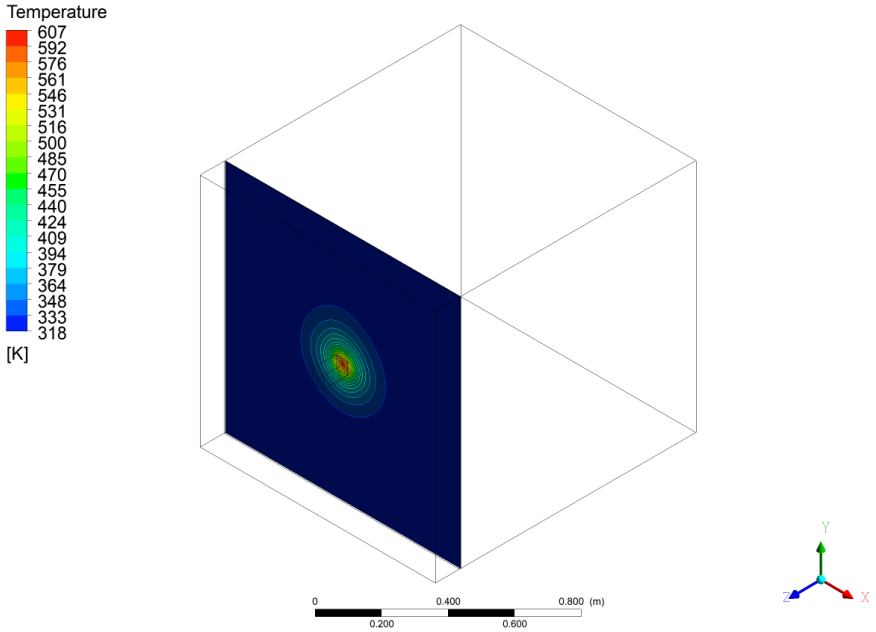

Figure V-64 25 cm^2 Attachment Steel Bulkhead Isometric View Temperature Contour

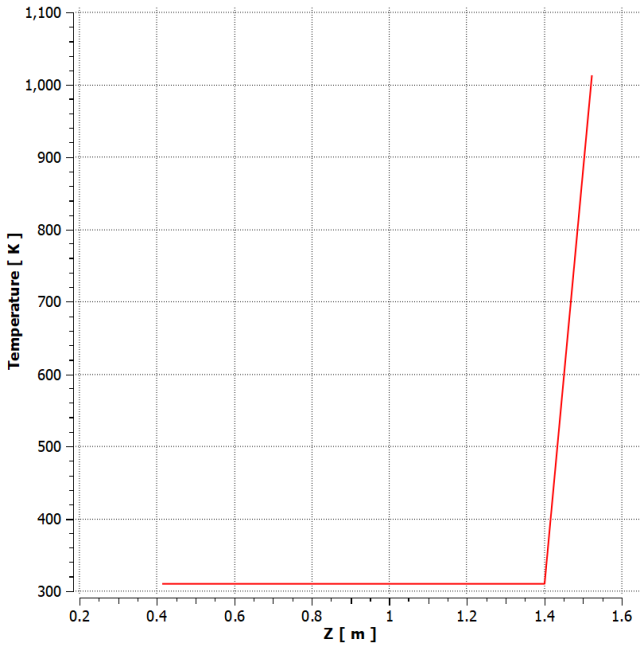

Figure V-65 5 cm^2 Attachment Temperature along Centerline

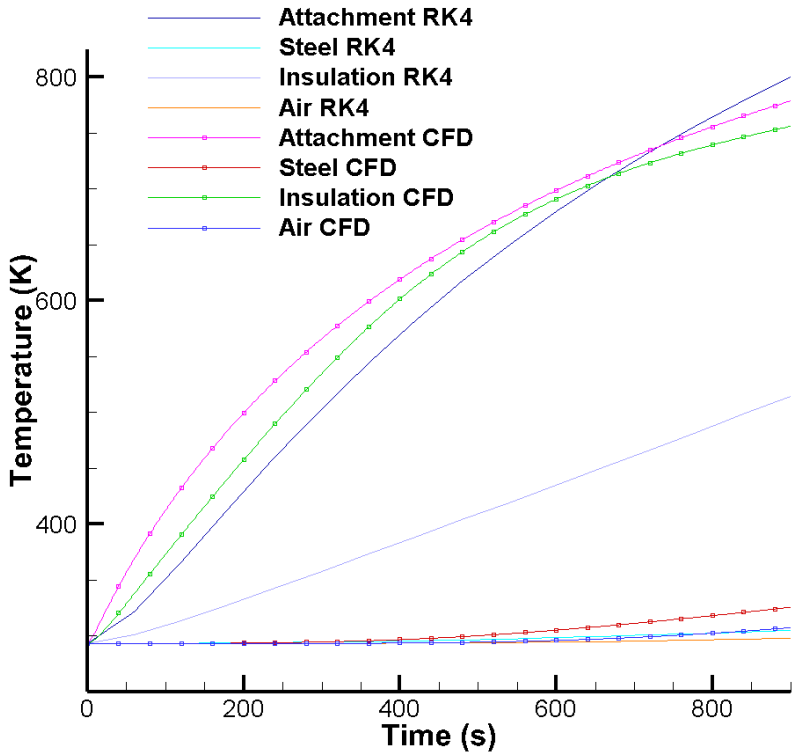

Figure V-66 25 cm^2 Attachment CFD Results vs Lumped Capacitance Parallel Flow

Figure V-65 shows how the temperature sharply decreases along the centerline of the model. Figure V-66 is a comparison of the CFD model to the lumped capacitance model. From analyzing this model, it can be determined that the air and steel temperature averages were more accurately predicted than the insulation.

When compared to the regulations, the attachment with a surface area of 25 cm^2 does not comply. It does not conform to the least stringent regulations of a "B" class division, in which the attachments must have "an insulation value such that the average temperature of the unexposed side will not rise more than 140^o C above the original temperature, nor will the temperature at any one point, including any joint, rise more than 225^o C above the original temperature" (SOLAS Consolidated Edition, 2014, p. 126). The point with the highest temperature on the non-fire side of the steel bulkhead was 606.85 K or 333.70^o C. This temperature was an increase of 313.70^o C, which is well above the requirement of 225^o C. Also, the average temperature of the air was 307.39 K or 34.24^o C; this resulted in a 14.24^o C rise in temperature. This temperature rise complies with the stated regulation, but the attachment fails overall because of the point temperature.

3. 100 cm^2 Attachment

An attachment of larger surface area and volume was tested because of the heat sink capabilities of steel (Zhang and Li, 2012). Figure V-67 and Figure V-68 show that an attachment with a larger surface area and volume allows heat to travel through it more readily than the insulation and a smaller attachment. This will cause a higher temperature build-up where the attachment meets the steel bulkhead. These contours also show a more impactful temperature increase in the air region.

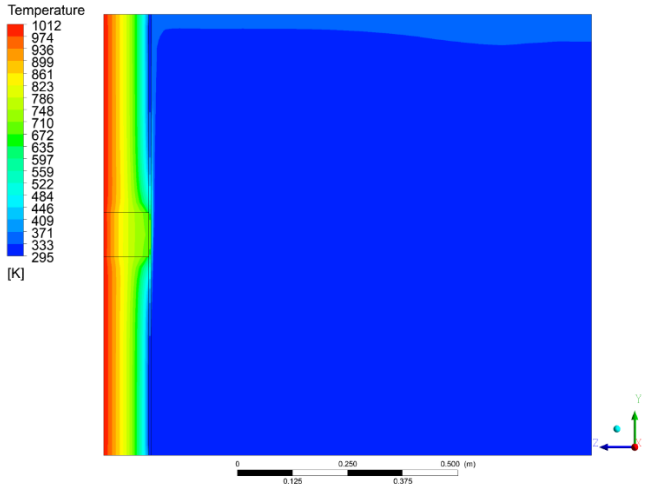

Figure V-67 100 cm^2 Attachment Side View Temperature Contour

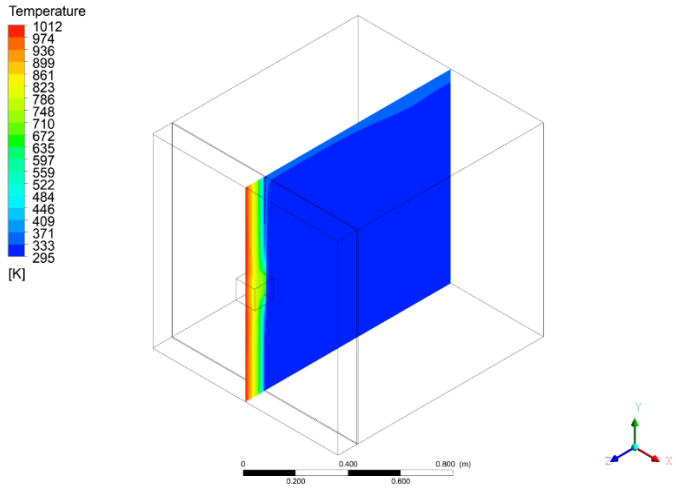

Figure V-68 100 cm^2 Attachment Isometric View Temperature Contour

Figure V-69 and Figure V-70 show the viscous boundary layer that developed at the steel bulkhead. From looking at velocity contours, it can be seen that the flow's velocity is greater for a larger attachment. The maximum velocity for the model with the attachment is also much greater than the model with the 6.25 cm^2 attachment and the model with the 25 cm^2, see Figure V-47 and Figure V-58. This could be due to the higher temperature at the intersection of the attachment and the steel bulkhead and more surface area at a higher temperature.

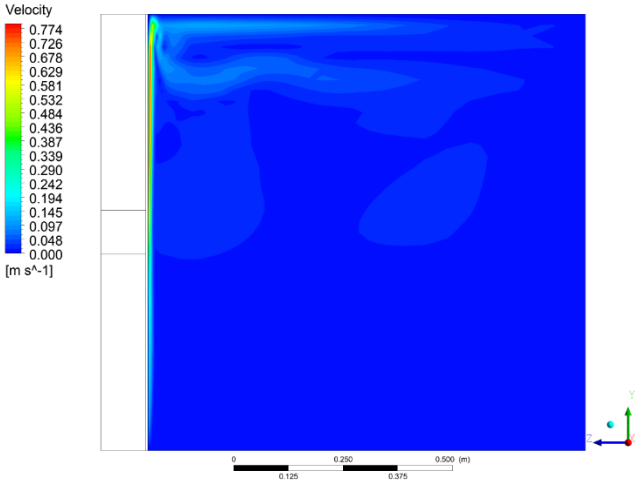

Figure V-69 100 cm^2 Attachment Side View Velocity Contour

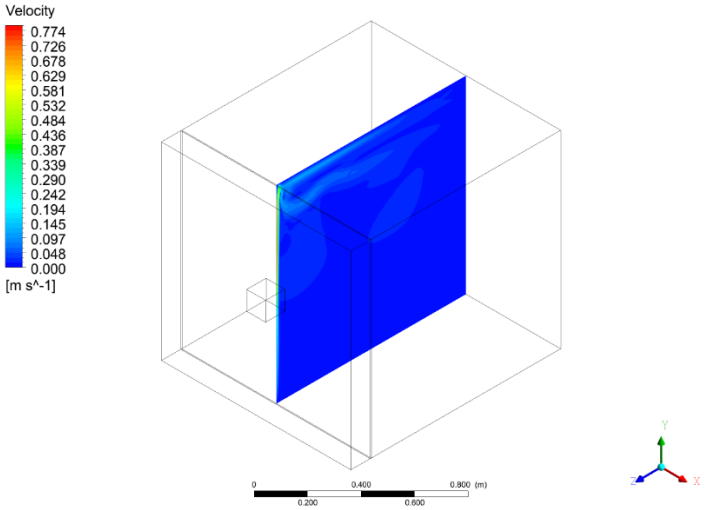

Figure V-70 100 cm^2 Attachment Isometric View Velocity Contour

Figure V-71, Figure V-72, and Figure V-73 show the thermal boundary layer formed at the steel bulkhead for the 100 cm^2 attachment and the resulting temperature distribution in the air region. From analyzing these figures, it can be observed that the air has the highest temperature at the wall, specifically where the attachment meets the steel, and at the top of the air region due to natural convection. Figure V-73 shows a zoomed view of where the attachment meets the steel. It can be seen that at this region the temperature is highest, with a maximum of 700 K. This temperature is significantly greater than the other attachments. The temperature build-up at this point is due to the steel having a higher thermal conductivity than the insulation and the greater surface area/volume of the attachment.

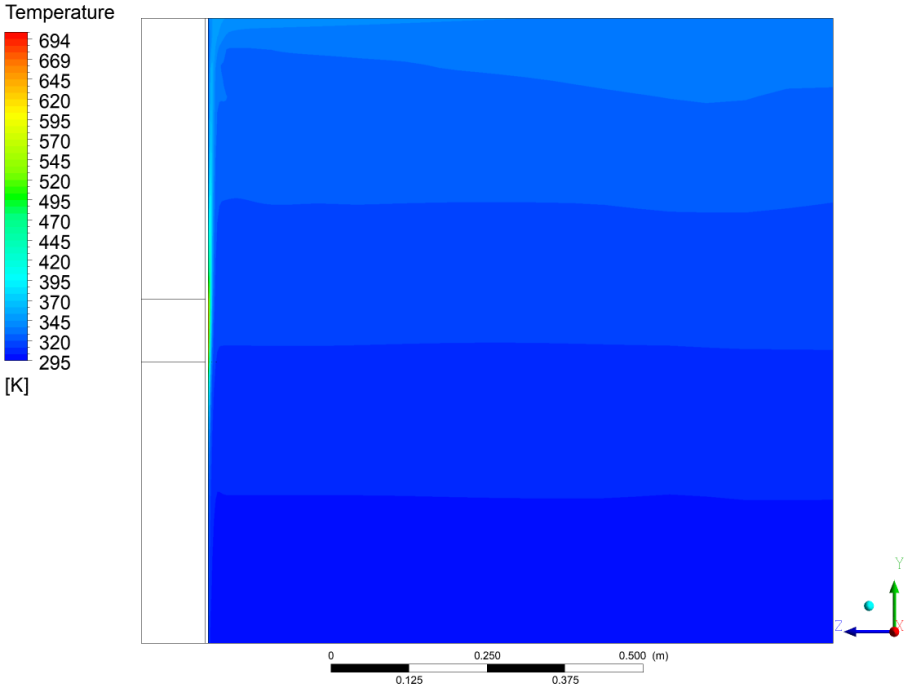

Figure V-71 100 cm^2 Attachment Side View Temperature Contour Air

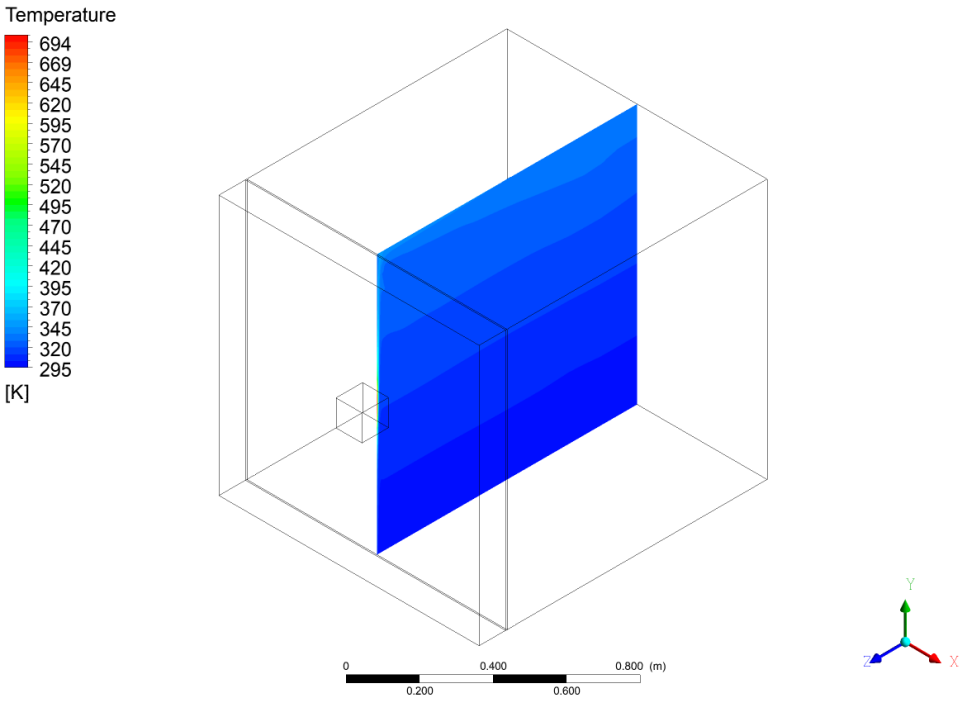

Figure V-72 100 cm^2 Attachment Isometric View Temperature Contour Air

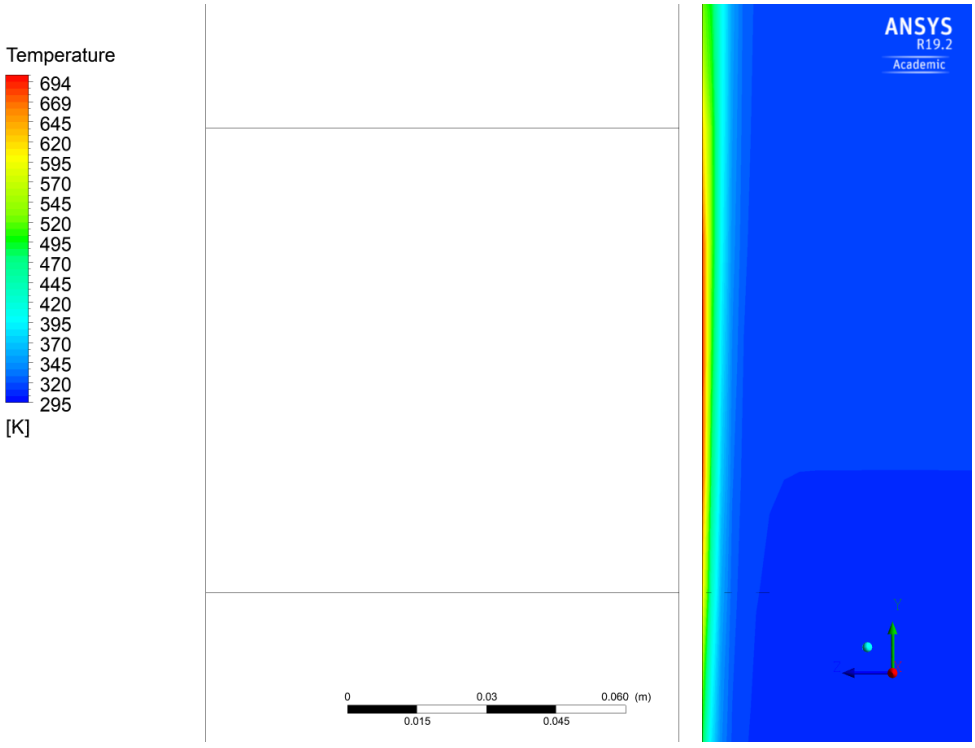

Figure V-73 100 cm^2 Attachment Zoomed View Temperature Contour Air

Figure V-74 and Figure V-75 represent the temperature at steel bulkhead for the non-fire side of the model. It can be seen that the temperature is highest were the attachment meets the steel bulkhead. A point temperature was taken at this hot spot being 702.73 K or 429.58^{o} C.

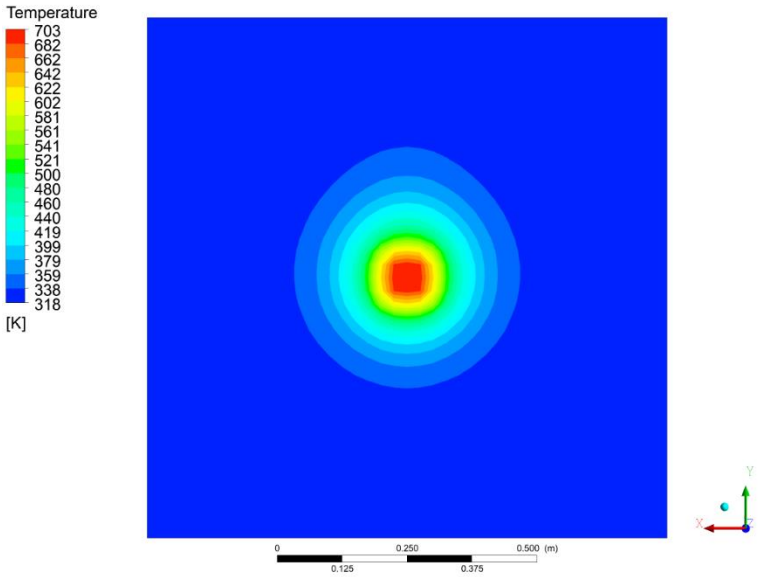

Figure V-74 100 cm^2 Attachment Steel Bulkhead Temperature Contour

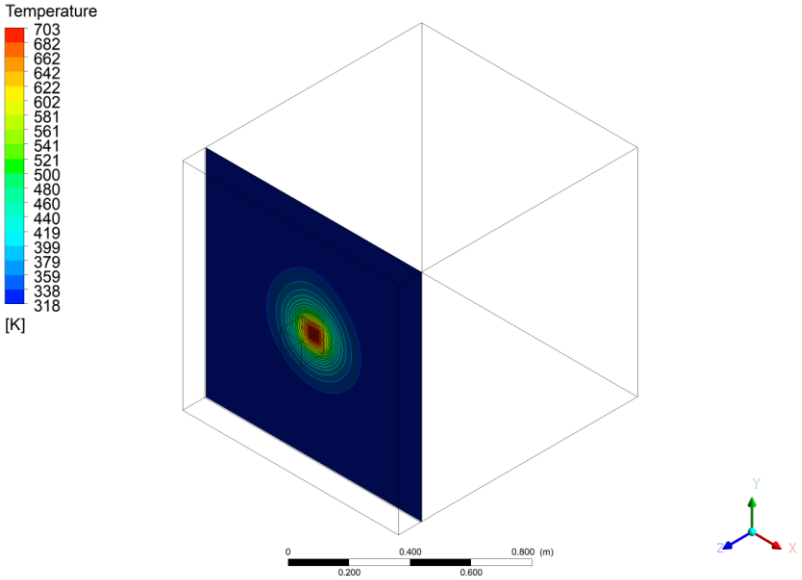

Figure V-75 100 cm^2 Attachment Steel Bulkhead Isometric View Temperature Contour

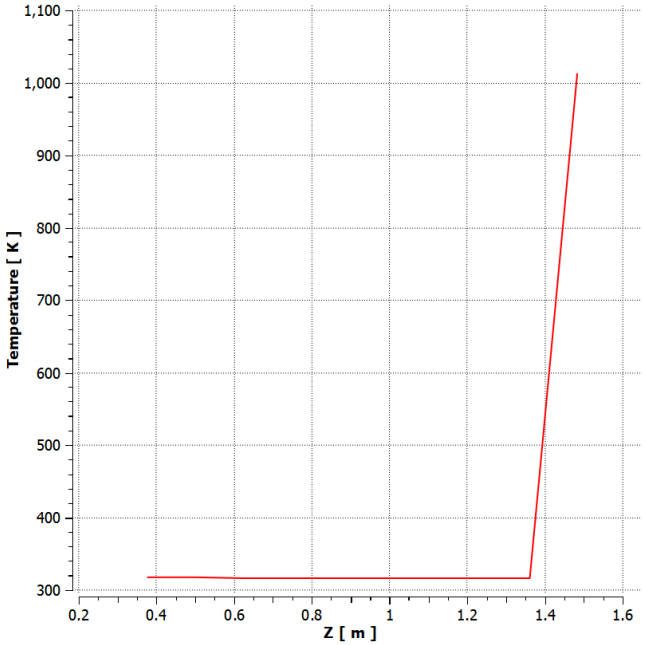

Figure V-76 100 cm^2 Attachment Temperature along Centerline

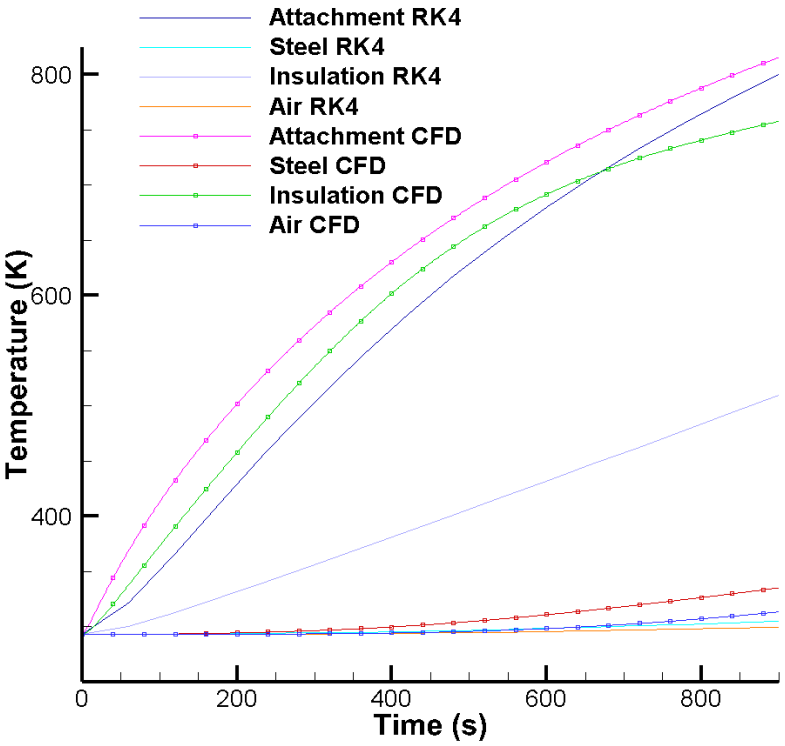

Figure V-77 100 cm^2 Attachment CFD Results vs Lumped Capacitance Parallel Flow

Figure V-76 shows how the temperature sharply decreases along the centerline of the model. Figure V-77 is a comparison of the CFD model to the lumped capacitance model. From analyzing this model, it can be determined that the air and steel temperature averages were more accurately predicted than the insulation.

When compared to the regulations, the attachment with a surface area of 100 cm^2 does not comply. It does not conform to the least stringent regulations of a "B" class division, in which the attachments must have "an insulation value such that the average temperature of the unexposed side will not rise more than 140^o C above the original temperature, nor will the temperature at any one point, including any joint, rise more than 225^o C above the original temperature" (SOLAS Consolidated Edition, 2014, p. 126). The point with highest temperature on the non-fire side of the steel bulkhead was 702.73 K or 429.58^o C. This temperature was an increase of 409.58^o C, which is well above the requirement of 225^o C. Also, the average temperature of the air was 313.44 K or 40.29^o C; this resulted in a 20.29^o C rise in temperature. This rise complies with the stated regulation, but the attachment fails overall because of the point temperature.

VI. Conclusion and Recommendations

The purpose of this thesis was to determine if attachments have a significant effect on the integrity of a fire division. It was determined at low surface areas and volumes that the attachment will still allow the division to conform to the regulations. However, at higher surface areas and volumes, the model failed the regulations. Therefore, it is possible for the attachments to pass, but only in certain circumstances. When a shipbuilder installs different attachments, they would need to model the division via CFD in order to determine the significance of those specific attachments' effect. Although, this method may be more costly to shipbuilders than applying coat-back or insulation to the attachments themselves.

Some limitations of this research were that the lumped capacitance model was unable to capture the high temperature gradient at the insulation. This is due to the model averaging the entire temperature of the region. In order to improve this, a 1-D Finite Volume method could be used to more properly capture the differing temperature gradients. Also, a more complicated geometry should be created and tested to see if the varying shapes, quantity, and locations of attachments have an overall effect on the fire division's integrity.

There are many opportunities for further research within this area of study. For example, a compressible model could be tested because a higher temperature at the interface of the steel bulkhead and air causes an increase of the boundary layer's velocity, leading to compressible flow. Therefore, a compressible model could be warranted in order to improve accuracy. In addition, a turbulent model could be tested because of the boundary layer's higher velocity. The specific heat for the insulation and steel could also be made temperature dependent and then analyzed. Finally, an idealized fire curve could be utilized instead of the standard time-temperature fire curve within the model to capture a more accurate prediction of the fire temperature.

Overall, the research concluded in this thesis demonstrates that small, uninsulated attachments may not affect the integrity of the fire division when in the A-15 rating.

References

Abdou, A. A., & Budaiwi, I. M. (2005). Comparison of Thermal Conductivity Measurements of Building Insulation Materials under Various Operating Temperatures. *Journal of Building Physics,29*(2), 171-184. doi:10.1177/1744259105056291

ANSYS FLUENT User's Guide (2009). release 12.0 edition. ANSYS Inc., Canonsburg, PA.

ANSYS FLUENT Theory Guide (2009). release 12.0 edition. ANSYS Inc., Canonsburg, PA.

Arpaci, V. S., & Larsen, P. S. (1984). *Convection heat transfer*. Englewood Cliffs, NJ: Prentice-Hall.

Basak, T., Roy, S., & Balakrishnan, A. (2006). Effects of thermal boundary conditions on natural convection flows within a square cavity. *International Journal of Heat and Mass Transfer,49*(23-24), 4525-4535. doi:10.1016/j.ijheatmasstransfer.2006.05.015

Beene, D. E., Jr., Howes, J. H., & Penn, A. (1988). *FIRE RESISTANCE TESTING OF BULKHEAD AND DECK PENETRATIONS*. Marine Fire and Safety Research Division.

Blagojevic, M., & Pesic, D. (2011). A new curve for temperature-time relationship in compartment fire. Thermal Science, 15(2), 339-352. doi:10.2298/tsci100927021b

Briggs, C. (2018, April 30). Attachments [E-mail to the author].

Cook, K. S. (2010). *CH-1 to NVIC 9-97, GUIDE TO STRUCTURAL FIRE PROTECTION*. United States Coast Guard.

DiNenno, P. J. (2008). *SFPE handbook of fire protection engineering*. Quincy, MA: National Fire Protection Ass.

ECFR.io. (n.d.). E-CFR Title 46 - Shipping. Retrieved from https://ecfr.io/Title-46/

Firefighting Procedures (Vol. 1). (2013). Fire Department City of New York.

Franssen, J., & Real, P. V. (2012). *Fire design of steel structures*. Berlin: Ernst.

Fusegi, T., Hyun, J. M., & Kuwahara, K. (1991). A numerical study of 3D natural convection in a cube: Effects of the horizontal thermal boundary conditions. *Fluid Dynamics Research,8*(5-6), 221-230. doi:10.1016/0169-5983(91)90044-j

Incropera, F. P. (2007). *Fundamentals of Heat and Mass Transfer*. Hoboken, NJ: John Wiley.

Introduction to CFD Methodology. (2010). Retrieved March 14, 2019, from https://imechanica.org/files/fluent_13.0_lecture02-intro-to-cfd.pdf

Jansson, R. (2004). *Measurement of Thermal Properties at Elevated Temperatures*. Swedish National Testing and Research Institute.

Makinde, O. D., & Olanrewaju, P. O. (2010). Buoyancy Effects on Thermal Boundary Layer Over a Vertical Plate With a Convective Surface Boundary Condition. *Journal of Fluids Engineering,132*(4), 044502. doi:10.1115/1.4001386

McQuiston, F. C., Parker, J. D., & Spitler, J. D. (2005). Heating, ventilating, and air conditioning: Analysis and design. Hoboken, NJ: John Wiley & Sons.

OFFICE OF THE FEDERAL REGISTER - U. S. (2018). *CODE OF FEDERAL REGULATIONS, TITLE 46 - SHIPPING: Revised as of October 1, 2017*. Place of publication not identified: BERNAN Press.

Patankar, S. V. (1980). *Numerical heat transfer and fluid flow*. U.S.: Hemisphere Pub.

SOLAS, consolidated edition 2014: Consolidated text of the International Convention for the Safety of Life at Sea, 1974, and its Protocol of 1988: Articles, annexes and certificates. (2014). London: International Maritime Organization.

Standard Test Methods for Fire Tests of Building Construction and Materials. (n.d.). *ASTM International, E 119*.

Wickström, U. (2008). Adiabatic Surface Temperature and the Plate Thermometer for Calculating Heat Transfer and Controlling Fire Resistance Furnaces. *Fire Safety Science,9*, 1227-1238. doi:10.3801/iafss.fss.9-1227

Wickström, U. (1985). Temperature analysis of heavily-insulated steel structures exposed to fire. *Fire Safety Journal,9*(3), 281-285. doi:10.1016/0379-7112(85)90038-4

Zhang, C., & Li, G. (2013). Modified One Zone Model For Fire Resistance Design Of Steel Structures. *Volume 9 Number 4,*282-297. doi:10.18057/ijasc.2013.9.4.2

Zitzmann, T., Cook, M., Pfrommer, P., Rees, S., & Marjanovic, L. (2005). Simulation of Steady-State Natural Convection Using CFD. *Ninth International IBPSA Conference,*1449-1456. Retrieved January 31, 2019.

Vita

Carl Hendrickson was born on December 10, 1991 in Nashville, Tennessee. He received his Bachelor's degree in Marine Engineering and Shipyard Management from the United States Merchant Marine Academy in 2014. Upon graduation, he commissioned into the United States Coast Guard. Carl conducts safety and security inspections on both domestic and international vessels for the Coast Guard. Carl is currently completing his Master's education in Mechanical Engineering at University of New Orleans and will be graduating in May 2019. He intends to continue serving in the United States Coast Guard after graduation.